Geosci. Model Dev. Discuss., 4, 3485–3598, 2011
www.geosci-model-dev-discuss.net/4/3485/2011/
doi:10.5194/gmdd-4-3485-2011

Geoscientific Model Development Discussions

Toward a minimal representation of aerosol direct and indirect effects: model description and evaluation

X. Liu[1], R. C. Easter[1], S. J. Ghan[1], R. Zaveri[1], P. Rasch[1], X. Shi[1], J.-F. Lamarque[2], A. Gettelman[2], H. Morrison[2], F. Vitt[2], A. Conley[2], S. Park[2], R. Neale[2], C. Hannay[2], A. M. L. Ekman[3], P. Hess[4], N. Mahowald[5], W. Collins[6], M. J. Iacono[7], C. S. Bretherton[8], M. G. Flanner[9], and D. Mitchell[10]

[1]Atmospheric Science and Global Change Division, Pacific Northwest National Laboratory, Richland, Washington, USA
[2]National Center for Atmospheric Research, Boulder, Colorado, USA
[3]Department of Meteorology and Bert Bolin Centre for Climate Research, Stockholm University, Sweden
[4]Biological and Environmental Engineering, Cornell University, Ithaca, New York, USA
[5]Earth and Atmospheric Sciences, Cornell University, Ithaca, New York, USA
[6]Earth Sciences Division, Lawrence Berkeley National Laboratory, Berkeley, California, USA
[7]Atmospheric and Environmental Research, Inc., Lexington, Massachusetts, USA
[8]Department of Atmospheric Sciences, University of Washington, Seattle, Washington, USA

[9]Department of Atmospheric, Oceanic & Space Sciences, University of Michigan, 2455 Hayward St., Ann Arbor, Michigan, USA
[10]Division of Atmospheric Sciences, Desert Research Institute, Reno, Nevada, USA

Received: 26 October 2011 – Accepted: 28 November 2011 – Published: 12 December 2011

Correspondence to: X. Liu (xiaohong.liu@pnnl.gov)

Published by Copernicus Publications on behalf of the European Geosciences Union.

GMDD
4, 3485–3598, 2011

Abstract

A modal aerosol module (MAM) has been developed for the Community Atmosphere Model version 5 (CAM5), the atmospheric component of the Community Earth System Model version 1 (CESM1). MAM is capable of simulating the aerosol size distribution and both internal and external mixing between aerosol components, treating numerous complicated aerosol processes and aerosol physical, chemical and optical properties in a physically based manner. Two MAM versions were developed: a more complete version with seven lognormal modes (MAM7), and a version with three lognormal modes (MAM3) for the purpose of long-term (decades to centuries) simulations. Major approximations in MAM3 include assuming immediate mixing of primary organic matter (POM) and black carbon (BC) with other aerosol components, merging of the MAM7 fine dust and fine sea salt modes into the accumulation mode, merging of the MAM7 coarse dust and coarse sea salt modes into the single coarse mode, and neglecting the explicit treatment of ammonia and ammonium cycles.

Simulated sulfate and secondary organic aerosol (SOA) mass concentrations are remarkably similar between MAM3 and MAM7 as most (~ 90 %) of these aerosol species are in the accumulation mode. Differences of POM and BC concentrations between MAM3 and MAM7 are also small (mostly within 10 %) because of the assumed hygroscopic nature of POM, so that much of the freshly emitted POM and BC is wet-removed before mixing internally with soluble aerosol species. Sensitivity tests with the POM assumed to be hydrophobic and with slower aging increase the POM and BC concentrations, especially at high latitudes (by several times). The mineral dust global burden differs by 10 % and sea salt burden by 30–40 % between MAM3 and MAM7 mainly due to the different size ranges for dust and sea salt modes and different standard deviations of the log-normal size distribution for sea salt modes between MAM3 and MAM7. The model is able to qualitatively capture the observed geographical and temporal variations of aerosol mass and number concentrations, size distributions, and aerosol optical properties. However, there are noticeable biases, e.g., simulated sulfate and

GMDD

4, 3485–3598, 2011

mineral dust concentrations at surface over the oceans are too low. Simulated BC concentrations are significantly lower than measurements in the Arctic. There is a low bias in modeled aerosol optical depth on the global scale, especially in the developing countries. There biases in aerosol simulations clearly indicate the need for improvements of aerosol processes (e.g., emission fluxes of anthropogenic aerosols and precursor gases in developing countries, boundary layer nucleation) and properties (e.g., primary aerosol emission size, POM hygroscopicity). In addition the critical role of cloud properties (e.g., liquid water content, cloud fraction) responsible for the wet scavenging of aerosol is highlighted.

1 Introduction

Atmospheric aerosol is recognized as one of the most important forcing agents in the climate system (Forster et al., 2007). Aerosol influences the Earth's radiative balance by directly scattering and absorbing solar and terrestrial radiation (direct effect). Aerosol affects the climate system indirectly by acting as cloud condensational nuclei (CCN) and ice nuclei (IN) and changing cloud microphysical and radiative properties (indirect effect). Aerosol can reduce cloud cover by heating the atmosphere in which clouds reside (semi-direct effect), and reduce the snow and land and sea ice albedo by deposition and melting of snow and ice (cryosphere radiative effect) (Flanner et al., 2007). However, after decades of intensive studies, aerosol forcings are still one of the largest uncertainties in projecting future climate change (Forster et al., 2007; Stevens and Feingold, 2009).

Recognizing the importance of aerosol in the climate system, almost all global climate models (GCMs) have implemented treatments of aerosol and its influence on climate. Unlike most greenhouse gases, which due to their long lifetimes (~ 5–10^2 yr) have a relatively uniform spatial distribution, aerosol particles have short lifetimes ($\sim$ days) and hence large spatial variations. In addition, aerosol particles span a spectrum of size ranges (10^{-3} to 10^{1} μm), multiple chemical species (e.g., sulfate, black

GMDD
4, 3485–3598, 2011

carbon (BC), organic carbon (OC), mineral dust and sea salt), and change through complicated physical and chemical aging in the atmosphere. This diversity and complexity imposes a great challenge to representing aerosol processes and properties in GCMs.

There are several methods of aerosol treatments in GCMs. The bulk method only predicts mass mixing ratio of various aerosol species and prescribes fixed aerosol size distributions in order to convert aerosol mass to number mixing ratio. External mixing is often assumed between different aerosol species (each particle is composed of only one chemical species), and a time scale of 1–2 days is prescribed for the aging of carbonaceous aerosols from hydrophobic to hydrophilic state. The bulk method neglects the fact that aerosol size distributions are significantly different between continents and oceans and at the surface and in the upper troposphere, and therefore the bulk method may introduce biases in estimates of the aerosol direct and indirect forcing. This method also neglects the fact that different aerosol species are often internally mixed (Clarke et al., 2004; Moffet and Prather, 2009), which for BC and sulfate can enhance absorption of sunlight by up to a factor of two (Jacobson, 2003). Neglecting this internal mixture can significantly affect estimates of aerosol direct forcing (Jacobson, 2001).

The most sophisticated and accurate method for aerosol treatment in GCMs is the sectional method (Jacobson, 2001; Adams and Seinfeld, 2002; Spracklen et al., 2005) when using a sufficient number of size bins. However, it is still prohibitive for GCMs to implement this method for long simulations (decades to centuries) due to limited computational resources. An intermediate treatment is the modal method (Wilson et al., 2001; Herzog et al., 2004; Vignati et al., 2004; Easter et al., 2004), in which aerosol size distributions are represented by multiple log-normal functions. By predicting mass mixing ratios of different aerosol species and number mixing ratio within each mode and prescribing standard deviations of log-normal size distributions based on observations, aerosol size distributions can be derived. The modal method generally assumes that different aerosol species are internally mixed within modes and externally

GMDD
4, 3485–3598, 2011

mixed between modes, and thus represents aerosol mixing states more realistically than the bulk method. The modal method has been implemented in the ECHAM5 (Stier et al., 2005), Community Atmosphere Model version 2 (CAM2) (Ghan and Easter, 2006) and version 3 (CAM3) (Wang et al., 2009). The quadrature method of moments (QMOM) (McGraw, 1997; Wright et al., 2001; Yoon and McGraw, 2004) has some similarities to the modal method, but is more powerful in that it does not require assumptions about the shape of the aerosol size distribution (e.g., log-normal). Another important consideration is the number of aerosol types that are used to represent the aerosol mixing state. Typically just a few types are used (e.g., fresh/hydrophobic and aged/mixed/hygroscopic in the sub-micron range, and dust and sea salt in the super-micron), but a few studies have used many more (Jacobson, 2001; Bauer et al., 2008).

Numerous processes in the atmosphere affect aerosol physical, chemical and optical properties (e.g., number/mass concentration, size, density, shape, refractive index, chemical composition): aerosol nucleation, coagulation, condensational growth, gas- and aqueous-phase chemistry, emission, dry deposition and gravitational settling, water uptake, in-cloud and below-cloud scavenging, and release from evaporated cloud and rain droplets. Uncertainties in the treatment of these processes in GCMs will influence our confidence in estimates of aerosol radiative forcing and climate impacts. For example, wet removal of aerosol was identified as one of the major processes responsible for the large differences (by more than a factor of 10) in aerosol concentrations in the free troposphere and in the polar regions among models participating in the Aerosol Model Intercomparison Initiative (AeroCom) project (Kinne et al., 2006; Koch et al., 2009). There are still large uncertainties in secondary organic aerosol (SOA) formation and aging and its physical and chemical properties (Kanakidou et al., 2005; Farina et al., 2010; Jimenez et al., 2009). Large uncertainties exist for aerosol emissions, including emission sizes, injection heights of biomass burning aerosol, and flux rates of sea salt and mineral dust. The uncertainty in aerosol mixing states will impact its hygroscopicity, water uptake, droplet activation, and optical properties important for aerosol direct and indirect radiative forcing.

GMDD
4, 3485–3598, 2011

The modal method is a favorable approach for conserving computational resources and for representing aerosol size distributions and mixing states with sufficient accuracy to estimate aerosol radiative forcing. However, even for models adopting this method, there can be large differences between models in selecting the number of modes and the number of aerosol species in each mode. The treatment of aerosol aging, water uptake and optics of aerosol internal/external mixtures can be different. There can be different complexities for the treatment of SOA formation and gas/particle partitioning including the comprehensive one based on the volatility basis set (VBS) (Farina et al., 2010). However, for GCMs with many detailed and time-consuming components (atmosphere, land, ocean, sea ice, biosphere with carbon/nitrogen cycles) running for decades to centuries, a minimal representation of aerosol that can capture the essentials of aerosol forcing on climate is highly desirable.

The minimum level of complexity needed to represent both anthropogenic and natural aerosol effects on climate cannot be determined and described in a single manuscript. Drawing on previous work, in this study we have implemented a plausible set of aerosol lifecycle processes in a global atmosphere model, and focus on the sensitivity of the aerosol lifecycle to simplifications in the representation of the aerosol in the model. The impact of simplifications in the representation of aerosol on aerosol forcing and the decomposition of the total anthropogenic aerosol forcing by mechanism and species are presented in a companion paper (Ghan et al., 2011). Section 2 describes the model used, including one relatively complete and one simplified representation of the aerosol. Section 3 compares global distributions and budgets of aerosol simulated with both representations. Section 4 evaluates simulations with both representations of the aerosol. Section 5 considers additional sensitivity experiments to improve understanding of the differences found for the two representations. Conclusions and future work are summarized in Sect. 6.

GMDD
4, 3485–3598, 2011

2 Model description

The model used in this study is version 5.1 of the Community Atmosphere Model (CAM5.1), which is a major update of CAM3.5 described by Gent et al. (2009). With the exception of deep cumulus convection, almost all processes in CAM5.1 differ markedly from CAM3.5. Here we summarize the treatment of aerosols, clouds, radiation, and turbulence in this model.

2.1 Aerosol

We have implemented two different modal representations of the aerosol. A 7-mode version of the modal aerosol model (MAM7) serves as a benchmark for further simplification. It includes Aitken, accumulation, primary carbon, fine dust and sea salt and coarse dust and sea salt modes (Fig. 1). Within a single mode, for example, the accumulation mode, we predict the mass mixing ratios of internally-mixed sulfate (SO_4), ammonium (NH_4), SOA, organic matter (OM) aged from the primary carbon mode, black carbon (BC) aged from the primary carbon mode, sea salt, and the number mixing ratio of accumulation mode particles. Primary carbon (OM and BC) particles are emitted to the primary carbon mode and aged to the accumulation mode due to condensation of H_2SO_4, NH_3 and semi-volatile organics and coagulation with Aitken and accumulation modes (see section below).

Aerosol particles (AP) exist in different attachment states. We mostly think of AP that are suspended in air (either clear or cloudy air), and these are referred to as interstitial AP. AP can also be attached to (or contained within) different hydrometeors, such as cloud droplets. In CAM5, the interstitial AP and the AP in stratiform cloud droplets (referred to as cloud-borne AP) are both explicitly predicted, as in Easter et al. (2004). The interstitial AP species are transported in 3 dimensions. The cloud-borne AP species are not transported (except for vertical turbulent mixing) but saved every time step, which saves computer time but has little impact on their predicted values (Ghan and Easter, 2006).

GMDD
4, 3485–3598, 2011

The size distributions of each mode are assumed to be log-normal, with the mode dry or wet radius varying as number and total dry or wet volume change, and standard deviation is prescribed as given in Fig. 1. The total number of transported aerosol tracers is 31 for MAM7. The transported gas species are sulfur dioxide (SO_2), hydrogen peroxide (H_2O_2), dimethylsulfide (DMS), sulfuric acid gas (H_2SO_4), ammonia (NH_3), and a lumped semi-volatile organics species.

For long-term (decades to centuries) climate simulations a 3-mode version of MAM (MAM3) is also developed that has only Aitken, accumulation and coarse modes (Fig. 2). For MAM3 the following assumptions are made: (1) primary carbon is internally mixed with secondary aerosol by merging the primary carbon mode with the accumulation mode; (2) the coarse dust and sea salt modes are merged into a single coarse mode based on the recognition that sources of dust and sea salt are geographically separated. Although dust is much less soluble than sea salt, it readily absorbs water (Koretsky et al., 1997) and activates similarly as CCN (Kumar et al., 2009), particularly when coated by solutes like sulfate and organic, and so it is likely to be removed by wet deposition almost as easily as sea salts, so this is unlikely to introduce substantial error into our simulations; (3) the fine dust and sea salt modes are similarly merged with the accumulation mode; (4) sulfate is partially neutralized by ammonium in the form of NH_4HSO_4, so ammonium is effectively prescribed and NH_3 is not simulated. The total number of transported aerosol tracers in MAM3 is 15. The transported gas species are SO_2, H_2O_2, DMS, H_2SO_4, and a lumped semi-volatile organics species. The prescribed standard deviations are given in Fig. 2.

2.1.1 Emissions

Anthropogenic (defined here as originating from industrial, energy, transportation, domestic and agriculture activity sectors) emissions are from the Lamarque et al. (2010) IPCC AR5 emission dataset. Emissions of BC and OC represent an update of Bond et al. (2007) and Junker and Liousse (2008). Emissions of SO_2 are an update of Smith et al. (2001, 2004).

GMDD
4, 3485–3598, 2011

The IPCC AR5 emission data set includes emissions for anthropogenic aerosols and precursor gases: SO_2, primary OM (POM), and BC. However, it does not provide injection heights and size distributions of primary emitted particles and precursor gases for which we have followed the AeroCom protocols (Dentener et al., 2006). We assumed that 2.5 % (molar) of sulfur emissions are emitted directly as primary sulfate aerosols and the rest as SO_2 (Dentener et al., 2006). Sulfur from agriculture, domestic, transportation, waste, and shipping sectors is emitted at the surface while sulfur from energy and industry sectors is emitted at 100–300 m above the surface, and sulfur from forest fire and grass fire is emitted at higher elevations (0–6 km). Sulfate particles from agriculture, waste, and shipping (surface sources), and from energy, industry, forest fire and grass fire (elevated sources) are put in the accumulation mode, and those from domestic and transportation are put in the Aitken mode. POM and BC from forest fire and grass fire are emitted at 0–6 km, while those from other sources (domestic, energy, industry, transportation, waste, and shipping) are emitted at the surface. Injection height profiles for fire emissions are derived from the corresponding AeroCom profiles (Dentener et al., 2006), which vary spatially and temporally. Mass emission fluxes for sulfate, POM and BC are converted to number emission fluxes for Aitken and accumulation mode at the surface or at higher elevations based on AeroCom prescribed lognormal size distributions as summarized in Table 1.

The IPCC AR5 data set also does not provide emissions of natural aerosols and precursor gases: volcanic sulfur, DMS, NH_3, and biogenic volatile organic compounds (VOCs). Thus AeroCom emission fluxes, injection heights and size distributions for volcanic SO_2 and sulfate and the surface DMS flux are used. The emission flux for NH_3 is prescribed from the MOZART-4 data set (Emmons et al., 2010). Emission fluxes for isoprene, monoterprenes, toluene, big alkenes, and big alkanes, which are used to derive emissions of the semi-volatile organic species, are prescribed from the MOZART-2 data set (Horowitz et al., 2003). These emissions represent late 1990's conditions. For years prior to 2000, we use anthropogenic non-methane VOC (NMVOC) emissions from IPCC AR5 and scale the MOZART toluene, big alkene, and big alkane emissions

GMDD
4, 3485–3598, 2011

by the ratio of year-of-interest NMVOC emissions to year 2000 NMVOC emissions.

The emission of sea salt aerosols from the ocean follows the parameterization by Märtensson et al. (2003) for aerosols with geometric diameter $< 2.8\,\mu m$. The total number particle flux F_0 ($m^{-2}\,s^{-1}$) is described by

$$\frac{dF_0}{d\log D_p} = \Phi W = (A_k T_w + B_k)\cdot W, \quad (1)$$

where D_p is the particle diameter, T_w is the water temperature and A_k and B_k are coefficients dependent on the size interval. W is the white cap area:

$$W = 3.84\times 10^{-4}\cdot U_{10}^{3.41}, \quad (2)$$

where U_{10} is the wind speed at 10 m. For aerosols with a geometric diameter $\geq 2.8\,\mu m$, sea salt emissions follow the parameterization by Monahan et al. (1986):

$$\frac{dF_0}{d\log r} = 1.373\cdot U_{10}^{3.41} r^{-3}(1+0.0057 r^{1.05})\times 10^{1.19 e^{-B^2}}, \quad (3)$$

where r is the radius of the aerosol at a relative humidity of 80 % and $B = (0.380 - \log r)/0.650$. All sea salt emission fluxes in the model are calculated for a size interval of $d\log D_p = 0.1$ and then summed up for each modal size range. The cut-off size ranges for sea salt emissions in MAM7 are 0.02–0.08 (Aitken), 0.08–0.3 (accumulation), 0.3–1.0 (fine sea salt), and 1.0–10 µm (coarse sea salt); for MAM3 the ranges are 0.02–0.08 (Aitken), 0.08–1.0 (accumulation), and 1.0–10 µm (coarse).

In regions of strong winds, dry, un-vegetated soils generate soil particles small enough to be entrained into the atmosphere, and these are referred to here as mineral dust particles. The generation of mineral dust particles is calculated based on the Dust Entrainment and Deposition Model (Zender et al., 2003), and the implementation in the Community Climate System Model has been described and compared to observations (Mahowald et al., 2006a, 2006b; Yoshioka et al., 2007). Here the only change in the source scheme from the previous studies is the increase in the threshold for leaf

GMDD
4, 3485–3598, 2011

area index for the generation of dust from 0.1 to 0.3 $m^2\ m^{-2}$, to be more consistent with observations of dust generation in more productive regions (Okin, 2008). The cut-off size range for dust emissions is 0.1–2.0 µm (fine dust) and 2.0–10 µm (coarse dust) for MAM7; and 0.1–1.0 µm (accumulation), and 1.0–10 µm (coarse) for MAM3. A lower cut-off size at 1.0 µm is used between accumulation and coarse mode dust in MAM3 to limit the accumulation mode to submicron sizes.

2.1.2 Chemistry

Simple gas-phase chemistry is included for sulfate aerosol. This includes (1) DMS oxidation with radicals (OH and NO_3) to form SO_2; (2) SO_2 oxidation with OH to form H_2SO_4 (gas); (3) H_2O_2 production ($HO_2 + HO_2$); and (4) H_2O_2 loss (H_2O_2 photolysis and $H_2O_2 + OH$). The rate coefficients for these reactions are provided from the MOZART model (Emmons et al., 2010). Oxidant concentrations (O_3, OH, HO_2, and NO_3) are temporally interpolated from monthly averages taken from simulations by a chemistry-climate model (CAM-Chem) (Lamarque et al., 2010).

SO_2 oxidation in bulk cloud water by H_2O_2 and O_3 is based on the MOZART treatment (Tie et al., 2001). The *p*H value in the bulk cloud water is calculated from the electroneutrality equation between the bulk cloud-borne SO_4 and NH_4 ion concentrations (summation over modes), and ion concentrations from the dissolution and dissociation of trace gases based on the Henry's law equilibrium. Irreversible uptake of H_2SO_4 (gas) to cloud droplets is also calculated (Seinfeld and Pandis, 1998). Sulfate produced from SO_2 aqueous oxidation and H_2SO_4 (gas) uptake is partitioned to increase the cloud-borne sulfate mixing ratio in each mode according to the ratio of the cloud-borne aerosol number among modes (i.e., the cloud droplet number associated with each aerosol mode) by assuming droplets associated with each mode have the same size. For MAM7, changes to aqueous NH_4 ion from dissolution of NH_3 are similarly partitioned among modes. SO_2 and H_2O_2 mixing ratios are at the same time reduced due to aqueous phase consumption.

GMDD
4, 3485–3598, 2011

2.1.3 SOA

The simplest treatment of SOA, which is used in many global models, is to assume fixed mass yields for anthropogenic and biogenic precursor VOC's, then directly emit this mass as primary aerosol particles. MAM adds one additional step of complexity by simulating a single lumped semi-volatile organics gas-phase species, which is referred to as SOAG in the model. Fixed mass yields for five VOC categories of the MOZART-4 gas-phase chemical mechanism (Emmons et al., 2010) are assumed, as shown in Table 2. These yields have been increased by a factor of 1.5 during the CAM5 development, considering the large uncertainty with SOA formation. The resulting mass is emitted as the SOAG species. MAM then calculates condensation/evaporation of the SOAG to/from several aerosol modes. The condensation/evaporation is treated dynamically, as described below. The equilibrium partial pressure of the SOAG gas, P^*_m over each aerosol mode m is expressed in terms of Raoult's Law as:

$$P^*_m = \left(\frac{A^{SOA}_m}{A^{SOA}_m + 0.1 A^{POA}_m} \right) P^o, \quad (4)$$

where A^{SOA}_m is SOA mass concentration in mode m, A^{POA}_m is the primary organic aerosol (POA) mass concentration in mode m (10 % of which is assumed to be oxygenated), and P^o is the mean saturation vapor pressure of the SOAG whose temperature dependence is expressed as:

$$P^o(T) = P^o(298\,\mathrm{K}) \times \exp\left[\frac{-\Delta H_{vap}}{R} \left(\frac{1}{T} - \frac{1}{298} \right) \right], \quad (5)$$

where $P^o(298\,\mathrm{K})$ is assumed at 1×10^{-10} atm and the mean enthalpy of vaporization ΔH_{vap} is assumed at 156 kJ mol^{-1}. R is the universal gas constant.

Treatment of this semi-volatile organics gas-phase species and explicit condensation/evaporation provides (1) a realistic method for calculating the distribution of SOA

GMDD
4, 3485–3598, 2011

among different modes and (2) a minimal treatment of the temperature dependence of the gas/aerosol partitioning.

2.1.4 Nucleation

New particle formation is calculated using parameterizations of binary H_2SO_4-H_2O homogeneous nucleation, ternary H_2SO_4-NH_3-H_2O homogeneous nucleation, and boundary layer nucleation. A binary parameterization (Vehkamaki et al., 2002) is used in the 3-mode version, which does not predict NH_3, while a ternary parameterization (Merikanto et al., 2007) is used in the 7-mode version. The boundary layer parameterization, which is applied in the planetary boundary layer (PBL) in both versions, uses the empirical first order (in H_2SO_4) nucleation rate from Sihto et al. (2006), with a first order rate coefficient of $1.0 \times 10^{-6}\,s^{-1}$ as in Wang et al. (2009). The new particles are added to the Aitken mode, and we use the parameterization of Kerminen and Kulmala (2002) to account for loss of the new particles by coagulation as they grow from critical cluster size to Aitken mode size.

2.1.5 Condensation

Condensation of H_2SO_4 vapor, NH_3 (7 mode only), and the semi-volatile organics to various modes is treated dynamically, using standard mass transfer expressions (Seinfeld and Pandis, 1998) that are integrated over the size distribution of each mode (Binkowski and Shankar, 1995). An accommodation coefficient of 0.65 is used for H_2SO_4 (Poschl et al., 1998) and, currently, for the other species too. H_2SO_4 and NH_3 condensation are treated as irreversible. NH_3 uptake stops when the NH_4/SO_4 molar ratio of a mode reaches 2. SOA condensation is reversible, with the equilibrium vapor pressure over particles given by Eq. (4).

In MAM7, condensation onto the primary carbon mode produces aging of the particles in this mode. Various treatments of the aging process have been used in other models (Cooke and Wilson, 1996; Wilson et al., 2001; Riemer et al., 2003; Liu et al.,

GMDD
4, 3485–3598, 2011

2005). In MAM7, a criterion of 3 monolayers of sulfate is used to convert fresh POM/BC particles to the aged accumulation mode. Using this criterion, the mass of sulfate required to age all the particles in the primary carbon mode, $M_{SO_4,age\text{-}all}$, is computed. If $M_{SO_4,cond}$ condenses on the mode during a timestep, we assume that a fraction $f_{age} = M_{SO_4,cond}/M_{SO_4,age\text{-}all}$ has been aged. This fraction of the POM, BC, and number in the mode is transferred to the accumulation mode, along with the condensed soluble species. SOA is included in the aging process. The SOA that condenses in a time step is scaled by its lower hygroscopicity to give a condensed sulfate equivalent.

The two continuous growth processes (condensation and aqueous chemistry) can result in Aitken mode particles growing to a size that is nominally within the accumulation mode size range. We thus transfer part of the Aitken mode number and mass (those particles on the upper tail of the distribution) to the accumulation mode after calculating continuous growth, following the approach of Easter et al. (2004).

2.1.6 Coagulation

Coagulation of the Aitken, accumulation, and primary carbon modes is treated. Coagulation with the larger size modes is much slower and is neglected. Coagulation within each of these modes reduces number but leaves mass unchanged. For coagulation of Aitken with accumulation mode and of primary-carbon with accumulation mode, mass is transferred from Aitken or primary-carbon mode to the accumulation mode. For coagulation of Aitken with primary-carbon mode in MAM7, Aitken mass is first transferred to the primary-carbon mode. This ages some of the primary-carbon particles. An aging fraction is calculated as with condensation, then the Aitken mass and the aged fraction of the primary-carbon mass and number are transferred to the accumulation mode. Coagulation rates are calculated using the fast/approximate algorithms of the Community Multiscale Air Quality (CMAQ) model, version 4.6.

GMDD
4, 3485–3598, 2011

2.1.7 Water uptake

Water uptake is based on the equilibrium Köhler theory (Ghan and Zaveri, 2007) using the relative humidity and the volume-mean hygroscopicity for each mode to diagnose the wet volume-mean radius of the mode from the dry volume-mean radius. The hygroscopity of each component is listed in Table 3. The hygroscopicities here are equivalent to the κ parameters of Petters and Kreidenweis (2007). Note that the measured hygroscopicity of dust varies widely, from 0.03 to 0.26 (Koehler et al., 2009), and the measured hygroscopity of POM can vary from 0.0 for fossil fuel source to 0.06–0.30 for biomass burning source (Liu and Wang, 2010).

2.1.8 Subgrid vertical transport and activation/re-suspension

The vertical transport of interstitial aerosols and trace gases by deep convective clouds, using updraft and downdraft mass fluxes from the Zhang-McFarlane parameterization (Zhang and McFarlane, 1995), is described in Collins et al. (2004). Currently this vertical transport is calculated separately from wet removal, but a more integrated treatment is planned. Cloud-borne aerosols associated with large-scale stratiform cloud are assumed to not interact with the convective clouds. Vertical transport by shallow convective clouds is treated similarly, using mass fluxes from the UW parameterization.

Turbulent transport of the aerosol is given a special treatment with respect to other tracers. To strengthen the coupling between turbulent transport and aerosol activation in stratiform clouds, the implicit time integration scheme used for turbulent transport of heat, energy, and momentum is replaced by an explicit scheme for cloud droplets and aerosol. A sub-timestep calculation is performed for each column based on the minimum turbulent transport time in the column. Turbulent transport is integrated over the sub-time steps using a forward time integration scheme.

Aerosol activation converts particles from the interstitial attachment state to the cloud-borne state. In stratiform cloud, activation is treated consistently with droplet nucleation, so that the total number of particles activated and transferred to the

GMDD
4, 3485–3598, 2011

cloud-borne state equals the number of droplets nucleated. Activation is parameterized in terms of updraft velocity and the properties of all of the aerosol modes (Abdul-Razzak and Ghan, 2000), with both mass and number transferred to the cloud-borne state. The updraft velocity is approximated by the square root of the turbulence kinetic energy, with a minimum value of $0.2\,m\,s^{-1}$. Activation is assumed to occur as updrafts carry air into the base of the cloud (Ghan et al., 1997) and as cloud fraction increases (Ovtchinnikov and Ghan, 2005). In addition, activation is assumed to occur as air is continuously cycled through clouds, assuming a cloud regeneration time scale of one hour. For example, consider a model time step of 20 min, so that 1/3 of the cloud is regenerated in a time step. We essentially dissipate and then reform 1/3 of the cloud in each time step. During dissipation, grid-cell mean cloud droplet number is reduced by 1/3, and 1/3 of the cloud-borne aerosols are re-suspended and converted to the interstitial state. During regeneration, interstitial aerosols are activated in the "new" cloud, and cloud droplet number is increased accordingly. This regeneration has a small impact on shallow boundary layer clouds, but it noticeably increases droplet number in deeper free-tropospheric clouds where vertical mixing is slow. Particles are re-suspended as aerosol when droplets evaporate. This process is assumed to occur as droplets are transferred below or above cloud and as clouds dissipate.

2.1.9 Wet deposition

Aerosol wet removal is calculated using the CAM3.5 wet removal routine (Barth et al., 2000; Rasch et al., 2000) with modifications noted below. The routine treats in-cloud scavenging (the removal of cloud-borne AP) and below-cloud scavenging (the removal of interstitial AP by precipitation particles through impaction and Brownian diffusion).

For stratiform in-cloud scavenging, the stratiform cloud water and precipitation production are used to calculate first-order loss rates for cloud-water at each level. These cloud-water loss rates are multiplied by "solubility factors" to obtain first-order loss rates for cloud-borne AP, from which the removal over a time step are obtained. In previous versions of CAM, the solubility factors could be interpreted as: (the fraction of aerosols

GMDD
4, 3485–3598, 2011

that are in cloud drops) × (an additional tuning factor); in CAM5, they are simply tuning factors. The stratiform in-cloud scavenging only affects the stratiform-cloud-borne AP (which are treated explicitly), and these currently have solubility factors of 1.0. The stratiform in-cloud scavenging does not affect the interstitial AP, and these have solubility factors of 0.0.

For convective in-cloud scavenging of MAM aerosols, the first-order loss rates for cloud-water and convective-cloud-borne AP are calculated similarly as above. Cloud-borne AP within convective clouds are not treated explicitly, so they are diagnosed from the grid-average interstitial AP using prescribed within-convective-cloud activation fractions. The activation fractions currently are 0.0 for the primary carbon mode, 0.4 for the fine and coarse dust modes, and 0.8 for other modes, with lower values reflecting lower hygroscopicity. These factors are applied to both number and mass species within each mode, with one exception. In MAM3, different activation fractions are applied to the coarse mode dust and sea salt (0.4 and 0.8, respectively), and a weighted average is applied to the coarse mode sulfate and number. The solubility (tuning) factors are currently 0.5 for all modes and species. The stratiform-cloud-borne AP reside in the stratiform clouds, and are assumed to not interact with or be affected by convective clouds.

For below-cloud scavenging, the first-order removal rate is equal to: (solubility factor) × (scavenging coefficient) × (precipitation rate). Again, the solubility factor can be viewed as a tuning factor. The scavenging coefficient for interstitial aerosol is calculated as in Easter et al. (2004). This varies strongly with particle size, with lowest values for the accumulation mode. The solubility factor is 0.1. For stratiform-cloud-borne aerosol, there is no below-cloud scavenging, and the solubility factor is 0.0.

Aerosol that is scavenged at one altitude can be re-suspended at a lower altitude if precipitation evaporates. A fraction of the in-cloud scavenged aerosol is re-suspended, and the re-suspended fraction is equal to the fraction of precipitation that evaporates below cloud.

GMDD
4, 3485–3598, 2011

2.1.10 Dry deposition

Aerosol dry deposition velocities are calculated using the Zhang et al. (2001) parameterization with the CAM5 land-use and surface layer information. Gravitational settling velocities are calculated at layers above the surface following Seinfeld and Pandis (1998). Both velocities depend on particle wet size, so average values for aerosol mass and number are calculated for each mode. The velocities for cloud-borne aerosols are calculated based on droplet sizes. Aerosol mixing ratio changes and fluxes from dry deposition and sedimentation throughout a vertical column are then calculated using the CAM3 dust deposition/sedimentation routine (Zender et al., 2003).

2.2 Clouds

In CAM5 two types of clouds exist in each layer: "stratus" and "cumulus". They are horizontally non-overlapped and have their own cloud fraction and condensate. Total cloud fraction is a sum of stratus and cumulus fractions because stratus is assumed to occupy non-cumulus area only. Both the stratus and cumulus are radiatively active.

Liquid and ice stratus fraction are treated separately. Liquid stratus fraction is obtained from the triangular probability density function (PDF) of total specific humidity using an externally specified half width of the distribution (Smith, 1990; Park et al., 2011). Ice stratus fraction is a quadratic function of relative humidity (RH) (Slingo, 1980; Rasch and Kristjansson, 1998), but with consideration of super-saturation over ice and grid-mean ice water content (IWC) (Gettelman et al., 2010). Total stratus fraction is the maximum of liquid and ice stratus fractions by assuming maximum overlap between liquid and ice.

Conversion of water vapor into stratus liquid water content (LWC) is computed using a prognostic saturation adjustment (Park et al., 2011) based on the assumptions that RH within liquid stratus is one and clear sky cannot hold cloud condensate. Thus, any water vapor exceeding saturation specific humidity over water within liquid stratus is

GMDD
4, 3485–3598, 2011

condensed into cloud liquid, while any cloud liquid in the clear sky is evaporated until the clear sky is saturated. The sum of these two processes determines grid-mean net condensation rate. It is assumed that external advective forcing of conservative scalars (total specific humidity including water vapor and cloud condensate, q_t, and liquid potential temperature, θ_l) is uniform across the grid. In order to reduce inconsistency between in-stratus LWC and liquid stratus fraction, a pseudo condensation-evaporation is additionally applied until the in-cloud LWC is within a reasonable range (Park et al., 2011). In case of in-stratus IWC, we adjust the ice stratus fraction such that the resulting in-stratus IWC is within the specified lower and upper limits. These adjustment processes effectively remove both "empty stratus" (i.e., non-zero cloud fraction but zero condensate) and "dense-stratus" (i.e., zero cloud fraction but non-zero condensate). If net evaporation occurs, cloud droplet number concentration decreases. This macrophysical treatment of liquid stratus is detailed in Park et al. (2011). The conversion of water vapor into stratus IWC is expressed in terms of ice particle surface area and supersaturation with respect to ice, as described by Liu et al. (2007) and Gettelman et al. (2010).

Stratus cloud microphysical processes are treated using the double-moment formulation of Morrison and Gettelman (2008) and Gettelman et al. (2008), which predicts number and mass mixing ratios of cloud droplets and ice crystals and diagnoses number and mass mixing ratios of rain and snow. The treatments of droplet and crystal nucleation have been modified. Droplet nucleation is treated consistently with aerosol activation as described above. Ice crystal nucleation is based on Liu et al. (2007), which includes homogeneous nucleation on sulfate competing with heterogeneous immersion on mineral dust in ice clouds (with temperature less than $-37\,^{\circ}\mathrm{C}$) (Liu and Penner, 2005). In the mixed-phase cloud regime ($-37\,^{\circ}\mathrm{C} < T < 0\,^{\circ}\mathrm{C}$), deposition/condensation/immersion nucleation is considered based on Meyers et al. (1992), and contact freezing of cloud droplets through Brownian coagulation with mineral dust is included (Young, 1974). Secondary ice production between $-3\,^{\circ}\mathrm{C}$ and $-8\,^{\circ}\mathrm{C}$ (the Hallet-Mossop process) in mixed-phase clouds is included.

GMDD
4, 3485–3598, 2011

Cumulus consists of "shallow cumulus" and "deep cumulus", which are horizontally non-overlapped and have their own cloud fraction and condensate. Deep cumulus fraction is parameterized as an empirical logarithmic function of deep convective mass flux, while shallow cumulus fraction is computed using shallow convective updraft mass flux and vertical velocity. In-cumulus condensate is internally generated within each shallow and deep convective scheme. The fraction of LWC among total convective condensate is a simple ramping function of temperature.

The shallow convection scheme is described in Park and Bretherton (2009). A single convective updraft plume with certain source air properties (q_t, θ_l and aerosol number and mass densities) is launched at the PBL top. The cloud base mass flux is determined from the mean turbulence kinetic energy (TKE) within the PBL and the inversion strength just above the PBL top (i.e., convective Inhibition). Above the PBL, a portion of convective updraft mass is mixed with the same mass of environmental air. The amount of mass involved in the mixing is proportional to the updraft mass flux and the inverse of geometric height. The mixtures with positive buoyancy or with negative buoyancy with a vertical velocity strong enough to reach a certain level are entrained but the others are detrained. The entrainment and detrainment determine vertical profiles of convective updraft properties, which allow us to compute convective flux and the tendency of any conservative scalars.

At the cumulus top where an inversion layer exists, free air is entrained into the cumulus layer in proportion to the convective updraft mass flux. Within the PBL, the convective updraft flux is a simple linear function with zero value at the surface. The shallow convection scheme also computes the vertical velocity of the cumulus updraft. Core updraft fractional area is the updraft mass flux divided by the updraft vertical velocity and density. The saturated convective fractional area is set to be twice the core updraft fractional area. No convective downdrafts exist in the shallow convection scheme.

Shallow cumulus microphysics is very simple: if in-cumulus condensate is larger than a certain threshold, the excess is precipitated out. This means that no microphysical

GMDD
4, 3485–3598, 2011

interaction exists between aerosol and convective condensate. Thus, aerosol indirect effect associated with cumulus is not simulated even though convective precipitation scavenges aerosols as mentioned above.

Deep convection is represented following a modified version of the Zhang-McFarlane parameterization (Zhang and McFarlane, 1995). The scheme represents an ensemble of buoyant plumes in bulk form and is closed on undilute Convectively Available Potential Energy (CAPE). Modifications to the scheme follow those used in Community Climate System Model version 3.5 (CCSM3.5) coupled climate simulations (Neale et al., 2008; Gent et al., 2009) with the inclusion of sub-grid convective momentum transports (Richter and Rasch, 2008) and the use of an entraining plume model to calculate a dilute CAPE used in the closure (Neale et al., 2008).

2.3 Radiation

Longwave and shortwave radiative transfer are parameterized in CAM5 with the Rapid Radiative Transfer Model for GCMs (RRTMG), a broadband *k*-distribution radiation model developed for application to GCMs (Mlawer et al., 1997; Iacono et al., 2003, 2008). Both RRTMG and the related single-column radiation model RRTM were developed in the context of continual comparison to the Line By Line Radiative Transfer Model (LBLRTM), which is an accurate, efficient and highly flexible line-by-line radiative transfer model that continues to be extensively validated with measured atmospheric radiance spectra from the sub-millimeter to the ultraviolet (Turner et al., 2004; Clough et al., 2005). This realizes the objective of providing improved radiative transfer capability to GCMs that is directly traceable to measurements. Molecular absorbers in RRTMG include water vapor, carbon dioxide, ozone, methane, nitrous oxide, oxygen, nitrogen and the halocarbons in the longwave and water vapor, carbon dioxide, ozone, methane and oxygen in the shortwave. The water vapor continuum is based on CKD_v2.4, and molecular line parameters are based on HITRAN 2000 for water vapor and HITRAN 1996 for all other molecules. RRTMG uses sixteen spectral intervals to represent the longwave region, while the shortwave band is represented by fourteen

GMDD
4, 3485–3598, 2011

spectral intervals. Absorption from aerosols and clouds are included in the longwave, and extinction from aerosols, clouds and Rayleigh scattering are treated in the shortwave.

While RRTMG shares the same basic physics and absorption coefficients as RRTM, it incorporates several modifications to improve computational efficiency, to update the code formatting for easier application to GCMs, and to represent sub-grid scale cloud variations. The complexity of representing fractional cloudiness and cloud overlap in the presence of multiple scattering is addressed in RRTMG with the use of McICA, the Monte-Carlo Independent Column Approximation (Pincus et al., 2003), which is a statistical technique for representing sub-grid scale cloud variability including cloud overlap. Although this method introduces random noise to the cloudy calculation of radiance, the result has been shown to be unbiased. This approach provides the flexibility to represent the vertical correlation of the clouds (i.e. cloud overlap) in some detail by imposing an assumed relation (such as random or maximum-random) among the stochastic cloud arrays across the vertical dimension. The maximum-random cloud overlap assumption, in which adjacent cloud layers in the vertical are presumed to overlap maximally and non-adjacent cloudy layers are assumed to overlap randomly, is used for this work.

Aerosol radiative effects are treated in RRTMG through the specification of their optical properties within each spectral interval. Aerosol optical properties are parameterized in terms of wet refractive index and wet surface mode radius according to Ghan and Zaveri (2007), except that volume mixing rule is used to calculate the volume-mean wet refractive index for mixtures of insoluble and soluble particles. We found little difference between the volume mixing treatment and the Maxwell-Garnett mixing rule. Refractive indices for most aerosol components are taken from OPAC (Hess et al., 1998), but for black carbon the value (1.95, 0.79i) from Bond and Bergstrom (2006) is used. Densities for each component are listed in Table 4.

Liquid cloud optics are implemented as a lookup table in terms of the lambda and gamma parameters of the gamma size description provided by the methods of Morrison

GMDD
4, 3485–3598, 2011

and Gettelman (2008). The table elements are the wavelength and size-distribution averages of the extinction, single-scattering albedo, and asymmetry parameter resulting from Mie computations (Wiscombe, 1979) using the index of refraction of pure water. These elements are a function of selected lambda and gamma values that cover the range of values generated by the stratiform microphysical code. The effect of in-cloud liquid water variability is not included in the generation of the lookup tables. The values of lambda and gamma for shallow and deep cumulus clouds are assumed to be the same as those for stratiform clouds if they exist in the same grid cell; otherwise they are set to constant values corresponding to a shape parameter μ of 5.3 and an effective diameter of 25 µm.

CAM5 also uses a look-up table approach for the ice cloud optics. The mass-weighted extinction (volume extinction coefficient/ice water content) and the single scattering albedo, ω_o, in the ice optics look-up table were produced by the modified anomalous diffraction approximation (MADA), described by Mitchell (2000; 2002) and Mitchell et al. (2006). MADA calculates the extinction and absorption coefficients, β_{ext} and β_{abs}, and thus cloud optical depth and ω_o. The asymmetry parameter g is determined as a function of wavelength and ice particle size and shape as described by Gettelman et al. (2010). A shape recipe for ice crystals was assumed when calculating these optical properties, as well as for snow since the radiative effect of snow is also included (Gettelman et al., 2010).

Snow darkening from aerosol deposition is treated uniquely within the land and sea-ice components of CCSM. Deposited aerosols are apportioned into species conforming to the "bulk" aerosol scheme (Rasch et al., 2001) to which the Snow, Ice, and Aerosol Radiative (SNICAR) model was originally coupled (Flanner et al., 2007). Mapping of species from the modal aerosol scheme to bulk aerosols is listed in Table 5. In this mapping scheme, interstitial and in-cloud species are grouped together. Wet- and dry deposited-species are also treated together, once they have been received by the surface model components.

GMDD
4, 3485–3598, 2011

For each snowpack constituent, we assign mass-extinction coefficients ($m^2\,kg^{-1}$), single-scatter albedos, and scattering asymmetry parameters according to the spectral grid applied in each host model. SNICAR, embedded in the land model, applies five spectral bands (0.3–0.7, 0.7–1.0, 1.0–1.2, 1.2–1.5, and 1.5–5.0 µm), whereas the sea-ice model utilizes a delta-Eddington scheme (Briegleb and Light, 2007) with three bands (0.3–0.7, 0.7–1.19, 1.19–5.0 µm). Hyper-spectral (470 band) optical properties are computed offline with Mie Theory, and weighted into these broad bands according to a surface-incident spectral flux distribution typical of mid-latitude winter (Flanner et al., 2007). Descriptions on the snow and sea-ice radiative transfer schemes, including tables with optical properties of all impurities and details of the weighting schemes applied to merge impurity and ice optical properties, are found, respectively, in Oleson et al. (2010) and Briegleb and Light (2007). We plan to implement future versions of the snow model that represent aerosols more consistently with the MAM3 and MAM7 schemes discussed here.

2.4 Turbulence

The treatment of turbulence in CAM5 is described by Bretherton and Park (2009) and its performance is evaluated by Park and Bretherton (2009). The scheme expresses down-gradient diffusion of moist-conserved scalars and horizontal momentum within turbulent layers in terms of a TKE diagnosed from the local TKE production-transport-dissipation balance. The strong longwave radiative cooling at the cloud top is explicitly included in the TKE balance equation, which allows more realistic simulation of marine stratocumulus clouds. An explicit entrainment closure is used to diagnose an effective "entrainment diffusivity" at the edge of turbulent layers. All the scalars except aerosols and cloud liquid droplet number are diffused in an implicit way to reduce numerical instability due to the long model integration time step (1800 s) in CAM5.

GMDD
4, 3485–3598, 2011

2.5 Resolved Transport

Transport of water and other trace species is calculated with the Lin-Rood finite volume dynamical core (Lin and Rood 1996; Lin 2004). Gent et al. (2009) describe the performance of this dynamical core at 0.5° resolution with CAM3.5 physics. Here we use the 1.9° latitude × 2.5° longitude resolution with 30 vertical layers in CAM5. There are five vertical layers below 900 hPa.

3 Aerosol distributions and budgets

All simulations are performed with the stand-alone version CAM5.1 using climatological sea surface temperature and sea ice and anthropogenic aerosol and precursor gas emissions for the year 2000. The model is integrated for 6 yr, and results from the last 5 yr are used in this study. In this section model simulated global distributions and budgets for different aerosol species are analyzed and comparisons are made between MAM3 and MAM7.

3.1 Simulated global aerosol distributions

Figure 3a,b shows annual mean vertically integrated (column burden) mass concentrations of sulfate, BC, POM, SOA, dust and sea salt from MAM3, and the relative difference of these concentrations between MAM7 and MAM3, respectively. These aerosol species concentrations are summations over all available modes (e.g., the POM concentration in MAM7 includes contributions from the primary carbon and accumulation modes). Sulfate has maximum concentrations in the industrial regions (e.g., East Asia, Europe, and North America). The distribution patterns and absolute values of sulfate concentration are very similar (within 10 %) between MAM3 and MAM7 (Fig. 3b). This is expected since most of sulfate burden (∼ 90 %) is in the accumulation mode (see sulfate budget in Sect. 3.2). This is also the case for SOA, which has high concentrations over the industrial regions and in the biomass burning regions (e.g., Central

GMDD
4, 3485–3598, 2011

Africa and South America). The differences between MAM3 and MAM7 are generally small (within 10 %). POM column concentrations have spatial distributions and magnitudes similar to SOA, but are lower in Europe, Northeast US and South America, and higher in Central Africa. The distribution patterns of BC burden concentrations are similar to those of POM, but have relatively larger contributions from the industrial regions because of different emission factors of BC/POM from different sectors. Dust burden concentrations have maxima over strong source regions (e.g., Northern Africa, Northwest Asia, and Australia), and over the outflow regions (e.g., in the Atlantic and in the Western Pacific). Sea salt burden concentrations are high over the storm track regions (e.g., the Southern Ocean) where wind speeds and emissions are higher, and in the subtropics of both hemispheres where precipitation scavenging is weaker.

One major difference between MAM3 and MAM7 is the treatment of primary carbonaceous aerosols (POM and BC). These aerosols are instantly mixed with sulfate and other components in the accumulation mode in MAM3 once they are emitted, and thus subject to wet removal by precipitation due to the high hygroscopicity of sulfate. In MAM7, carbonaceous aerosols are emitted in the primary carbon mode and aged to the accumulation mode due to condensation of H_2SO_4 (gas), NH_3 (gas) and semi-volatile organics and coagulation with Aitken and accumulation mode. Therefore we expect lower wet removal rates and higher concentrations for POM and BC in MAM7 than in MAM3. However, since we use a hygroscopicity (κ) of 0.10 for POM (to account for the soluble nature of biomass burning aerosols), POM and BC in the primary carbon mode in MAM7 are subject to wet scavenging before aging into the accumulation mode. As shown in Fig. 3b, differences in column burden concentrations of POM and BC are within 10 % on the global scale between MAM3 and MAM7. However, concentrations from MAM7 can be higher by up to 40 % in some source regions, e.g., in Siberia and Indonesia. The sensitivities of model results to a different hygroscopicity of POM ($\kappa = 0.0$) and to a different criterion of 8 monolayers for the aging of primary carbonaceous aerosols to the accumulation mode will be described in Sect. 5.

GMDD
4, 3485–3598, 2011

Other major differences between MAM3 and MAM7 are cut-off size (diameter) ranges and mixing states assumed for dust and sea salt, as discussed in Sect. 2.1. The fine dust mode is separated from the accumulation mode in MAM7, while in MAM3 it is merged into the accumulation mode. There is a fine sea salt mode in MAM7, which is merged to the accumulation mode in MAM3. Coarse dust and sea salt mode in MAM7 are merged to a single coarse mode in MAM3. Dust column burden concentrations are generally higher in MAM7 (Fig. 3b) with global dust burden increased by ∼10 %. In some regions away from dust sources the difference can reach 60 %. This will be further discussed in the budget analysis in Sect. 3.2. Significant changes occur for sea salt with sea salt column burden concentrations reduced by ∼30 % in MAM7. Besides differences in mixing states and cut-off size ranges of sea salt, the standard deviations σ_g of log-normal distributions are reduced from 2.0 for fine and coarse sea salt modes in MAM7 to 1.8 for the accumulation and coarse mode in MAM3 for the merging with other species. The larger σ_g in MAM7 increases the mass-weighted sedimentation velocity of coarse-mode sea salt by about 65 %, which causes the lower sea salt mass concentrations in MAM7.

Figure 4 shows the annual and zonal mean distributions of sulfate, BC, POM, SOA, dust and sea salt mass concentrations in MAM3. Anthropogenic sulfate in the Northern Hemisphere (NH) mid-latitudes is lifted upward and transported towards the North Pole in the upper troposphere. Other peak concentrations of BC, POM and SOA near the tropics in the biomass burning regions are transported upwards and towards the upper troposphere in the Southern Hemisphere (SH). Dust particles are uplifted into the free troposphere, since dust emission is often produced by frontal systems. In comparison, sea salt is mostly confined below 700 hPa. This is because sea salt particles have larger wet sizes due to the water uptake over the oceans, which produces stronger wet removal and gravitational settling of sea salt particles towards the surface. Consistent with Fig. 3b, sea salt concentration in the zonal mean distribution is lower in MAM7 than that in MAM3 mainly due to the larger standard deviations of log-normal distributions for fine and coarse sea salt modes in MAM7, while differences are much smaller for other

GMDD
4, 3485–3598, 2011

aerosol species (figures not shown). Concentrations of BC, POM, SOA, and dust are all very low in the lower troposphere at NH high latitudes, due to efficient wet removal during transport from source regions.

Figure 5 shows the annual mean number concentration of aerosol in Aitken, accumulation and coarse mode in the surface layer from MAM3 and MAM7 at standard temperature and pressure (STP) (1013.25 hPa, 273.15 K). For a direct comparison with MAM3, we add the aerosol number in the MAM7 primary carbon, fine sea salt, and fine dust mode with sizes between 0.1–1.0 µm (by splitting the fine dust mode into 0.1–1.0 and 1.0–2.0 µm using model calculated dry mode radius) into the accumulation mode in MAM7. In the same way we add the aerosol number in the coarse sea salt, fine dust mode with sizes between 1.0–2.0 µm and coarse dust mode into a single coarse mode in MAM7. As indicated in Fig. 5, accumulation mode number concentrations in both MAM3 and MAM7 are higher over the continents due to the primary emissions of sulfate, POM and BC, and growth of aerosol particles from Aitken to accumulation mode. In the industrial regions (e.g., East and South Asia and Europe) and in the biomass burning regions (e.g., maritime continents, Central Africa and South America) the number concentration can exceed 1000 cm^{-3}. Accumulation mode number concentrations over oceans can be high in the continental outflow regions (e.g., West Pacific, tropical Atlantic), while in the remote areas, the concentrations are less than 100 cm^{-3}. We do not find significant differences in accumulation mode aerosol number concentrations between MAM3 and MAM7.

Aerosol number concentrations in the Aitken mode in MAM3 and MAM7 are high over the continents with strong sulfur emissions (e.g., in East Asia, Europe, and in North America). Aitken mode aerosol number concentrations are very low (less than 40 cm^{-3}) in the biomass burning regions because primary aerosol particles from the biomass burning source are emitted in the accumulation mode in MAM3 and in the primary carbon mode in MAM7, in both cases with a 0.08 µm number mode diameter (see Table 1). Over remote oceanic and Antarctic regions, aerosol number concentrations in Aitken mode can reach 500 cm^{-3}. This is primarily due to strong aerosol nucleation

GMDD
4, 3485–3598, 2011

in these regions where accumulation mode number concentrations are extremely low ($< 40\,cm^{-3}$), and sea salt emissions also contribute in the SH storm track region near 60° S where surface winds are strong. We see higher Aitken mode number concentrations in MAM7 than those in MAM3 over these remote regions. H_2SO_4 concentrations are somewhat higher in MAM7, resulting in more aerosol nucleation. Aerosol number concentrations in the coarse mode are higher over the sea salt and dust source regions and in the dust outflow regions and are in the range of less than $10\,cm^{-3}$. Interestingly, even though sea salt mass concentrations in the coarse mode in MAM3 are significantly higher than in MAM7 over the oceanic regions, coarse mode aerosol number concentrations there are similar between MAM3 and MAM7. This is because the number-weighted settling velocity for coarse mode sea salt number is rather insensitive to small σ_g changes. As a result, the coarse mode median diameters are larger in MAM3 due to higher mass concentrations (figure not shown). A breakdown of total accumulation mode number concentration in MAM7 shown in Fig. 5 is as follows: fine sea salt contributes about 5–20 cm^{-3} over oceans; fine dust contributes 50–100 cm^{-3} over major source regions (e.g., North Africa and North China) and 10–20 cm^{-3} in the dust outflow regions. Primary carbon aerosol contributes 10–30 % over the industrial region (e.g., East Asia and Europe) and 30–70 % in the biomass burning regions (e.g., Central Africa, South America, Indonesia, and Russia), and the rest is from the accumulation mode aerosol.

Figure 6 is the same as Fig. 5 except for annual and zonal mean aerosol number concentrations in Aitken, accumulation and coarse modes. Aitken mode aerosol number concentrations show a prominent peak in the tropical upper troposphere and over the South Pole, where temperature is low and relative humidity (RH) is high along with low preexisting aerosol surface areas. Note that we consider the number loss of the new particles by coagulation as they grow from the critical cluster size (a few nanometers) to Aitken mode size (0.02–0.08 µm). Consistent with surface number concentrations shown in Fig. 5, Aitken mode aerosol number concentrations are generally higher in MAM7 than in MAM3. Accumulation mode aerosol particles are transported into

GMDD
4, 3485–3598, 2011

the middle and upper troposphere with number concentrations of 20–100 cm^{-3} above 600 hPa. This is contributed from biomass burning emission injected at 0–6 km in the tropics. The spatial distribution of coarse mode aerosol number concentration is associated with the spatial distribution of dust and sea salt (Fig. 4), and slightly higher number concentrations simulated with MAM3 than with MAM7.

Figure 7 shows the annual averaged global distribution of CCN number concentration at 0.1 % supersaturation (S) in the surface layer in MAM3 and MAM7. Distribution patterns of CCN concentration closely follow those of accumulation mode number concentration and have high concentrations (400–1000 cm^{-3}) in the industrial regions due to the dominance of sulfate with a high hygroscopicity. CCN concentration at $S = 0.1$ % has similar ranges in the biomass burning regions as in the industrial regions because biomass burning aerosol is assumed to be water-soluble. CCN concentration at $S = 0.1$ % is lower than 100 cm^{-3} over oceans, except in the continental outflow regions. CCN concentration at $S = 0.1$ % is 20–40 % of the total accumulation mode number over the continents and outflow regions. Over the remote oceans CCN concentration at $S = 0.1$ % is 70–90 % of accumulation mode aerosol number concentration. CCN concentration in MAM3 is higher than that in MAM7 over the oceanic regions. This is due to merging the 0.3–1.0 µm size range of MAM7 fine sea salt into the accumulation mode in MAM3, increasing MAM3 accumulation mode median size, and thus allowing more of the accumulation mode particles to be CCN at $S = 0.1$ %, although coarse mode aerosol number concentrations are similar there (Fig. 5).

3.2 Annual global budgets of aerosols and precursor gases

Tables 6–12 give the global budgets of aerosol species and their precursor gases in MAM3 and MAM7. Budgets of gas species are compared to a range of model results collected from literature by Liu et al. (2005). For aerosol species, the averages and standard deviations of available models participated in the AeroCom project (Textor et al., 2006) are listed for comparison as the "AeroCom".

GMDD
4, 3485–3598, 2011

The DMS emission from ocean is 18.2 Tg S yr^{-1}, which is balanced by the gas oxidation of DMS to form SO_2 and other products (e.g., MSA). DMS burden is 0.067 Tg S with a lifetime of 1.3 days for both MAM3 and MAM7 (Table 6), which is within the range of model results reported in the literature. SO_2 emission (64.8 Tg S yr^{-1}) is at the low end of the range of model results. Production of SO_2 from DMS oxidation (15.2 Tg S yr^{-1}) together with SO_2 emission is balanced by SO_2 losses by dry and wet deposition, and by gas- and aqueous-phase oxidation. The wet deposition loss of SO_2 is at the high end of the range from the literature and is comparable to that of dry deposition loss. This is because wet deposition of gas species in CAM5 uses the MOZART treatment (Emmons et al., 2010), which assumes that the wet removal rate coefficient of SO_2 is the same as that of H_2O_2 (g) and assumes full gas retention during droplet freezing. 66–68 % of chemical loss of SO_2 is through the aqueous phase oxidation. One noticeable difference between MAM3 and MAM7 is that there is a larger aqueous phase chemical loss in MAM7. This is because NH_3 (g) and ammonium are explicitly treated in MAM7, and NH_3 (g) dissolves in cloud water to increase pH values to be larger than those with the assumed form of NH_4HSO_4 in MAM3 (figure not shown). Thus this enhances the contribution from aqueous phase SO_2 oxidation by O_3 (Seinfeld and Pandis, 1998). The global burden of SO_2 is 0.35 (MAM3) and 0.34 Tg S (MAM7) with a lifetime of 1.60 (MAM3) and 1.55 days (MAM7), which are within the range of the literature.

H_2SO_4 (g) is produced by gas phase SO_2 production and is lost by condensation on pre-existing aerosol (by 96 %) and aqueous phase uptake by cloud water (by 4 %) (Table 6). The losses by dry deposition (0.01 %) and nucleation (0.2 %) are negligibly small. H_2SO_4 (g) has a global burden of ~ 0.00040 Tg S, and a lifetime of 15 min, in agreement with limited reports from the literature.

Sulfate aerosol is produced from aqueous phase SO_2 oxidation, and to a lesser extent from H_2SO_4 (g) condensation on pre-existing aerosol, and is lost mainly by wet scavenging (Table 7). MAM7 has a smaller percentage of aqueous phase sulfate production from H_2O_2 compared to MAM3 for the reason mentioned above. The global burden is ~ 0.46 Tg S which is lower than that of the AeroCom multi-model mean. The

GMDD
4, 3485–3598, 2011

lifetime is 3.7–3.8 days, which is close to the AeroCom multi-model mean (4.12 days). The lower sulfate burden is primarily due to the smaller production from SO_2 in the model (44–46 Tg S yr^{-1}) compared to AeroCom multi-model mean (59.67 Tg S yr^{-1}). This smaller production in CAM5 may be due to smaller SO_2 sources and higher SO_2 wet removal rate coefficient, so that less SO_2 is available for gas/aqueous phase oxidation to form sulfate. Most sulfate (89–96 %) is in the accumulation mode, which has a larger total surface area for H_2SO_4 (g) condensation and a higher contribution to CCN (at $S = 0.1$ %) for aqueous phase oxidation.

The NH_3 and NH_4 cycles are explicitly treated in MAM7. Their budgets are given in Table 8. The source of NH_3 from emission is balanced by losses due to the condensation onto the preexisting aerosol to form NH_4 and to a lesser extent due to the dry and wet deposition. The global NH_3 burden is 0.064 Tg N with a lifetime of 0.48 day. The formation of NH_4 from condensation is balanced by the loss mostly due to wet deposition. The global NH_4 burden is 0.24 Tg N with a lifetime of 3.4 days. There is a small budget term for NH_3 and NH_4 related to the partitioning between NH_3 and NH_4 in cloud water based on the effective Henry's law. NH_3 and NH_4 budgets are compared to a few available studies in the literature (Table 8). The NH_3 and NH_4 budgets are close to those from a modeling study by Feng and Penner (2007), although our burdens are slightly lower and lifetimes slightly shorter. The molar ratio of ammonium to sulfate (NH_4/SO_4) in aerosol has a global annual average value of 1.2. In the continental boundary layer, it is near 2 for many regions but is lower over desert, boreal, and polar regions, with lowest values (annual average < 0.1) over Antarctica. In the marine boundary layer, the ratio is near 2 in the tropics, is generally less than 1 in the NH mid-latitudes, and is in the 0.5–1.5 range in the SH mid-latitudes. The ratio is less than 1.0 in much of the free troposphere, except in the tropics where ratios of 1.5–2.0 appear, especially over continents. These results indicate different neutralization of SO_4 by NH_4 in aerosol in MAM7 compared to a molar ratio of 1.0 with NH_4HSO_4 assumed in MAM3.

Table 9 gives the budgets of POM and SOA. The POM burden is 0.63–0.68 Tg, which is less than half of the AeroCom mean (1.7 Tg). This is mainly because the IPCC AR5

GMDD
4, 3485–3598, 2011

POM emissions used here are only about half of the AeroCom multi-model mean. Also, for many of the AeroCom models, biogenic SOA is included in the POM. The POM lifetime is 4.5–4.9 days, which is lower than that of the AeroCom multi-model mean (6.54 days), due to the 20 % higher wet removal rate in this study related to the precipitation formation in CAM5.1 (Table 9). We note that wet removal rate for sulfate in this study is close to that of the AeroCom multi-model mean, and thus the sulfate lifetimes are similar between this study and the AeroCom multi-model mean (Table 7). This reflects different geographic distributions of sulfate versus POM concentration (Fig. 3). The POM burden is slightly lower and lifetime slightly shorter in MAM3 than in MAM7 due to the instant aging of POM and mixing with sulfate and other components in the accumulation mode in MAM3, which produces faster wet removal due to the higher hygroscopicity of sulfate than that of POM (Table 3). In MAM7, about 15 % of POM is in the primary carbon mode and has a lifetime of 0.72 days due to the fast aging to the accumulation mode. The burden of SOA is 1.15 Tg and has a lifetime of 4.1 days. The SOA lifetime is shorter than that of POM. This is confirmed by the larger wet removal rate (by 20–30 %) of SOA than that of POM. The reason is that SOA is formed from the partitioning of semi-volatile organic gas species emitted at the surface in the model and thus experiences wet removal by precipitation in the boundary layer, while biomass burning emissions are elevated and occur in different seasons and different geographical regions. Another reason for the shorter SOA lifetime is the larger hygroscopicity (0.14) of SOA than that (0.10) of POM. The SOA burden is higher and lifetime shorter than the means from other studies collected in Farina et al. (2010), which, however, have very large standard deviations (>100 %).

The simulated global BC burden is 0.088–0.093 Tg (Table 10), which is only 40 % of AeroCom multi-model mean (0.24 Tg). One reason for the difference is that the IPCC BC emission is 65 % of the AeroCom multi-model mean. Another reason is that the wet removal rate is 60 % higher in this model than the AeroCom multi-model mean. The simulated BC lifetime is 4.2–4.4 days, much lower than the AeroCom multi-model mean (7.1 days). BC burden is slightly higher and lifetime slightly longer in MAM7 than

GMDD
4, 3485–3598, 2011

in MAM3. About 10 % of BC is in the primary carbon mode with a lifetime of 0.50 day in MAM7, which is shorter than that of POM (0.72 day). BC has relatively more fossil fuel and less biomass burning emissions compared to POM, indicating more rapid aging for industrial versus biomass burning source regions.

Table 11 gives the budgets for dust. The simulated dust emission (2900–3100 Tg yr^{-1}) is ∼60 % higher than the AeroCom multi-model mean (1840 Tg yr^{-1}), and dust has a burden of 22–25 Tg, close to the AeroCom multi-model mean (19 Tg), because of the shorter lifetime (2.6–3.1 days) in the simulation than the AeroCom mean (4.14 days). The reason for the shorter lifetime is due to the larger wet removal rate (by ∼60 %) than the AeroCom mean. Gravitational settling plays a dominant role (∼90 %) in the total dry deposition, larger than the AeroCom mean (46.2 %). The burden is slightly lower and lifetime shorter in MAM3 than in MAM7, respectively. This is due to the larger dry deposition rate (Table 11) in MAM3 with a different cut-off size from that in MAM7. The internal mixing of dust with other components in MAM3 also increases the wet removal rate of dust in MAM3 compared to that in MAM7. The sensitivity of simulated dust to different cut-off sizes will be investigated in a future study.

The simulated sea salt emission is ∼5000 Tg yr^{-1}, slightly lower than the AeroCom median (6280 Tg yr^{-1}), and substantially lower than the AeroCom mean (16 600 Tg yr^{-1}) with a standard deviation of ∼200 % (Table 12). Note that some of the AeroCom models treated sea salt larger than 10 µm diameter. The burden is 7.58 Tg and lifetime 0.55 day in MAM7, similar to the AeroCom means. The dry and wet deposition rates are close to the AeroCom medians, and so is the contribution of sedimentation to dry deposition (60.8 %) in MAM7. In MAM3, the wet deposition rate does not change much from that in MAM7. However, the dry deposition rate is ∼40 % less due to the smaller standard deviation σ_g of the coarse mode in MAM3 (1.8), compared with that for coarse sea salt mode in MAM7 (2.0). Therefore, the sea salt burden in MAM3 is 10.4 Tg and lifetime 0.76 day, which is ∼37 % higher than that in MAM7, respectively. Most (∼90 %) of sea salt is in the coarse mode in both MAM3 and MAM7.

GMDD
4, 3485–3598, 2011

4 Model evaluation

4.1 Aerosol mass concentration

Figures 8 and 9 compare simulated annual mean SO_2 and sulfate concentrations at the surface from MAM3 and MAM7 with observations from the Interagency Monitoring of Protected Visual Environment (IMPROVE) sites in the United States (http://vista.cira.colostate.edu/improve), and the European Monitoring and Evaluation Programme (EMEP) sites (http://www.emep.int). Clearly the model overestimates SO_2 in both Eastern and Western United States, while it performs better at the European EMEP sites, although there are still overestimations there. Overall modeled sulfate agrees with observations within a factor of 2 for most sites in the United States and Europe. Sulfate in the Western United States is overestimated by the model. The performance of MAM3 and MAM7 in simulating SO_2 and sulfate is similar for these sites in both regions. However, modeled SO_2 concentrations are slightly lower in MAM7 than in MAM3 (see model mean for these sites), while modeled sulfate concentrations are higher in MAM7, especially in the European sites (by 10–20 %), indicating faster conversion of SO_2 to sulfate in MAM7. This is consistent with the larger aqueous-phase chemical conversion of SO_2 to sulfate in MAM7 (as discussed in Sect. 3.2) due to the explicit treatment of NH_3 (g) and ammonium in MAM7. In Europe with higher NH_3 concentrations than those in United States (not shown), the increase in sulfate concentrations in MAM7 is larger.

Figure 10 compares annual mean sulfate concentrations simulated at the surface from MAM3 and MAM7 with observations from an ocean network operated by the University of Miami (Prospero et al., 1989; Savoie et al., 1989, 1993; Arimoto et al., 1996). Simulated sulfate concentrations systematically underestimate the observations at these ocean sites for both MAM3 and MAM7 probably due to too high wet removal rates, although the correlation coefficients between modeled and observed concentrations are ~0.98.

GMDD
4, 3485–3598, 2011

Figures 11–14 compare simulated annual mean BC and OC/OM from MAM3 and MAM7 with those observed at the IMPROVE sites, EMEP sites, and those compiled by Liousse et al. (1996), Cooke et al. (1999) and Zhang et al. (2007). Modeled BC concentrations agree with observations reasonably well (mostly within a factor of 2) at the IMPROVE sites (Fig. 11a), while the model significantly overestimates observed OC concentrations by more than a factor of 2 especially in the Eastern US (Fig. 12a). The OC high bias is improved when the 50 % SOA yield increase (Sect. 2.1.3) is removed. The model underestimates observed BC and OC concentrations at the EMEP sites (Figs. 11b and 12b). Modeled OC and BC generally capture the spatial variations of those compiled by Liousse et al. (1996), Cooke et al. (1999) and Zhang et al. (2007). However, BC concentrations are significantly underestimated in remote regions and at some Pacific and Atlantic locations, suggesting the too strong wet removal of BC during its transport from the source regions. These results for MAM3 and MAM7 are very similar due to the hygroscopicity ($\kappa = 0.1$) used for POM. Modeled OM concentrations are within a factor of 2 of observations at most sites compiled by Zhang et al. (2007).

We compare model simulated vertical profiles of BC with aircraft measurements from several field campaigns in the tropics and subtropics, over mid-latitude North America (Fig. 15), and at high latitudes (Fig. 16). These measurements were made by a Single Particle Soot absorption Photometer (SP2) (Schwarz et al., 2006). Koch et al. (2009) gave a detailed description of aircraft flights and data processing. The mean as well as median and standard deviation are shown in the figures when available. Modeled BC profiles are based on monthly results interpolated to the average latitude and longitude of flight tracks. Measured BC concentrations show a strong gradient (by 1–2 orders of magnitude) from the boundary layer to the free troposphere in the tropics (CR-AVE and TC4) and subtropics (AVE Houston). Modeled BC concentrations from MAM3 and MAM7 show a smaller decrease with altitude in the free troposphere, thus overestimating observations above 600–500 hPa by a factor of 10, although the agreement is better (within the data standard deviation) in the boundary layer. This overestimation of BC concentration in the free troposphere is also shown in almost all the models

GMDD
4, 3485–3598, 2011

participating in the AeroCom project (Koch et al., 2009). The campaign in the mid-latitudes of North America (CARB) encountered strong biomass burning plumes, and BC concentrations show less reduction below ~700 hPa. The modeled BC concentrations agree with the data median (more representing the background condition) better than with the data mean.

Unlike those in the lower latitudes, observed BC concentrations at polar latitudes are relatively uniform up to 400 hPa, especially in spring (Fig. 16). This is due to the transport of pollutants to the Arctic from mid-latitudes by meridional lofting along isentropic surfaces. Modeled BC concentrations from MAM3 and MAM7 are significantly lower than those observed below 200 hPa, resulting from the too efficient scavenging of BC by convective and stratiform clouds during its transport and/or the model with the climatological emissions missing some local fire events. This underestimation of BC below 200 hPa is also simulated by most of the AeroCom models (Koch et al., 2009). The too efficient removal of BC is related to excessive liquid clouds in the NH in CAM5.1 (H.-L. Wang, personal communication) and/or too fast wet removal of fossil fuel BC (see Sect. 5 for sensitivity tests). Therefore, although there is too much BC uplifted in the free troposphere by convection in the lower latitudes (Fig. 15), there is much less BC arriving in the higher latitudes due to fast removal by precipitation. The comparison of modeled BC with observations is better in the summer probably due to the better simulation of clouds then. Model results between MAM3 and MAM7 are similar due to the hygroscopic nature of POM used in the model. Sensitivity tests (MAM7-k and MAM7-aging) will be discussed in Sect. 5 to further examine the impact on modeled BC profiles.

Figure 17 compares modeled profiles of BC with SP2 measured BC concentrations during the HIAPER Pole-to-Pole Observations campaign (HIPPO1) conducted above the remote Pacific from 80° N to 67° S during a two-week period in January 2009 (Schwarz et al., 2010). We note that this kind of comparison is for reference purposes due to the short duration of observations. The observed BC profiles show significant differences between different latitude zones. Upper tropospheric BC concentration is

GMDD
4, 3485–3598, 2011

much lower (by two orders of magnitude) than that in the lower troposphere in the tropics (20° S to 20° N), which is consistent with observations included in Koch et al. (2010) as discussed in Fig. 15. The observed BC profiles show much less variation up to 200 hPa in both NH and SH mid-latitudes. Observed BC concentration increases with altitude in the SH high latitudes, reflecting the upper level transport of BC from biomass burning sources regions in South America and Southern Africa. In contrast, observed BC concentration decreases with altitude in the NH high latitudes (60–80° N) with very high BC concentrations above 50 ng kg^{-1} near the surface. This is different from the more uniform BC profiles observed in April (Fig. 16). MAM3 and MAM7 capture the vertical variations of BC concentration reasonably well in the SH high latitudes and NH and SH mid-latitudes. However, modeled BC shows less vertical reduction in the tropics, thus significantly overestimating measurements in the upper troposphere. This overestimation is also shown in the model median and mean of AeroCom models, which is attributed to the insufficient wet removal of BC in the models by convective clouds (Schwarz et al., 2010). Similar to the results in Fig. 16 for the NH high latitudes in April, modeled BC significantly underestimates the observations below 300 hPa. There is little difference between model BC in MAM3 and MAM7, although BC concentrations from MAM7 are slightly higher. We will further discuss the impact of BC aging on modeled BC profiles in Sect. 5.

Figures 18 and 19 compare the simulated annual mean dust concentrations and dust deposition fluxes at the surface from MAM3 and MAM7 with observations collected by Mahowald et al. (2009). As for sulfate, dust concentrations are underestimated at many sites especially in MAM3. The underestimation is reduced in MAM7, which is consistent with the higher dust burden and concentration in MAM7. Modeled dust deposition fluxes are also lower than limited observational data.

Figure 20 compares the simulated annual mean sea salt concentrations at the surface from MAM3 and MAM7 with observations obtained at the ocean sites operated by the University of Miami. Most of the simulated sea salt concentrations are within a factor of 2 of the observations although there is large scatter between the model and

GMDD
4, 3485–3598, 2011

observations, and correlation coefficients are low (0.23–0.25) in part due to the narrow range of the model and observed sea salt concentrations. MAM7 simulates lower sea salt concentrations with lower model mean and correlation coefficient than those of MAM3.

4.2 Aerosol number concentration and size distribution

Figure 21 compares simulated aerosol size distributions in the marine boundary layer with observations from Heintzenberg et al. (2000). The observational data were compiled and aggregated onto a 15° × 15° grid. We sampled the model results over the same regions as those of the observations. Observations show bi-modal size distributions for all the latitudinal bands with a mode median diameter of 0.03 to 0.06 µm for the Aitken mode, and 0.1–0.2 µm for the accumulation mode. There are higher Aitken mode number concentrations in the SH extratropics due to the boundary layer aerosol nucleation and entrainment of aerosol from the free troposphere. The model is able to reproduce the bi-modal size distributions. However, the model underestimates the Aitken mode number concentrations in the SH (15° S–60° S) and NH (15° N–30° N), which suggests that the boundary layer nucleation in these remote regions is too weak, the ultrafine sea salt emission flux is too small, or the model misses an organic ocean source. The results for the SH are consistent with Pierce and Adams (2006). In the NH mid-latitudes, the model underestimation of Aitken mode number concentration may also suggest that the anthropogenic influence is too weak. The model underestimates the accumulation mode number concentrations in almost all latitude bands. This suggests that the model may have too low fine sea salt emission flux, too strong wet removal of sea salt in the marine boundary layer and anthropogenic aerosols during the transport from the continents, and/or missing organic source from oceans. There are higher Aitken mode aerosol number concentrations in MAM7 than those in MAM3 in all these marine zonal bands, consistent with the higher nucleation rates of aerosol in MAM7, as indicated in Sect. 3.1. The difference in the accumulation mode aerosol number concentration is small between MAM3 and MAM7.

GMDD
4, 3485–3598, 2011

Figure 22 compares simulated vertical profiles of aerosol number concentration in the Aitken mode (diameter larger than 14 nm) and in the accumulation mode (diameter larger than 100 nm) with observations at Punta Arena, Chile (53° S) and Prestwick, Scotland (54° N) during the Interhemispheric Differences in Cirrus Properties From Anthropogenic Emissions (INCA) campaign (Minikin et al., 2003). Observed aerosol number concentrations in the Aitken mode in both locations show little variation up to 8–10 km. The Aitken mode number concentrations in Scotland are a factor of 2–3 higher than those in Chile. Aitken mode number concentrations from the model also show small vertical variations up to 10 km; however, they are similar between the two locations. The modeled concentrations are lower than those from measurements, especially at the NH site (Scotland). This underestimation may be partly due to the excessively large size of carbonaceous aerosols emitted from fossil fuel combustion and/or that the aerosol nucleation is too weak due to the too efficient scavenging of precursor gases (e.g., SO_2). Observed aerosol number concentrations in the accumulation mode decrease significantly with height in the boundary layer, and then vary little in the middle troposphere and increase slightly around 10 km for both locations. The model captures these vertical variations well and also the much higher concentrations at the NH (Scotland) than those at the SH (Chile). The model underestimates the observed accumulation mode number concentrations especially at the NH site (Scotland). There are slightly higher number concentrations from MAM7 than those from MAM3 for both Aitken and accumulation modes at both sites.

Figure 23 compares vertical profiles of modeled CCN number concentrations at supersaturation of 0.1 % with data from the eight field experiments reported in Ghan et al. (2001). Observations show a variety of vertical profiles of CCN number concentrations. CCN number concentrations increase over Tasmania in the austral winter and over the Arctic in spring, and vary little over Tasmania during ACE-1 in the austral summer. These vertical profiles suggest the influence of continual outflows from Australia or from mid-latitudes. At other sites observed CCN number concentrations decrease with altitude. The model results show the reduction for all sites. The model severely

GMDD
4, 3485–3598, 2011

underestimates the observed CCN number concentration in the Arctic in spring, which is consistent with the underestimation of BC concentration due to the too efficient wet scavenging in the model. The ARM site in Oklahoma is located in a strong concentration gradient region. With the large horizontal grid size, the model is not able to capture the small-scale spatial variability and thus underestimates the observed CCN number concentration. The model performance is qualitatively similar to that found by Wang et al. (2011) and Ghan et al. (2001). CCN number concentrations near the surface over ocean from MAM7 are significantly lower than those of MAM3, as discussed in Sect. 3.1.

4.3 Aerosol optical properties

Figure 24 compares the monthly aerosol optical depth (AOD) and single scattering albedo (SSA) at 550 nm from the model with observations from the AERONET (http://aeronet.gsfc.nasa.gov) at sites in seven regions (North and South America, Europe, East and South Asia, and Northern and Southern Africa) over the globe. The AERONET data are averaged for the years of 1998–2005. Modeled monthly AOD agrees with observations within a factor of 2 for sites in North America. The model also captures the seasonal variations of observed AOD in North America reasonably well: AOD is lower in the winter and higher in the summer due to the photochemical production of sulfate and SOA in the summer (figure not shown). At several sites the modeled AOD values are lower than observations in the summer probably due to the too strong wet scavenging in the model. Differences in simulated AOD between MAM3 and MAM7 are small in North America. The normalized mean bias (NMB) of simulated AOD in MAM3 and MAM7 is −0.28 there (Table 13). The underestimation of monthly AOD is much more severe in South and East Asia (by more than a factor of 2), probably due to the underestimation of anthropogenic emissions there. The model captures well the seasonal variations of AOD in North Africa (figure not shown), and MAM7 has a much better simulation (with NMB of −0.12) compared to the NMB of −0.37 of MAM3, due to its higher dust burdens and concentrations (Sect. 3). In South Africa, the

GMDD
4, 3485–3598, 2011

model is able to capture the AOD seasonal trends resulting from the biomass burning emission (figure not shown). However, both MAM3 and MAM7 underestimate the AOD peaks in autumn there.

The modeled SSA ranges mostly between 0.88–0.94, and has less variation than observations. This is indicated in the low correlation coefficients between model simulations and observations (Table 14). The model captures well the seasonal variations and magnitudes of SSA in Northern and Southern Africa. The modeled SSA is lower than observations in East Asia, probably because of the underestimation of anthropogenic sulfate there, while it is higher than observations in South America, probably because of the underestimation of local biomass burning sources in the model. Because of the combination of the AOD and SSA, modeled absorption AOD (AAOD) is mostly within a factor of 2 of observations in North America, Europe, East Asia (due to the compensation of lower AOD and lower SSA), and Northern Africa for MAM7 (figure not shown). The model underestimates observed AAOD in Northern Africa for MAM3 due to the underestimation of dust AOD, in Southern Africa (due to the underestimation of biomass burning AOD), in South Asia (due to the underestimation of anthropogenic AOD and overestimation of SSA), and in South America (due to the overestimation of SSA).

Figure 25 shows the simulated AOD at 550 nm from MAM3 and MAM7 in January and July, in comparison with that from a satellite AOD retrieval composite derived by Kinne et al. (2006). As noted in Kinne et al. (2006), this satellite composite combines the strength of individual satellite retrievals (MODIS, MISR, AVHRR, TOMS, and POLDER), giving regional preferences for different satellite products separately over land and over ocean. The simulated AOD captures the general patterns of AOD on the global scale. The model simulates higher AOD over the biomass burning region in Southern Africa and in the industrial region in East Asia in January, in agreement with satellite data. The model underestimates satellite observed AOD over North America, Europe and East Asia. However, this underestimation is not evident for North America compared to the AERONET data, which suggests the possible overestimation

GMDD
4, 3485–3598, 2011

of satellite AOD over North America in January (satellite observed AOD is over 0.1 for most of US). The model captures the observed AOD peaks over the Saharan and Asian deserts, biomass burning regions over Southern Africa and South America, and industrial regions over East and South Asia in July. The model underestimates observed AOD in East Asia, North America and Southern Africa in July, which agrees with the comparison of modeled AOD with the AERONET data. The model overestimates the outflow of Saharan dust and Southern African biomass aerosols over the Central Atlantic and Central Pacific, respectively. Modeled AOD from MAM3 and MAM7 is similar over the continents with higher AOD over Northern Africa in MAM7. Modeled AOD in MAM3 over oceans agrees reasonably well with satellite data, while modeled AOD in MAM7 is significantly lower over oceans (e.g., in the storm track regions), consistent with the lower sea salt concentrations in MAM7 as discussed in Sect. 3.

4.4 Cloud properties

In this subsection we compare model simulated cloud properties from MAM3 and MAM7 with available observations, which is important for the aerosol wet removal and aerosol indirect forcing. Figure 26 shows annual and zonal mean shortwave cloud forcing (SWCF), longwave cloud forcing (LWCF), liquid water path (LWP), and total cloud cover (CLDTOT) from MAM3 and MAM7 in comparison with available observations. The global annual mean values for these and other variables are given in Table 15. We can see that modeled SWCF is too strong in the tropics, but it is too weak in NH and SH high latitudes, in comparison with CERES data. Modeled LWCF is too low on the global scale compared with CERES data, as well as LWP with SSM/I data. Modeled total cloud cover is too low in the subtropics and mid-latitudes, but it is too high in the two polar regions, as compared to the ISCCP data. This too low LWP indicates too fast conversion of cloud water to precipitation and thus a too short lifetime of cloud water. This may partly explain the too large wet scavenging rates of aerosols (once they are inside the cloud water via droplet activation) and thus the too low burdens and short lifetimes of aerosols (e.g., POM, SOA and BC). The too large cloud cover in the high

GMDD
4, 3485–3598, 2011

latitudes of NH also contributes to the low concentrations of aerosol (e.g., BC) in the Arctic. Simulated cloud properties are very similar between MAM3 and MAM7 with a slightly higher column cloud droplet number concentration in MAM3 (Table 15), due to its larger sea salt concentrations. We note that the relative differences in CDNUMC are smaller than the differences in CCN at $S = 0.1\,\%$ (Table 15).

4.5 Timing

It takes about 4.8 h of wall-clock time for a one-year simulation with the stand-alone CAM5 with MAM3 (with 15 aerosol and 5 precursor gas species) using 128 CPUs on NCAR bluefire, an IBM Power 6. It takes 6.3 h for MAM7 (with 31 aerosol and 6 trace gas species), thus CAM5 with MAM7 is ∼ 30 % slower than CAM5 with MAM3. The wall-clock time for running MAM3 is ∼ 35 % higher than that using the CAM5 with the prognostic bulk aerosol module (BAM, with 13 aerosol and 3 precursor gas species). This increase in computational time is due to the additional aerosol microphysics processes (e.g., nucleation, condensation, coagulation) considered in MAM3.

5 Sensitivity studies

In the standard MAM7 the hygroscopicity (κ) value for POM is 0.1. As a result POM and BC in the primary carbon mode experience wet scavenging before aerosol particles in the primary carbon mode are aged into the accumulation mode. Therefore we do not find large differences in model simulated carbonaceous aerosols between MAM7 and MAM3. In one sensitivity experiment the κ value of POM is changed from 0.1 to 0.0 to reflect the non-hygroscopic nature ($\kappa = 0$) of POM from fossil fuel combustion. We run MAM7 to examine the impact of this change on model simulated carbonaceous aerosols (experiment MAM7-k). In another sensitivity experiment, in addition to $\kappa = 0$ for POM we change the coating criterion for conversion of carbonaceous aerosols in the primary carbon mode to accumulation mode. The coating thickness is changed

GMDD
4, 3485–3598, 2011

from 3 to 8 monolayers. Thus more coating material (sulfate, ammonium and SOA) is required to age primary carbon mode particles and transfer them to the accumulation mode (experiment MAM7-aging). For a 0.134 µm diameter non-hygroscopic particle, which is the volume-mean size for BC and POM emissions, the 3 and 8 monolayers of sulfate produce CCN with critical supersaturations of 0.49 and 0.32 %, respectively.

Tables 16 and 17 give the global budgets of POM and BC, respectively from the two sensitivity experiments (MAM7-k and MAM7-aging) in comparison with those from the MAM7 control run. Global POM and BC burdens in the primary carbon mode increase by ∼40 % in MAM7-k when scavenging through in-cloud droplet activation is suppressed by the lower value of κ. Their lifetimes are thus longer. With less wet removal in the primary mode, more POM and BC are transferred to the accumulation mode. Once in the accumulation mode they experience the same dry and wet removal efficiencies as those in MAM7. Thus burdens of POM and BC in the accumulation mode are higher but with similar lifetimes as MAM7. The global burdens of total POM and BC (i.e., primary carbon mode plus accumulation mode) in MAM7-k are 10 % and 8 % higher than those in MAM7, respectively.

With slower aging and less wet removal in the primary carbon mode (MAM7-aging), global burdens of POM and BC in the primary carbon mode increase by a factor of ∼4 with much longer lifetimes than those in MAM7. Similar amounts of POM and BC are transferred to the accumulation mode as in MAM7 as a result of less wet removal but more dry deposition (due to the slower aging) in the primary carbon mode. POM and BC burdens and lifetimes in accumulation mode are similar to those in MAM7. The global burdens of total POM and BC in MAM7-aging are 43 % and 34 % higher than those in MAM7, respectively.

A reduced κ value for POM and slower aging of primary carbon mode produce small changes for POM and BC surface concentrations near the continental source regions (e.g., at the IMPROVE and EMEP sites) in comparison with MAM7 (figures not shown). However, model underestimation of POM and BC surface concentration at ocean and remote continental sites are improved, especially for BC (Fig. 27). The impact on

GMDD
4, 3485–3598, 2011

vertical profiles of BC concentration from the two sensitivity experiments is shown in Figs. 15–17. With a reduced κ value for POM (MAM7-k run), BC concentrations are increased in comparison with MAM7 due to less efficient wet scavenging of BC in the primary carbon mode. However, the increase are small in the tropics and subtropics in North America (Fig. 15). There are significant increases in the BC concentrations in the upper troposphere in the mid-latitudes (during the CARB campaign in June). BC concentrations are enhanced by several times during the Arctic spring when the base-run concentrations are very low, but less so in the summer when base-run concentrations are higher (Fig. 16). These changes are consistent with the HIPPO comparison (Fig. 17), where strong increases occur in the mid- and high latitudes of NH, and in the high latitudes of SH. These increases in BC concentrations improve model comparison with observations except in the tropics and subtropics where the model high biases in the upper troposphere are larger.

With slower aging of primary carbon mode and $\kappa = 0$ for POM (MAM7-aging run), increases in BC concentrations are evident in all the profiles of Figs. 15–17. This makes the overestimations of BC concentrations in the free troposphere in the tropics and subtropics even more severe. The model still underestimates observed BC median concentrations in the Arctic in spring, which suggests a model bias of wet scavenging for the accumulation mode aerosol and/or underestimated local emissions in the model during the spring season. The impacts of the changes from these two sensitivity experiments are small for aerosol number and size distributions over the oceans and CCN number concentrations in Figs. 20–22.

Figure 28 shows the fraction of the total BC column burden that is in the primary carbon mode from the three experiments MAM7, MAM7-k and MAM7-aging. In the MAM7 control run, BC from primary emissions (e.g., fossil fuel, bio-fuel, and biomass burning) is aged to the accumulation mode quickly, e.g., in the industrial regions where sulfate concentrations are high. Primary BC fractions are 30–50 % in the tropical and boreal biomass burning source regions (e.g., Central Africa, the maritime continent, and Siberia). Other than these regions aged BC dominates the total BC burden (larger

GMDD
4, 3485–3598, 2011

than 90 %). With reduced κ value for POM (MAM7-k), primary BC fractions increase because of less wet removal. Primary BC fractions are 30–40 % over the Arctic regions because of more transport of primary BC from the source regions (e.g., Siberia). These results are in general agreement with observations that carbonaceous aerosol particles are internally mixed with sulfate and other components except near the source regions (e.g., Posfai et al., 2003; Clarke et al., 2004; Moffet and Prather, 2009; Wang et al., 2010). When the high coating criterion is used for aging, primary BC fraction increases significantly with values of 50–70 % over the Arctic and biomass burning regions in the maritime continent and Central Africa. There are high fractions (30–40 %) of primary BC in the SH midlatitudes due to the transport of primary BC from biomass burning regions in SH. However, BC concentrations there are small.

6 Conclusions and future work

In this study a modal aerosol module (MAM) was developed in CAM5 with two versions. The more comprehensive one (MAM7) has 7 log-normal modes and explicitly treats the aging of POM and BC from the primary carbon mode into which they are emitted to the accumulation mode where they are mixed with other aerosol species. For long-term (decades to centuries) simulations, a simplified version (MAM3) was developed that has 3 log-normal modes and neglects the aging process of POM and BC by assuming the immediate mixing of POM and BC with other aerosol species. Other approximations in MAM3 include merging of the MAM7 fine dust and fine sea salt modes into the accumulation mode in MAM3, and merging of the MAM7 coarse dust and coarse sea salt modes into the single coarse mode in MAM3, which is made feasible by the separate geographical sources of sea salt and mineral dust.

Sulfate and SOA burdens and concentrations are remarkably similar between MAM3 and MAM7 because most ($\sim$ 90 %) of these aerosol species are in the accumulation mode. Although POM and BC are treated differently in MAM3 and MAM7, POM and BC concentrations are also similar. This is because a value of $\kappa = 0.1$ is assumed

GMDD
4, 3485–3598, 2011

for POM, therefore much of the POM and BC in the primary carbon mode is wet-scavenged before aging into the accumulation mode in MAM7. Sensitivity tests with MAM7 with a lower κ value (0.0) for POM and additionally with a higher coating criteria for aging produce significantly larger POM and BC concentrations, especially at high latitudes.

Sea salt concentrations simulated by MAM7 are significantly lower (by 30–40 %) along with a lower AOD over the Southern Oceans than those from MAM3. This is primarily due to differences in the treatment of coarse-mode sea salt. MAM7 has different standard deviations (σ_g) for the coarse sea salt (2.0) and dust modes (1.8), while in MAM3 the value of 1.8 is used for the single coarse mode. Thus, the coarse-mode sea salt in MAM7 has larger sedimentation velocities than that in MAM3. Also, the fine sea salt mode in MAM7 with a σ_g of 2.0 is merged to the accumulation mode in MAM3 with a σ_g of 1.8. As a result, simulated CCN number concentration (at $S = 0.1$ %) and AOD from MAM7 over the oceans are lower than those from MAM3. Dust concentrations from MAM3 are slightly lower (by ~ 10 %) than those from MAM7 due to the different size ranges for fine and coarse dust, and to a lesser extent to the different assumptions of mixing states of dust with other components. Results from additional sensitivity tests are needed to more precisely explain how differing assumptions in MAM3 and MAM7 affect fine and coarse sea salt and dust concentrations, CCN, and AOD.

Another difference between MAM3 and MAM7 is that ammonia/ammonium cycles are explicitly treated in MAM7, but not in MAM3. NH_3 (g) dissolves to the cloud water and increases aqueous phase sulfate production by enhancing pH values of cloud water. The NH_4/SO_4 molar ratio in aerosol predicted in MAM7 averages 1.2 globally. It is near 2 in much of the continental and tropical marine boundary layer, while it is less than 1.0 in many mid-latitude marine boundary layer regions. The ratio is generally less than 1.0 in the free troposphere, except in the tropics where the ratio can be 1.5–2.0. These results differ from the ratio of 1.0 assumed in MAM3.

Overall the model with MAM3 and MAM7 performs reasonably well in capturing the spatial and temporal variations of observed mass concentrations of aerosol species,

GMDD
4, 3485–3598, 2011

aerosol number and size distribution, AOD, SSA, and CCN number concentration. There are biases in modeled aerosol fields that need to be improved in future work. Some of these biases are related to the model treatment of aerosol processes and properties, and some related to the model treatment of cloud and other physical processes. The simulated aerosol distributions and life cycles are tightly coupled with and affected by modeled cloud fields (e.g., cloud water content, cloud cover, precipitation) in GCMs. This is expected since wet removal is the primary removal process for submicron aerosol particles, and most sulfate is formed by cloud chemistry. CAM5 has a too rapid life cycle of cloud water, because of its low bias in cloud liquid water path as indicated in Sect. 4.4, in order to keep the same amount of surface precipitation through the conversion of cloud liquid water to rain water. This results in too fast wet-removal rates of aerosols. As a result, simulated sulfate and mineral dust concentrations at the surface are lower than those observed from the oceanic sites operated by the RSMAS at the University of Miami. Simulated accumulation mode number concentrations are lower than those observed in the marine boundary layer by Heintzenberg et al. (2000). There is a low bias in AOD on the global scale. In addition to cloud liquid water content, the high bias in low-level cloud amount at high latitudes in cold seasons increases the occurrence of wet removal of aerosol during its transport from the mid-latitudes to the polar regions (H. Wang, personal communication). This is indicated from the significantly low BC concentrations in the Arctic compared to observations from the ARCTAS and ARCPAC campaigns in April and from the HIPPO campaign in January. BC concentrations in the free troposphere in the tropics and in the mid-latitudes are, however, overestimated in the model, which suggests the need for improvement of transport and wet scavenging in convective clouds in the model. Currently CAM5 has very simple cloud microphysics for convective clouds, and no explicit treatment of aerosol activation in convective clouds, as well as separate (although weakly coupled) treatments of convective transport and scavenging. A more integrated treatment of the aerosol transport and scavenging by convective clouds is being developed, and the implementation of a double-moment cloud microphysics parameterization for deep convective clouds

GMDD
4, 3485–3598, 2011

in CAM5 (Song and Zhang, 2011) will allow further improvement of aerosol processes in convective clouds.

Another uncertain process is aerosol emissions: our results indicate the underestimation of anthropogenic emissions in the developing counties (e.g., in East and South Asia), and emissions of large forest fires (e.g., in Southern Africa and South America) and local fires (e.g., in the Arctic), which results in the low bias of AOD from comparison with the AERONET and satellite data. Currently MAM does not differentiate the properties of carbonaceous aerosol (POM and BC) between biomass burning and fossil fuel combustion sources, and it uses the same emitted size (0.134 μm diameter) for these two, although sizes of fossil fuel emitted particles can be much smaller (Dentener et al., 2006). This may partially explain the too low Aitken mode number concentrations over Scotland compared with the INCA observations. Future improvement of MAM will separate POM and BC by sources with different physical and chemical properties. In addition to emissions, aerosol nucleation and growth play key roles in the aerosol number and size distribution. The model underestimation of Aitken mode number concentration in the marine boundary layer suggests needed improvement of boundary layer aerosol nucleation and the role of organics and amines from biological sources in the nucleation and growth.

Surface OM is overestimated in the model compared to the data obtained at the North America IMPROVE network sites (especially in the Eastern US), while model simulated OM agrees with observations from Zhang et al. (2007) in most global sites within a factor of 2 and also with EMEP observations. The Eastern US high bias may reflect a different mixture of SOA precursors (from anthropogenic and biogenic sources). The agreement is better when lower SOA yields are used. Future improvement of SOA formation, partitioning and aging is needed.

Nitrate, which is not treated in MAM because of its computational expense, can be important on regional scales (e.g., in East Asia) (Gao et al., 2011) and is expected to be more important in simulations of the future with the expected increase of nitrogen-related and reduction of sulfur-related emissions. This can be realized through the

GMDD
4, 3485–3598, 2011

MOSAIC (Model for Simulating Aerosol Interactions and Chemistry) (Zaveri et al., 2008) aerosol thermodynamics model, which is being implemented in CAM5. MOSAIC can also treat the water uptake of aerosol particles more accurately and include aerosol-phase chemistry during the aging process (e.g., the heterogeneous chemistry on the surface of dust particles).

Along with the above planned improvements for MAM, future work will quantify model sensitivity to approximations on aerosol modal parameters (size range and geometric standard deviation), aerosol mixing state, internal structure and shape, aerosol production, transformation, and loss processes, and climate forcing mechanisms.

Acknowledgements. X. Liu, R. C. Easter, S. J. Ghan were funded by the US Department of Energy, Office of Science, Scientific Discovery through Advanced Computing (SciDAC) program. We thank M. Wang for providing the scripts for plotting some figures in this paper and J. P. Schwarz for providing the HIPPO BC data. A. Ekman would like to acknowledge the support form the Bert Bolin Center for Climate Research. M. J. Iacono was supported by the Office of Biological and Environmental Research of the US Department of Energy under Grant No. DE-FG02-92ER61549. The CESM project is supported by the National Science Foundation and the Office of Science (BER) of the US Department of Energy Computing resources were provided by the Climate Simulation Laboratory at NCAR's Computational and Information Systems Laboratory (CISL), sponsored by the National Science Foundation and other agencies. The Pacific Northwest National Laboratory is operated for DOE by Battelle Memorial Institute under contract DE-AC06-76RLO 1830.

References

Abdul-Razzak, H. and Ghan, S. J.: A parameterization of aerosol activation 2. Multiple aerosol types, J. Geophys. Res.-Atmos., 105(D5), 6837–6844, 2000.

Adachi, K. and Buseck, P. R.: Internally mixed soot, sulfates, and organic matter in aerosol particles from Mexico City, Atmos. Chem. Phys., 8, 6469–6481, doi:10.5194/acp-8-6469-2008, 2008.

Adachi, K., Chung, S., and Buseck, P.: Shapes of soot aerosol particles and implications for global climate, J. Geophys. Res.-Atmos., 115, D15206, DOI:10.1029/2009JD012868, 2010.

GMDD

4, 3485–3598, 2011

Adams, P. J. and Seinfeld, J. H.: Predicting global aerosol size distributions in general circulation models, J. Geophys. Res., 107, 4370, DOI 10.1029/2001JD001010, 2002.
Arimoto, R., Duce, R. A., Savoie, D. L., Prospero, J. M., Talbot, R., Cullen, J. D., Tomza, U., Lewis, N. F., and Jay, B. J.: Relationships among aerosol constituents from Asia and the North Pacific during PEM-West A, J. Geophys. Res., 101, 2011–2023, 1996.
Barth, M. C., Rasch, P. J., Kiehl, J. T., Benkovitz, C. M., and Schwartz, S. E.: Sulfur chemistry in the National Center for Atmospheric Research Community Climate Model: description, evaluation, features, and sensitivity to aqueous chemistry, J. Geophys. Res.-Atmos., 105(D1), 1387–1415, 2000.
Bauer, S. E., Wright, D. L., Koch, D., Lewis, E. R., McGraw, R., Chang, L.-S., Schwartz, S. E., and Ruedy, R.: MATRIX (Multiconfiguration Aerosol TRacker of mIXing state): an aerosol microphysical module for global atmospheric models, Atmos. Chem. Phys., 8, 6003–6035, doi:10.5194/acp-8-6003-2008, 2008.
Binkowski, F. S. and Shankar, U.: The regional particulate matter model. 1. Model description and preliminary results, J. Geophys. Res.-Atmos., 100, 26191–26209, 1995.
Bond, T. C. and Bergstrom, R. W.: Light absorption by carbonaceous particles: an investigative review, Aerosol Sci. Technol., 40, 27–67, 2006.
Bond, T. C., Habib, G., and Bergstrom, R. W.: Limitations in the enhancement of visible light absorption due to mixing state, J. Geophys. Res.-Atmos., 111(D20), D20211, doi:10.1029/2006jd007315, 2006.
Bond, T. C., Bhardwaj, E., Dong, R., Jogani, R., Jung, S. K., Roden, C., Streets, D. G., and Trautmann, N. M.: Historical emissions of black and organic carbon aerosol from energy-related combustion, 1850–2000, Global Biogeochem. Cy., 21(2), Gb2018, doi:10.1029/2006gb002840, 2007.
Bretherton, C. S. and Park, S.: A new moist turbulence parameterization in the community atmosphere model, J. Climate, 22(12), 3422–3448, doi:10.1175/2008jcli2556.1, 2009.
Briegleb, B. P. and Light, B.: A Delta-Eddington multiple scattering parameterization for solar radiation in the sea-ice component of the Community Climate System Model, National Center for Atmospheric Research Technical Note NCAR/TN-472+STR, 2007.
Clarke, A. D., Shinozuka, Y., Kapustin, V. N., Howell, S., Huebert, B., Doherty, S., Anderson, T., Covert, D., Anderson, J., Hua, X., Moore, K. G., McNaughton, C., Carmichael, G., and Weber, R.: Size distributions and mixtures of dust and black carbon aerosol in Asian outflow: physiochemistry and optical properties, J. Geophys. Res., 109, D15S09,

GMDD
4, 3485–3598, 2011

doi:10.1029/2003JD004378, 2004.
Clarke, A., McNaughton, C., Kapustin, V., Shinozuka, Y., Howell, S., Dibb, J., Zhou, J., Anderson, B., Brekhovskikh, V., Turner, H., and Pinkerton, M.: "Biomass burning and pollution aerosol over North America: Organic components and their influence on spectral optical properties and humidification response", J. Geophys. Res., 112, D12S18, doi:10.1029/2006jd007777, 2007.
Clough, S. A., Shephard, M. W., Mlawer, E., Delamere, J. S., Iacono, M., Cady-Pereira, K., Boukabara, S., and Brown, P. D.: Atmospheric radiative transfer modeling: a summary of the AER codes, J. Quant. Spectrosc. Ra., 91(2), 233–244 doi:10.1016/J.Jqsrt.2004.05.058, 2005.
Collins, W. D., Rasch, P. J., Boville, B. A., Hack, J. J., McCaa, J. R., Williamson, D. L., Kiehl, J. T., Briegleb, B., Bitz, C., Lin, S.-J., Zhang, M.-H., and Dai, Y.: Description of the NCAR Community Atmosphere Model (CAM 3.0), National Center for Atmospheric Research Technical Note NCAR/TN–464+STR, 2004.
Cooke, W. F. and Wilson, J. J. N.: A global black carbon aerosol model, J. Geophys. Res.-Atmos., 101(D14), 19395–19409, 1996.
Cooke, W. F., Liousse, C., Cachier, H., and Feichter, J.: Construction of a 1 degrees × 1 degrees fossil fuel emission data set for carbonaceous aerosol and implementation and radiative impact in the ECHAM4 model, J. Geophys. Res., 104, 22137–22162, 1999.
Dentener, F., Kinne, S., Bond, T., Boucher, O., Cofala, J., Generoso, S., Ginoux, P., Gong, S., Hoelzemann, J. J., Ito, A., Marelli, L., Penner, J. E., Putaud, J.-P., Textor, C., Schulz, M., van der Werf, G. R., and Wilson, J.: Emissions of primary aerosol and precursor gases in the years 2000 and 1750 prescribed data-sets for AeroCom, Atmos. Chem. Phys., 6, 4321–4344, doi:10.5194/acp-6-4321-2006, 2006.
Easter, R. C., Ghan, S. J., Zhang, Y., Saylor, R. D., Chapman, E. G., Laulainen, N. S., Abdul-Razzak, H., Leung, L. R., Bian, X., and Zaveri, R. A.: MIRAGE: Model description and evaluation of aerosols and trace gases, J. Geophys. Res.-Atmos., 109(D20), doi:D20210,10.1029/2004jd004571, 2004.
Emmons, L. K., Walters, S., Hess, P. G., Lamarque, J.-F., Pfister, G. G., Fillmore, D., Granier, C., Guenther, A., Kinnison, D., Laepple, T., Orlando, J., Tie, X., Tyndall, G., Wiedinmyer, C., Baughcum, S. L., and Kloster, S.: Description and evaluation of the Model for Ozone and Related chemical Tracers, version 4 (MOZART-4), Geosci. Model Dev., 3, 43–67, doi:10.5194/gmd-3-43-2010, 2010.

GMDD
4, 3485–3598, 2011

Farina, S. C., Adams, P. J., and Pandis, S. N.: Modeling global secondary organic aerosol formation and processing with the volatility basis set: implications for anthropogenic secondary organic aerosol, J. Geophys. Res., 115, D09202, doi:10129/2009JD013046, 2010.

Feng, Y. and Penner, J. E.: Global modeling of nitrate and ammonium: interaction of aerosols and tropospheric chemistry, J. Geophys. Res., 112, D01304, doi:10.1029/2005JD006404, 2007.

Ferraro, R. R., Weng, F. Z., Grody, N. C., and Basist, A.: An eightyear (1987–1994) time series of rainfall, clouds, water vapor, snow cover, and sea ice derived from SSM/I measurements, B. Am. Meteorol. Soc., 77, 891–905, 1996.

Flanner, M. G., Zender, C. S., Randerson, J. T., and Rasch, P. J.: Present-day climate forcing and response from black carbon in snow, J. Geophys. Res.-Atmos., 112(D11), doi:10.1029/2006jd008003, 2007.

Forster, P., Ramaswamy, V., Artaxo, P., Berntsen, T., Betts, R., Fahey, D. W., Haywood, J., Lean, J., Lowe, D. C., Myhre, G., Nganga, J., Prinn, R., Raga, G., Schulz, M., and Van Dorland, R., 2007: Changes in atmospheric constituents and in radiative forcing, in: Climate Change 2007: The Physical Science Basis, Contribution of Working Group I to the Fourth Assessment Report of the Intergovernmental Panel on Climate Change, edited by: Solomon, S., Qin, D., Manning, M., Chen, Z., Marquis, M., Averyt, K. B., Tignor, M., and Miller, H. L., Cambridge University Press, New York, 2007.

Gao, Y., Liu, X., Zhao, C., Zhang, M., and Wang, Y.: Emission controls versus meteorological conditions in determining aerosol concentrations in Beijing during the 2008 Olympic Games, Atmos. Chem. Phys. Discuss., 11, 16655–16691, doi:10.5194/acpd-11-16655-2011, 2011.

Gent, P. R., Yeager, S. G., Neale, R. B., Levis, S., and Bailey, D. A.: Improvements in a half degree atmosphere/land version of the CCSM, Clim. Dynam., 79, 25–58, doi:10.1007/s00382-009-0614-8, 2009.

Gettelman, A., Morrison, H., and Ghan, S. J.: A new two-moment bulk stratiform cloud microphysics scheme in the community atmosphere model, version 3 (CAM3). Part II: Single-colunm and global results, J. Climate, 21(15), 3660–3679, doi:10.1175/2008jcli2116.1, 2008.

Gettelman, A., Liu, X., Ghan, S. J., Morrison, H., Park, S., Conley, A. J., Klein, S. A., Boyle, J., Mitchell, D. L., and Li, J. L. F.: Global simulations of ice nucleation and ice supersaturation with an improved cloud scheme in the Community Atmosphere Model, J. Geophys. Res., 115, D18216, doi:10.1029/2009JD013797, 2010.

GMDD

4, 3485–3598, 2011

Ghan, S. J. and Easter, R. C.: Impact of cloud-borne aerosol representation on aerosol direct and indirect effects, Atmos. Chem. Phys., 6, 4163–4174, doi:10.5194/acp-6-4163-2006, 2006.

Ghan, S. J. and Schwartz, S. E.: Aerosol properties and processes – a path from field and laboratory measurements to global climate models, B. Am. Meteorol. Soc., 88(7), 1059–1083 , doi:10.1175/Bams-88-7-1059, 2007.

Ghan, S. J. and Zaveri, R. A.: Parameterization of optical properties for hydrated internally mixed aerosol, J. Geophys. Res.-Atmos., 112(D10), doi:D10201,10.1029/2006jd007927, 2007.

Ghan, S. J., Leung, L. R., Easter, R. C., and AbdulRazzak, K.: Prediction of cloud droplet number in a general circulation model, J. Geophys. Res.-Atmos., 102(D18), 21777–21794, 1997.

Ghan, S. J., Easter, R. C., Chapman, E. G., Abdul-Razzak, H., Zhang, Y., Leung, L. R., Laulainen, N. S., Saylor, R. D., and Zaveri, R. A.: A physically based estimate of radiative forcing by anthropogenic sulfate aerosol, J. Geophys. Res.-Atmos., 106(D6), 5279–5293, 2001.

Ghan, S. J., Liu, X., Easter, R. C., Zaveri, R., Rash, P. J., and Yoon, J.-H.: Toward a minimal representation of aerosol direct and indirect effects: comparative decomposition, J. Climate, submitted, 2011.

Greenwald, T. J., Stephens, G. L., Vonderhaar, T. H., and Jackson, D. L.: A physical retrieval of cloud liquid water over the global oceans using special sensor microwave imager (SSM/I) observations, J. Geophys. Res., 98, 18471–18488, 1993.

Han, Q. Y., Rossow, W. B., and Lacis, A. A.: Near-Global survey of effective droplet radii in liquid water clouds using ISCCP data, J. Climate, 7, 465–497, 1994.

Heintzenberg, J., Covert, D. C., and Van Dingenen, R.: Size distribution and chemical composition of marine aerosols: a compilation and review, Tellus B, 52, 1104–1122, 2000.

Herzog, M., Weisenstein, D. K., and Penner, J. E.: A dynamic aerosol module for global chemical transport models: Model description, J. Geophys. Res.-Atmos., 109(D18), D18202, doi:10.1029/2003jd004405, 2004.

Hess, M., Koepke, P., and Schult, I.: Optical properties of aerosols and clouds: the software package OPAC, B. Am. Meteorol. Soc., 79(5), 831–844, 1998.

Hoose, C., Lohmann, U., Erdin, R., and Tegen, I.: The global influence of dust mineralogical composition on heterogeneous ice nucleation in mixed-phase clouds, Environ. Res. Lett.,

GMDD

4, 3485–3598, 2011

3(2), 025003, doi:10.1088/1748-9326/3/2/025003, 2008.
Horowitz, L. W., Walters, S., Mauzerall, D. L., Emmons, L. K., Rasch, P. R., Granier, C., Tie, X., Lamarque, J.-F., Schultz, M. G., Tyndall, G. S., Orlando, J. J., and Brasseur, G. P.: A global simulation of tropospheric ozone and related tracers: description and evaluation of MOZART, version 2, J. Geophys. Res.-Atmos., 108, 4784, doi:10.1029/2002JD002853, 2003.
Howell, S. G., Clarke, A. D., Shinozuka, Y., Kapustin, V., McNaughton, C. S., Huebert, B. J., Doherty, S. J., and Anderson, T. L.: Influence of relative humidity upon pollution and dust during ACE-Asia: size distributions and implications for optical properties, J. Geophys. Res., 111, D06205, doi:10.1029/2004jd005759, 2006.
Iacono, M. J., Delamere, J. S., Mlawer, E. J., and Clough, S. A.: Evaluation of upper tropospheric water vapor in the NCAR Community Climate Model (CCM3) using modeled and observed HIRS radiances, J. Geophys. Res.-Atmos., 108(D2), 4037, doi:10.1029/2002jd002539, 2003.
Iacono, M. J., Delamere, J. S., Mlawer, E. J., Shephard, M. W., Clough, S. A., and Collins, W. D.: Radiative forcing by long-lived greenhouse gases: calculations with the AER radiative transfer models, J. Geophys. Res.-Atmos., 113(D13), D13103, doi:10.1029/2008jd009944, 2008.
Jacobson, M. Z.: Strong radiative heating due to the mixing state of black carbon in atmospheric aerosols, Nature, 409(6821), 695–697, 2001.
Jacobson, M. Z.: Reply to comment by Feichter, J. et al. on "Control of fossil-fuel particulate black carbon and organic matter, possibly the most effective method of slowing global warming", J. Geophys. Res., 108(D24), 4768, doi:10.1029/2002JD003299, 2003.
Jensen, E. J., Lawson, P., Baker, B., Pilson, B., Mo, Q., Heymsfield, A. J., Bansemer, A., Bui, T. P., McGill, M., Hlavka, D., Heymsfield, G., Platnick, S., Arnold, G. T., and Tanelli, S.: On the importance of small ice crystals in tropical anvil cirrus, Atmos. Chem. Phys., 9, 5519–5537, doi:10.5194/acp-9-5519-2009, 2009.
Jimenez, J. L., Canagaratna, M. R., Donahue, N. M., Prevot, A. S., Zhang, Q., Kroll, J. H., DeCarlo, P. F., Allan, J. D., Coe, H., Ng, N. L., Aiken, A. C., Docherty, K. S., Ulbrich, I. M., Grieshop, A. P., Robinson, A. L., Duplissy, J., Smith, J. D., Wilson, K. R., Lanz, V. A., Hueglin, C., Sun, Y. L., Tian, J., Laaksonen, A., Raatikainen, T., Rautiainen, J., Vaattovaara, P., Ehn, M., Kulmala, M., Tomlinson, J. M., Collins, D. R., Cubison, M. J., Dunlea, E. J., Huffman, J. A., Onasch, T. B., Alfarra, M. R., Williams, P. I., Bower, K., Kondo, Y., Schneider, J., Drewnick, F., Borrmann, S., Weimer, S., Demerjian, K., Salcedo, D., Cottrell, L., Griffin, R., Takami, A., Miyoshi, T., Hatakeyama, S., Shimono, A., Sun, J. Y., Zhang, Y. M., Dzepina, K., Kimmel, J.

GMDD
4, 3485–3598, 2011

R., Sueper, D., Jayne, J. T., Herndon, S. C., Trimborn, A. M., Williams, L. R., Wood, E. C., Middlebrook, A. M., Kolb, C. E., Baltensperger, U., and Worsnop, D. R.: Evolution of organic aerosols in the atmosphere, Science, 326, 1525–1529, 2009.

Johnson, K. S., Zuberi, B., Molina, L. T., Molina, M. J., Iedema, M. J., Cowin, J. P., Gaspar, D. J., Wang, C., and Laskin, A.: Processing of soot in an urban environment: case study from the Mexico City Metropolitan Area, Atmos. Chem. Phys., 5, 3033–3043, doi:10.5194/acp-5-3033-2005, 2005.

Junker, C. and Liousse, C.: A global emission inventory of carbonaceous aerosol from historic records of fossil fuel and biofuel consumption for the period 1860–1997, Atmos. Chem. Phys., 8, 1195–1207, doi:10.5194/acp-8-1195-2008, 2008.

Kanakidou, M., Seinfeld, J. H., Pandis, S. N., Barnes, I., Dentener, F. J., Facchini, M. C., Van Dingenen, R., Ervens, B., Nenes, A., Nielsen, C. J., Swietlicki, E., Putaud, J. P., Balkanski, Y., Fuzzi, S., Horth, J., Moortgat, G. K., Winterhalter, R., Myhre, C. E. L., Tsigaridis, K., Vignati, E., Stephanou, E. G., and Wilson, J.: Organic aerosol and global climate modelling: a review, Atmos. Chem. Phys., 5, 1053–1123, doi:10.5194/acp-5-1053-2005, 2005.

Kerminen, V. M. and Kulmala, M.: Analytical formulae connecting the real and the apparent nucleation rate and the nuclei number concentration for atmospheric nucleation events, J. Aerosol Sci., 33(4), 609–622, doi:PiiS0021-8502(01)00194-X, 2002.

Kiehl, J. T. and Trenberth, K. E.: Earth's annual global mean energy budget, B. Am. Meteorol. Soc., 78, 197–208, 1997.

Kinne, S., Schulz, M., Textor, C., Guibert, S., Balkanski, Y., Bauer, S. E., Berntsen, T., Berglen, T. F., Boucher, O., Chin, M., Collins, W., Dentener, F., Diehl, T., Easter, R., Feichter, J., Fillmore, D., Ghan, S., Ginoux, P., Gong, S., Grini, A., Hendricks, J., Herzog, M., Horowitz, L., Isaksen, I., Iversen, T., Kirkevå, A., Kloster, S., Koch, D., Kristjansson, J. E., Krol, M., Lauer, A., Lamarque, J. F., Lesins, G., Liu, X., Lohmann, U., Montanaro, V., Myhre, G., Penner, J., Pitari, G., Reddy, S., Seland, O., Stier, P., Takemura, T., and Tie, X.: An AeroCom initial assessment – optical properties in aerosol component modules of global models, Atmos. Chem. Phys., 6, 1815–1834, doi:10.5194/acp-6-1815-2006, 2006.

Kirkevag, A., Iversen, T., Seland, O., Debernard, J. B., Storelvmo, T., and Kristjansson, J. E.: Aerosol-cloud-climate interactions in the climate model CAM-Oslo, Tellus A, 60(3), 492–512, doi:10.1111/J.1600-0870.2008.00313, 2008.

Koch, D., Schulz, M., Kinne, S., McNaughton, C., Spackman, J. R., Balkanski, Y., Bauer, S., Berntsen, T., Bond, T. C., Boucher, O., Chin, M., Clarke, A., De Luca, N., Dentener, F.,

GMDD
4, 3485–3598, 2011

Diehl, T., Dubovik, O., Easter, R., Fahey, D. W., Feichter, J., Fillmore, D., Freitag, S., Ghan, S., Ginoux, P., Gong, S., Horowitz, L., Iversen, T., Kirkevåg, A., Klimont, Z., Kondo, Y., Krol, M., Liu, X., Miller, R., Montanaro, V., Moteki, N., Myhre, G., Penner, J. E., Perlwitz, J., Pitari, G., Reddy, S., Sahu, L., Sakamoto, H., Schuster, G., Schwarz, J. P., Seland, Ø., Stier, P., Takegawa, N., Takemura, T., Textor, C., van Aardenne, J. A., and Zhao, Y.: Evaluation of black carbon estimations in global aerosol models, Atmos. Chem. Phys., 9, 9001–9026, doi:10.5194/acp-9-9001-2009, 2009.

Koehler, K. A., Kreidenweis, S. M., DeMott, P. J., Petters, M. D., Prenni, A. J., and Carrico, C. M.: Hygroscopicity and cloud droplet activation of mineral dust aerosol, Geophys. Res. Lett., 36, L08805, doi:10.1029/2009gl037348, 2009.

Koretsky, C., Sverjensky, D., Salisbury, J., and D'Aria, D.: Detection of surface hydroxyl species on quart, gamma-alumina and feldspars using diffuse reflectance infrared spectroscopy, Geochim. Cosmochim. Ac., 61, 2193–2210, 1997.

Kroll, J. H., Ng, N. L., Murphy, S. M., Flagan, R. C., and Seinfeld, J. H.: Secondary organic aerosol formation from isoprene photooxidation, Environ. Sci. Technol., 40(6), 1869–1877, doi:10.1021/Es0524301, 2006.

Kumar, P., Nenes, A., and Sokolik, I.: The importance of adsoption for CCN activity and hygroscopic properties of mineral dust aerosol, Geophys. Res. Lett., 36, L24804, doi:10.1029/2009GL040827, 2009.

Lamarque, J.-F., Bond, T. C., Eyring, V., Granier, C., Heil, A., Klimont, Z., Lee, D., Liousse, C., Mieville, A., Owen, B., Schultz, M. G., Shindell, D., Smith, S. J., Stehfest, E., Van Aardenne, J., Cooper, O. R., Kainuma, M., Mahowald, N., McConnell, J. R., Naik, V., Riahi, K., and van Vuuren, D. P.: Historical (1850–2000) gridded anthropogenic and biomass burning emissions of reactive gases and aerosols: methodology and application, Atmos. Chem. Phys., 10, 7017–7039, doi:10.5194/acp-10-7017-2010, 2010.

Lawson, R. P., Baker, B. A., Pilson, B., and Mo, Q.: In situ observations of the microphysical properties of wave, cirrus and anvil clouds. Part 2: Cirrus cloud, J. Atmos. Sci., 63, 3186–3203, 2006.

Loeb, N. G., Wielicki, B. A., Doelling, D. R., Smith, G. L., Keyes, D. F., Kato, S., Manalo-Smith, N., and Wong, T.: Toward optimal closure of the Earth's top-of-atmosphere radiation budget, J. Climate, 22, 748–766, doi:10.1175/2008jcli2637.1, 2009.

Lim, Y. B. and Ziemann, P. J.: Products and mechanism of secondary organic aerosol formation from reactions of *n*-alkanes with OH radicals in the presence of NO_x, Environ. Sci. Technol.,

GMDD
4, 3485–3598, 2011

39(23), 9229–9236, doi:10.1021/Es051447g, 2005.
Lin, S. J.: A "vertically Lagrangian" finite-volume dynamical core for global models, Mon. Weather Rev., 132(10), 2293–2307, 2004.
Lin, S. J. and Rood, R. B.: Multidimensional flux-form semi-Lagrangian transport schemes, Mon. Weather Rev., 124(9), 2046–2070, 1996.
Liousse, C., Penner, J. E., Chuang, C., Walton, J. J., Eddleman, H., and Cachier, H.: A global three-dimensional model study of carbonaceous aerosols, J. Geophys. Res., 101, 19411–19432, 1996.
Liu, X. H. and Penner, J. E.: Ice nucleation parameterization for global models, Meteorol. Z., 14(4), 499–514, doi:10.1127/0941-2948/2005/0059, 2005.
Liu, X., and Wang, J.: How important is organic aerosol hygroscopicity to aerosol indirect forcing?, Environ. Res. Lett., 5, 044010, doi:10.1088/1748-9326/5/4/044010, 2010.
Liu, X. H., Penner, J. E., and Herzog, M.: Global modeling of aerosol dynamics: model description, evaluation, and interactions between sulfate and nonsulfate aerosols, J. Geophys. Res.-Atmos., 110(D18), D18206, doi:10.1029/2004jd005674, 2005.
Liu, X. H., Penner, J. E., Ghan, S. J., and Wang, M.: Inclusion of ice microphysics in the NCAR community atmospheric model version 3 (CAM3), J. Climate, 20(18), 4526–4547, doi:10.1175/Jcli4264.1, 2007.
Liu, X. H., Penner, J. E., and Wang, M. H.: Influence of anthropogenic sulfate and black carbon on upper tropospheric clouds in the NCAR CAM3 model coupled to the IMPACT global aerosol model, J. Geophys. Res.-Atmos., 114, D03204, doi:10.1029/2008jd010492, 2009.
Lohmann, U. and Feichter, J.: Global indirect aerosol effects: a review, Atmos. Chem. Phys., 5, 715–737, doi:10.5194/acp-5-715-2005, 2005.
Mahowald, N., Muhs, D., Levis, S., Rasch, P., Yoshioka, M., and Zender, C.: Change in atmospheric mineral aerosols in response to climate: last glacial period, pre-industrial, modern and doubled-carbon dioxide climates, J. Geophys. Res., 111, D10202, doi:10210.11029/12005JD006653, 2006a.
Mahowald, N., Yoshioka, M., Collins, W., Conley, A., Fillmore, D., and Coleman, D.: Climate response and radiative forcing from mineral aerosols during the last glacial maximum, pre-industrial and doubled-carbon dioxide climates, Geophys. Res. Lett., 33, L20705, doi:10.1029/2006GL026126, 2006b.
Mahowald, N., Engelstaedter, S., Luo, C., Sealy, A., Artaxo, P., Benitez-Nelson, C., Bonnet, S., Chen, Y., Chuang, P. Y., Cohen, D. D., Dulac, F., Herut, B., Johansen, A. M., Kubilay, N.,

GMDD
4, 3485–3598, 2011

Losno, R., Maenhaut, W., Paytan, A., Prospero, J. M., Shank, L. M., and Siefert, R. L.: Atmospheric iron deposition: global distribution, variability and human perturbations, Annu. Rev. Marine Sci., 1, 245–278, doi:10.1146/annurev/marine.010908.163727, 2009.

Märtensson, E. M., Nilsson, E. D., de Leeuw, G., Cohen, L. H., and Hansson, H. C.: Laboratory simulations and parameterization of the primary marine aerosol production, J. Geophys. Res.-Atmos., 108(D9), 4297, doi:10.1029/2002jd002263, 2003.

McFarquhar, G. M., Um, J., Freer, M., Baumgardner, D., Kok, G. L., and Mace, G.: Importance of small ice crystals to cirrus properties: observations from the Tropical Warm Pool International Cloud Experiment (TWP-ICE), Geophys. Res. Lett., 34(13), L13803, doi:10.1029/2007gl029865, 2007.

McGraw, R.: Description of aerosol dynamics by the quadrature method of moments, Aerosol Sci. Technol., 27(2), 255–265, 1997.

McNaughton, C. S., Clarke, A. D., Kapustin, V., Shinozuka, Y., Howell, S. G., Anderson, B. E., Winstead, E., Dibb, J., Scheuer, E., Cohen, R. C., Wooldridge, P., Perring, A., Huey, L. G., Kim, S., Jimenez, J. L., Dunlea, E. J., DeCarlo, P. F., Wennberg, P. O., Crounse, J. D., Weinheimer, A. J., and Flocke, F.: Observations of heterogeneous reactions between Asian pollution and mineral dust over the Eastern North Pacific during INTEX-B, Atmos. Chem. Phys., 9, 8283–8308, doi:10.5194/acp-9-8283-2009, 2009.

Menon, S., Del, A. D., Genio, Koch, D., and Tselioudis, G.: GCM simulations of the aerosol indirect effect: sensitivity to cloud parameterization and aerosol burden, J. Atmos. Sci., 59(3), 692–713, 2002.

Merikanto, J., Napari, I., Vehkamaki, H., Anttila, T., and Kulmala, M.: New parameterization of sulfuric acid-ammonia-water ternary nucleation rates at tropospheric conditions, J. Geophys. Res.-Atmos., 112(D15), D15207, doi:10.1029/2006jd007977, 2007.

Meyers, M. P., Demott, P. J., and Cotton, W. R.: New primary ice-nucleation parameterizations in an explicit cloud model, J. Appl. Meteorol., 31(7), 708–721, 1992.

Minikin, A., Petzold, A., Strom, J., Krejci, R., Seifert, M., van Velthoven, P., Schlager, H., and Schumann, U.: Aircraft observations of the upper tropospheric fine particle aerosol in the Northern and Southern Hemispheres at midlatitudes, Geophys. Res. Lett., 30, 1503, doi:10.1029/2002gl016458, 2003.

Mitchell, D. L.: Parameterization of the Mie extinction and absorption coefficients for water clouds, J. Atmos. Sci., 57(9), 1311–1326, 2000.

Mitchell, D. L.: Effective diameter in radiation transfer: general definition, applications, and

GMDD
4, 3485–3598, 2011

limitations, J. Atmos. Sci., 59(15), 2330–2346, 2002.
Mitchell, D. L., Baran, A. J., Arnott, W. P., and Schmitt, C.: Testing and comparing the modified anomalous diffraction approximation, J. Atmos. Sci., 63(11), 2948–2962, 2006.
Mlawer, E. J., Taubman, S. J., Brown, P. D., Iacono, M. J., and Clough, S. A.: Radiative transfer for inhomogeneous atmospheres: RRTM, a validated correlated-k model for the longwave, J. Geophys. Res.-Atmos., 102(D14), 16663–16682, 1997.
Moffet, R. C. and Prather, K. A.: In-situ measurements of the mixing state and optical properties of soot with implications for radiative forcing estimates, P. Natl. Acad. Sci. USA, 106(29), 11872–11877, doi:10.1073/Pnas.0900040106, 2009.
Monahan, E., Spiel, D. E., and Davidson, K. L.: A model of marine aerosol generation via whitecaps and wave disruption, in: Oceanic Whitecaps, edited by: Monahan, E. C. and MacNiochaill, G., D. Reidel, Norwell, Mass., 167–193, 1986.
Morrison, H. and Gettelman, A.: A new two-moment bulk stratiform cloud microphysics scheme in the community atmosphere model, version 3 (CAM3). Part I: Description and numerical tests, J. Climate, 21(15), 3642–3659, doi:10.1175/2008jcli2105.1, 2008.
Moteki, N. and Kondo, Y.: Effects of mixing state on black carbon measurements by laser-induced incandescence, Aerosol Sci. Tech., 41, 398–417, doi:10.1080/02786820701199728, 2007.
Moteki, N., Kondo, Y., Miyazaki, Y., Takegawa, N., Komazaki, Y., Kurata, G., Shirai, T., Blake, D. R., Miyakawa, T., and Koike, M.: Evolution of mixing state of black carbon particles: aircraft measurements over the Western Pacific in March 2004, Geophys. Res. Lett., 34, L11803, doi:10.1029/2006gl028943, 2007.
Neale, R. B., Richter, J. H., and Jochum, M.: The Impact of convection on ENSO: from a delayed oscillator to a series of events, J. Climate, 21(22), 5904–5924, doi:10.1175/2008jcli2244.1, 2008.
Ng, N. L., Chhabra, P. S., Chan, A. W. H., Surratt, J. D., Kroll, J. H., Kwan, A. J., McCabe, D. C., Wennberg, P. O., Sorooshian, A., Murphy, S. M., Dalleska, N. F., Flagan, R. C., and Seinfeld, J. H.: Effect of NO_x level on secondary organic aerosol (SOA) formation from the photooxidation of terpenes, Atmos. Chem. Phys., 7, 5159–5174, doi:10.5194/acp-7-5159-2007, 2007.
Odum, J. R., Jungkamp, T. P. W., Griffin, R. J., Forstner, H. J. L., Flagan, R. C., and Seinfeld, J. H.: Aromatics, reformulated gasoline, and atmospheric organic aerosol formation, Environ. Sci. Technol., 31(7), 1890–1897, 1997.

GMDD
4, 3485–3598, 2011

Okin, G.: A new model of wind erosion in the presence of vegetation, J. Geophys. Res.-Earth, 113, F02S10, doi:10.1029/2007JF000758, 2008.

Oleson, K. W., Lawrence, D. M., Bonan, G. B., Flanner, M. G., Kluzek, E., Lawrence, P. J., Levis, S., Swenson, S. C., Thornton, P. E., Dai, A., Decker, M., Dickinson, R., Feddema, J., Heald, C. L., Hoffman, F., Lamarque, J.-F., Mahowald, N., Niu, G.-Y., Qian, T., Randerson, J., Running, S., Sakaguchi, K., Slater, A., Stockli, R., Wang, A., Yang, Z.-L., Zeng, Xi., and Zeng, Xu.: Technical Description of version 4.0 of the Community Land Model (CLM), NCAR Technical Note NCAR/TN-478+STR, National Center for Atmospheric Research, Boulder, CO, 257 pp., 2010.

Ovtchinnikov, M. and Ghan, S. J.: Parallel simulations of aerosol influence on clouds using cloud-resolving and single-column models, J. Geophys. Res.-Atmos., 110(D15), doi:10.1029/2004jd005088, 2005.

Park, S. and Bretherton, C. S.: The University of Washington shallow convection and moist turbulence schemes and their impact on climate simulations with the Community Atmosphere Model, J. Climate, 22(12), 3449–3469, doi:10.1175/2008jcli2557.1, 2009.

Park, S., Bretherton, C., and Rasch, P. J.: The global cloud simulations in the community atmosphere model CAM5, in preparation, 2011.

Petters, M. D. and Kreidenweis, S. M.: A single parameter representation of hygroscopic growth and cloud condensation nucleus activity, Atmos. Chem. Phys., 7, 1961–1971, doi:10.5194/acp-7-1961-2007, 2007.

Pierce, J. R. and Adams, P. J.: Global evaluation of CCN formation by direct emission of sea salt and growth of ultrafine sea salt, J. Geophys. Res., 111, D06203, doi:10.1029/2005JD006186, 2006.

Pincus, R., Barker, H. W., and Morcrette, J. J.: A fast, flexible, approximate technique for computing radiative transfer in inhomogeneous cloud fields, J. Geophys. Res.-Atmos., 108(D13), 4376, doi:10.1029/2002jd003322, 2003.

Platnick, S., King, M. D., Ackerman, S. A., Menzel, W. P., Baum, B. A., Riedi, J. C., and Frey, R. A.: The MODIS cloud products: algorithms and examples from Terra, IEEE T. Geosci. Remote, 41, 459–473, 2003.

Poschl, U., Canagaratna, M., Jayne, J. T., Molina, L. T., Worsnop, D. R., Kolb, C. E., and Molina, M. J.: Mass accommodation coefficient of H_2SO_4 vapor on aqueous sulfuric acid surfaces and gaseous diffusion coefficient of H_2SO_4 in N_2/H_2O, J. Phys. Chem. A, 102(49), 10082–10089, 1998.

GMDD

4, 3485–3598, 2011

Posfai, M., Simonics, R., Li, J., Hobbs, P. V., and Buseck, P. R.: Individual aerosol particles from biomass burning in Southern Africa: 1. Compositions and size distributions of carbonaceous particles, J. Geophys. Res., 108, 8483–8496, 2003.

Prospero, J. M., Uematsu, M., and Savoie, D. L.: Mineral aerosol transport to the Pacific Ocean, in: Chemical Oceanography, edited by: Ridley, J. P., Chester, R., and Duce, R. A., Elsevier, New York, 188–218, 1989.

Rasch, P. J. and Kristjansson, J. E.: A comparison of the CCM3 model climate using diagnosed and predicted condensate parameterizations, J. Climate, 11(7), 1587–1614, 1998.

Rasch, P. J., Barth, M. C., Kiehl, J. T., Schwartz, S. E., and Benkovitz, C. M.: A description of the global sulfur cycle and its controlling processes in the National Center for Atmospheric Research Community Climate Model, Version 3, J. Geophys. Res.-Atmos., 105(D1), 1367–1385, 2000.

Rasch, P. J., Collins, W. D., and Eaton, B. E.: Understanding the Indian Ocean Experiment (INDOEX) aerosol distributions with an aerosol assimilation, J. Geophys. Res.-Atmos., 106(D7), 7337–7355, 2001.

Richter, J. H. and Rasch, P. J.: Effects of convective momentum transport on the atmospheric circulation in the community atmosphere model, version 3, J. Climate, 21(7), 1487–1499, doi:10.1175/2007jcli1789.1, 2008.

Riemer, N., Vogel, H., Vogel, B., and Fiedler, F.: Modeling aerosols on the mesoscale-gamma: Treatment of soot aerosol and its radiative effects, J. Geophys. Res.-Atmos., 108(D19), 4601, doi:10.1029/2003jd003448, 2003.

Riemer, N., West, M., Zaveri, R. A., and Easter, R. C.: Simulating the evolution of soot mixing state with a particle-resolved aerosol model, J. Geophys. Res.-Atmos., 114, D09202, doi:10.1029/2008jd011073, 2009.

Rossow, W. B. and Schiffer, R. A.: Advances in understanding clouds from ISCCP, B. Am. Meteorol. Soc., 80, 2261–2287, 1999.

Savoie, D. I., Prospero, J. M., Larsen, R. J., Huang, F., Izaguirre, M. A., Huang, T., Snowdon, T. H., Custals, L., and Sanderson, C. G.: Nitrogen and sulfur species in Antarctic aerosols at Mawson, Palmer Station, and Marsh (King George Island), J. Atmos. Chem., 17, 95–122, 1993.

Savoie, D. L., Prospero, J. M., and Saltzman, E. S.: Nitrate, nonseasalt sulfate and methanesulfonate over the Pacific Ocean, in: Chemical Oceanography, edited by: Ridley, J. P., Chester, R., and Duce, R. A., Elsevier, New York, 219–250, 1989.

GMDD
4, 3485–3598, 2011

Schwarz, J. P., Gao, R. S., Fahey, D. W., Thomson, D. S., Watts, L. A., Wilson, J. C., Reeves, J. M., Darbeheshti, M., Baumgardner, D. G., Kok, G. L., Chung, S. H., Schulz, M., Hendricks, J., Lauer, A., Kaercher, B., Slowik, J. G., Rosenlof, K. H., Thompson, T. L., Langford, A. O., Loewenstein, M., and Aikin, K. C.: Single-particle measurements of midlatitude black carbon and light-scattering aerosols from the boundary layer to the lower stratosphere, J. Geophys. Res., 111, D16207, doi:10.1029/2006jd007076, 2006.

Schwarz, J. P., Spackman, J. R., Gao, R. S., Watts, L. A., Stier, P., Schulz, M., Davis, S. M., Wofsy, S. C., and Fahey, D. W.: Global scale black carbon profiles observed in the remote atmosphere and compared to models, Geophys. Res. Lett., 37, L18812, doi:10.1029/2010GL044372, 2010.

Shinozuka, Y., Clarke, A. D., Howell, S. G., Kapustin, V. N., McNaughton, C. S., Zhou, J. C., and Anderson, B. E.: Aircraft profiles of aerosol microphysics and optical properties over North America: aerosol optical depth and its association with $PM_{2.5}$ and water uptake, J. Geophys. Res., 112, D12S20, doi:10.1029/2006jd007918, 2007.

Seinfeld, J. H. and Pandis, S. N.: Atmospheric Chemistry and Physics: from Air Pollution to Climate Change, John Wiley, Hoboken, NJ, 1998.

Sihto, S.-L., Kulmala, M., Kerminen, V.-M., Dal Maso, M., Petäjä, T., Riipinen, I., Korhonen, H., Arnold, F., Janson, R., Boy, M., Laaksonen, A., and Lehtinen, K. E. J.: Atmospheric sulphuric acid and aerosol formation: implications from atmospheric measurements for nucleation and early growth mechanisms, Atmos. Chem. Phys., 6, 4079–4091, doi:10.5194/acp-6-4079-2006, 2006.

Slingo, J. M.: A cloud parametrization scheme derived from gate data for use with a numerical-model, Q. J. Roy. Meteorol. Soc., 106(450), 747–770, 1980.

Smith, R. N. B.: A scheme for predicting layer clouds and their water content in a general circulation model, Q. J. Roy. Meteorol. Soc., 116, 435–460, 1990.

Smith, S. J., Pitcher, H., and Wigley, T. M. L.: Global and regional anthropogenic sulfur dioxide emissions, Global Planet. Change, 29(1–2), 99–119, 2001.

Smith, S. J., Andres, R., Conception, E., and Lurz, J.: Historical Sulfur Dioxide Emissions 1850–2000: Methods and Results, Pacific Northwest National Laboratory, Joint Global Change Research Institute, 2004.

Sokolik, I. N. and Toon, O. B.: Direct radiative forcing by anthropogenic airborne mineral aerosols, Nature, 381(6584), 681–683, 1996.

Spracklen, D. V., Pringle, K. J., Carslaw, K. S., Chipperfield, M. P., and Mann, G. W.: A global

GMDD
4, 3485–3598, 2011

off-line model of size-resolved aerosol microphysics: I. Model development and prediction of aerosol properties, Atmos. Chem. Phys., 5, 2227–2252, doi:10.5194/acp-5-2227-2005, 2005.
Stevens, B. and Feingold, G.: Untangling aerosol effects on clouds and precipitation in a buffered system, Nature, 461, doi:10.1038/nature08281, 2009.
Stier, P., Feichter, J., Kinne, S., Kloster, S., Vignati, E., Wilson, J., Ganzeveld, L., Tegen, I., Werner, M., Balkanski, Y., Schulz, M., Boucher, O., Minikin, A., and Petzold, A.: The aerosol-climate model ECHAM5-HAM, Atmos. Chem. Phys., 5, 1125–1156, doi:10.5194/acp-5-1125-2005, 2005.
Textor, C., Schulz, M., Guibert, S., Kinne, S., Balkanski, Y., Bauer, S., Berntsen, T., Berglen, T., Boucher, O., Chin, M., Dentener, F., Diehl, T., Easter, R., Feichter, H., Fillmore, D., Ghan, S., Ginoux, P., Gong, S., Grini, A., Hendricks, J., Horowitz, L., Huang, P., Isaksen, I., Iversen, I., Kloster, S., Koch, D., Kirkevåg, A., Kristjansson, J. E., Krol, M., Lauer, A., Lamarque, J. F., Liu, X., Montanaro, V., Myhre, G., Penner, J., Pitari, G., Reddy, S., Seland, Ø., Stier, P., Takemura, T., and Tie, X.: Analysis and quantification of the diversities of aerosol life cycles within AeroCom, Atmos. Chem. Phys., 6, 1777–1813, doi:10.5194/acp-6-1777-2006, 2006.
Tie, X., Brasseur, G., Emmons, L., Horowitz, L., and Kinnison, D.: Effects of aerosols on tropospheric oxidants: a global model study, J. Geophys. Res.-Atmos., 106(D19), 22931–22964, 2001.
Turner, D. D., Tobin, D. C., Clough, S. A., Brown, P. D., Ellingson, R. G., Mlawer, E. J., Knuteson, R. O., Revercomb, H. E., Shippert, T. R., Smith, W. L., and Shephard, M. W.: The QME AERI LBLRTM: a closure experiment for downwelling high spectral resolution infrared radiance, J. Atmos. Sci., 61(22), 2657–2675, 2004.
Vehkamäki, H., Kulmala, M., Napari, I., Lehtinen, K. E. J., Timmreck, C., Noppel, M., and Laaksonen, A.: An improved parameterization for sulfuric acid-water nucleation rates for tropospheric and stratospheric conditions, J. Geophys. Res.-Atmos., 107, 4622, doi:10.1029/2002jd002184, 2002.
Vignati, E., Wilson, J., and Stier, P.: M7: an efficient size-resolved aerosol microphysics module for large-scale aerosol transport models, J. Geophys. Res.-Atmos., 109(D22), D22202, doi:10.1029/2003jd004485, 2004.
Wang, J., Cubison, M. J., Aiken, A. C., Jimenez, J. L., and Collins, D. R.: The importance of aerosol mixing state and size-resolved composition on CCN concentration and the variation of the importance with atmospheric aging of aerosols, Atmos. Chem. Phys., 10, 7267–7283,

GMDD
4, 3485–3598, 2011

doi:10.5194/acp-10-7267-2010, 2010.
Wang, M. H., Penner, J. E., and Liu, X. H.: Coupled IMPACT aerosol and NCAR CAM3 model: evaluation of predicted aerosol number and size distribution, J. Geophys. Res.-Atmos., 114, D06302, doi:10.1029/2008jd010459, 2009.
Wang, M., Ghan, S., Easter, R., Ovchinnikov, M., Liu, X., Kassianov, E., Qian, Y., Gustafson Jr., W. I., Larson, V. E., Schanen, D. P., Khairoutdinov, M., and Morrison, H.: The multi-scale aerosol-climate model PNNL-MMF: model description and evaluation, Geosci. Model Dev., 4, 137–168, doi:10.5194/gmd-4-137-2011, 2011.
Weng, F. Z. and Grody, N. C.: Retrieval of cloud liquid water using the Special Sensor Microwave Imager (SSM/I), J. Geophys. Res., 99, 25535–25551, 1994.
Wilson, J., Cuvelier, C., and Raes, F.: A modeling study of global mixed aerosol fields, J. Geophys. Res.-Atmos., 106(D24), 34081–34108, 2001.
Wiscombe, W. J.: Mie scattering calculations: advances in technique and fast, vector-speed computer codes, National Center for Atmospheric Research, Tech. Note TN-140+STR, 62 pp., 1979.
Wright, D. L., Kasibhatla, P. S., McGraw, R., and Schwartz, S. E.: Description and evaluation of a six-moment aerosol microphysical module for use in atmospheric chemical transport models, J. Geophys. Res.-Atmos., 106(D17), 20275–20291, 2001.
Wylie, D., Jackson, D. L., Menzel, W. P., and Bates, J. J.: Trends in global cloud cover in two decades of HIRS observations, J. Climate, 18, 3021–3031, 2005.
Yang, P., Wei, H. L., Huang, H. L., Baum, B. A., Hu, Y. X., Kattawar, G. W., Mishchenko, M. I., and Fu, Q.: Scattering and absorption property database for nonspherical ice particles in the near- through far-infrared spectral region, Appl. Optics 44(26), 5512–5523, 2005.
Yoon, C. and McGraw, R.: Representation of generally mixed multivariate aerosols by the quadrature method of moments: II. Aerosol dynamics, J. Aerosol Sci., 35(5), 577–598, doi:10.1016/J.Jaerosci.2003.11.012, 2004.
Yoshioka, M., Mahowald, N., Conley, A., Collins, W., Fillmore, D., and Coleman, D.: Impact of desert dust radiative forcing on Sahel precipitation: relative importance of dust compared to sea surface temperature variations, vegetation changes and greenhouse gas warming, J. Climate, 20, 1445–1467, doi:10.1175/JCLI4056.1, 2007.
Young, K. C.: The role of contact nucleation in ice phase initiation in clouds, J. Atmos. Sci., 31, 768–776, 1974.
Zaveri, R. A., Easter, R. C., Fast, J. D., and Peters, L. K.: Model for Simulat-

GMDD
4, 3485–3598, 2011

ing Aerosol Interactions and Chemistry (MOSAIC), J. Geophys. Res., 113, D13204, doi:10.1029/2007JD008782, 2008.

Zaveri, R. A., Easter, R. C., Barnard, J. C., Riemer, N., and West, M.: Particle-resolved simulation of aerosol size, composition, mixing state, and the associated optical and cloud condensation nuclei activation properties in an evolving urban plume, J. Geophys. Res.-Atmos., 115, D17210, doi:10.1029/2009JD013616, 2010.

Zender, C., Bian, H., and Newman, D.: Mineral Dust Entrainment and Deposition (DEAD) model: description and 1990s dust climatology, J. Geophys. Res., 108(D14), 4416, doi:4410.1029/2002JD002775, 2003.

Zhang, G. J. and McFarlane, N. A.: Sensitivity of climate simulations to the parameterization of cumulus convection in the Canadian Climate Center general-circulation model, Atmos. Ocean, 33(3), 407–446, 1995.

Zhang, L. M., Gong, S. L., Padro, J., and Barrie, L.: A size-segregated particle dry deposition scheme for an atmospheric aerosol module, Atmos. Environ., 35(3), 549–560, 2001.

Zhang, M. H., Lin, W. Y., Bretherton, C. S., Hack, J. J., and Rasch, P. J.: A modified formulation of fractional stratiform condensation rate in the NCAR Community Atmospheric Model (CAM2), J. Geophys. Res.-Atmos., 108(D1), 4035, doi:10.1029/2002jd002523, 2003.

Zhang Q., Jimenez, J. L., Canagaratna M. R., Allan, J. D., Coe, H., Ulbrich, I., Alfarra, M. R., Takami, A., Middlebrook, A. M., Sun, Y. L., Dzepina, K., Dunlea, E., Docherty, K., DeCarlo, P. F., Salcedo, D., Onasch, T., Jayne, J. T., Miyoshi, T., Shimono, T., Hatakeyama, S., Takegawa, N., Kondo, Y., Schneider, J., Drewnick, F., Borrmann, S., Weimer, S., Demerjian, K., Williams, P., Bower, K., Bahreini, R., Cottrell, L., Griffin, R. J., Rautiainen, J., Sun, J. Y., Zhang, Y. M., and Worsnop, D. R.: Ubiquity and dominance of oxygenated species inorganic aerosols in anthropogenically influenced Northern Hemisphere midlatitudes, Geophys. Res. Lett., 34, L13801, doi:10.1029/2007GL029979, 2007.

Zhang, Y., Easter, R. C., Ghan, S. J., and Abdul-Razzak, H.: Impact of aerosol size representation on modeling aerosol-cloud interactions, J. Geophys. Res.-Atmos., 107(D21), doi:4558,10.1029/2001jd001549, 2002.

GMDD

4, 3485–3598, 2011

Table 1. Size distributions of primary aerosol emissions.

Emission source	Geometric standard deviation, σ_g	Number mode diameter, D_{gn} (μm)	D_{emit} (μm)[a]
BC/OM			
– Forest fire/grass fire	1.8	0.080	0.134
– Domestic/energy/industry/ transportation/waste/shipping	1.8[b]	0.080[b]	0.134[b]
SO_4			
– Forest fire/grass fire/waste/agriculture	1.8	0.080	0.134
– Energy/industry/shipping	–[c]	–[c]	0.261[c]
– Domestic/transportation	1.8	0.030	0.0504
– Continuous volcano, 50 % in Aitken mode	1.8	0.030	0.0504
– Continuous volcano, 50 % in accum. mode	1.8	0.080	0.134

[a] D_{emit} is volume-mean diameter = $D_{gn} \times \exp(1.5 \times (\ln(\sigma_g))^2)$ used in number emissions as $E_{number} = E_{mass}/(\pi/6 \times \rho D^3_{emit})$, and ρ is the aerosol particle density.

[b] This D_{emit} value is intermediate between the $D_{emit} = 0.0504$ μm in Dentener et al. (2006) and $D_{emit} = 0.206$ μm in Liu et al. (2005).

[c] Adapted from Stier et al. (2005) where 50 % of mass goes to accumulation mode with $D_{emit} = 0.207$ μm, and 50 % goes to coarse mode with $D_{emit} = 3.08$ μm. We put all mass in accumulation mode, and $D_{emit} = 0.261$ μm gives same number emissions as Stier et al. We note that Dentener et al. (2006) put all in coarse mode with $D_{emit} = 2.06$ μm.

GMDD
4, 3485–3598, 2011

Table 2. Assumed SOA yields.

Precursor species	Mass yield	Reference
Big alkanes	5 %	Lim and Ziemann (2005)
Big alkenes	5 %	assumed
Toluene	15 %	Odum et al. (1997)
Isoprene	4 %	Kroll et al. (2006)
Monoterpenes	25 %	Ng et al. (2007)

GMDD
4, 3485–3598, 2011

Table 3. Hygroscopicity of aerosol components.

Sea salt	Sulfate	Ammonium	SOA	POM	BC	Dust
1.16	0.507	0.507	0.14	0.10	10^{-10}	0.068

GMDD
4, 3485–3598, 2011

Table 4. Density (kg m^{-3}) of aerosol material.

Sea salt	Sulfate	Ammonium	SOA	POM	BC	Dust
1900	1770	1770	1000	1000	1700	2600

GMDD
4, 3485–3598, 2011

Table 5. Mapping of absorbing species from the MAM3 and MAM7 to the bulk aerosol scheme.

Bulk Aerosol	MAM3	MAM7
Hydrophilic BC	Accumulation mode BC	Same as MAM3
Hydrophobic BC	–	Primary-carbon mode BC
Hydrophilic OC	Accumulation mode POM + SOA	Same as MAM3
Hydrophobic OC	–	Primary-carbon mode OC
Dust, bin 1 (finest)	Accumulation mode dust	Fine-dust mode dust
Dust, bin 2	–	–
Dust, bin 3	Coarse mode dust	Coarse-dust mode dust
Dust, bin 4 (coarsest)	–	–

GMDD
4, 3485–3598, 2011

Table 6. Global budgets for DMS, SO_2, and H_2SO_4 (g) in MAM3 and MAM7.

	MAM3	MAM7	Previous studies (Liu et al., 2005)
	DMS		
Sources	18.2	18.2	
Emission	18.2	18.2	10.7–23.7
Sinks	18.2	18.3	
Gas-phase oxidation	18.2	18.3	10.7–23.7
Burden	0.067	0.067	0.02–0.15
Lifetime	1.34	1.32	0.5–3.0
	SO_2		
Sources	80.0	80.0	
Emission	64.8	64.8	63.7–92.0
DMS oxidation	15.2	15.2	10.0–24.7
Sinks	79.9	79.8	
Dry deposition	19.7	19.0	16.0–55.0
Wet deposition	17.6	16.8	0.0–19.9
Gas-phase oxidation	14.5	14.3	6.1–16.8
Aqueous-phase oxidation	28.0	29.7	24.5–57.8
Burden	0.35	0.34	0.20–0.61
Lifetime	1.60	1.55	0.6–2.6
	H_2SO_4 (g)		
Sources	14.5	14.3	
Gas-phase production	14.5	14.3	6.1–22.0
Sinks	14.5	14.3	
Dry deposition	0.002	0.003	
Aqueous-phase uptake	0.59	0.51	
Nucleation	0.030	0.030	
Condensation	13.9	13.7	
Burden (Tg S)	0.00040	0.00042	9.0×10^{-6}–1.0×10^{-3}
Lifetime (min)	14.5	15.3	4.3–10.1

Units are sources and sinks, Tg S yr^{-1}; burden, Tg S; lifetime, days except for H_2SO_4 (min).

GMDD
4, 3485–3598, 2011

Table 7. Global annual budget for sulfate. The means and normalized standard deviations (in %) from available models participating in AeroCom (Textor et al., 2006) are listed. The values in parentheses are mean removal rates (in 1 d^{-1}) and normalized standard deviations (in %) as budget terms are not given in Textor et al. (2006). For comparison removal rates (in 1 d^{-1}) from MAM3 and MAM7 are listed in parentheses.

	MAM3	MAM7	AeroCom
Sources	44.30	45.71	59.67, 22
Emission	1.66	1.66	
SO_2 aqueous-phase oxidation	28.03	29.74	
from H_2O_2 chemistry (%)	53.9	48.1	
H_2SO_4 aqueous-phase uptake	0.59	0.51	
H_2SO_4 nucleation	0.030	0.030	
H_2SO_4 condensation	13.98	13.74	
Sinks	44.30	45.71	
Dry deposition	4.96 (0.03)	5.51 (0.03)	(0.03, 55)
Wet deposition	39.34 (0.23)	40.20 (0.23)	(0.22, 22)
Burden	0.46	0.47	0.66, 25
In modes (%)	2.8 (Aitken), 95.5 (accum.), 1.7 (coarse)	2.9 (Aitken), 88.9 (accum.), 1.1 (fine sea salt), 5.9 (fine dust), 0.32 (coarse sea salt), 0.88 (coarse dust)	
Lifetime	3.77	3.72	4.12, 18

Units are sources and sinks, Tg S yr^{-1}; burden, Tg S; lifetime, days.

GMDD
4, 3485–3598, 2011

Table 8. Global budgets for NH_3 (g) and NH_4 in MAM7. The results from other studies are from Feng and Penner (2007) and references therein.

	MAM7	Previous studies (Feng and Penner, 2007)
	NH_3 (g)	
Sources	48.8	
Emission	46.0	52.1–54.1
Gas/aqueous-phase partitioning	2.8	
Sinks	48.9	
Dry deposition	12.5	15.4–29.4
Wet deposition	10.4	7.4–16.7
Nucleation	0.014	
Condensation	26.0	
Burden	0.064	0.084–0.19
Lifetime	0.48	0.57–1.4
	NH_4	
Sources	26.0	4.5–26.1
NH_3 condensation	26.0	
NH_3 nucleation	0.014	
Sinks	26.1	
Dry deposition	3.4	0.2–6.6
Wet deposition	19.9	4.3–23.0
Gas/aqueous-phase partitioning	2.8	
Burden	0.24	0.045–0.30
In modes (%)	1.8 (Aitken), 89.9 (accum.), 1.5 (fine sea salt), 5.7 (fine dust), 0.42 (coarse sea salt), 0.74 (coarse dust)	
Lifetime	3.4	3.6–4.2

Units are sources and sinks, Tg N yr^{-1}; burden, Tg N; lifetime, days.

GMDD
4, 3485–3598, 2011

Table 9. Global budgets for organic aerosol. For POM, the means and normalized standard deviations (in %) from available models participating in AeroCom (Textor et al., 2006) are listed. The values in parentheses are mean removal rates (in $1\,d^{-1}$) and normalized standard deviations (in %) as budget terms are not given in Textor et al. (2006). For comparison removal rates (in $1\,d^{-1}$) from MAM3 and MAM7 are listed in parentheses. For SOA, the mean and normalized standard deviations (in %) from other studies are from Farina et al. (2010) and references therein.

	MAM3	MAM7	AeroCom/ other studies
	POM		
Sources	50.2	50.2	96.6, 26
Fossil and bio-fuel emission	16.8	16.8	
Biomass burning emission	33.4	33.4	
Sinks	50.1	50.1	
Dry deposition	7.4 (0.03)	8.4 (0.03)	(0.03, 49)
Wet deposition	42.7 (0.19)	41.7 (0.17)	(0.14, 32)
Burden	0.63	0.68	1.70, 27
In modes (%)	100 (accum.)	14.7 (primary carbon) 85.3 (accum.)	
Lifetime	4.56	4.90	6.54, 27
	SOA		
Sources	103.3	103.3	34.0, 123
Condensation of SOA (g)	103.3	103.3	
Sinks	103.2	103.2	
Dry deposition	11.2 (0.03)	11.3 (0.03)	
Wet deposition	92.0 (0.22)	91.9 (0.22)	
Burden	1.15	1.15	0.57, 117
In modes (%)	0.8 (Aitken) 99.2 (accum.)	1.0 (Aitken) 99.0 (accum.)	
Lifetime	4.08	4.08	6.70, 115

Units are sources and sinks, $Tg\,yr^{-1}$; burden, Tg; lifetime, days.

GMDD
4, 3485–3598, 2011

Table 10. Global budgets for BC. The means and normalized standard deviations (in %) from available models participating in AeroCom (Textor et al., 2006) are listed. The values in parentheses are mean removal rates (in 1 d^{-1}) and normalized standard deviations (in %) as budget terms are not given in Textor et al. (2006). For comparison removal rates (in 1 d^{-1}) from MAM3 and MAM7 are listed in parentheses.

	MAM3	MAM7	AeroCom
Sources	7.76	7.76	11.9, 23
Fossil and bio-fuel emission	5.00	5.00	
Biomass burning emission	2.76	2.76	
Sinks	7.75	7.75	
Dry deposition	1.27 (0.04)	1.41 (0.04)	(0.03, 55)
Wet deposition	6.48 (0.20)	6.34 (0.19)	(0.12, 31)
Burden	0.088	0.093	0.24, 42
In modes (%)	100 (accum.)	10.8 (primary carbon) 89.2 (accum.)	
Lifetime	4.17	4.37	7.12, 33

Units are sources and sinks, Tg yr^{-1}; burden, Tg; lifetime, days.

GMDD
4, 3485–3598, 2011

Table 11. Global budgets for dust. The means, medians and normalized standard deviations (in %) from available models participating in AeroCom (Textor et al., 2006) are listed. The values in parentheses are mean and median removal rates (in 1 d^{-1}) and normalized standard deviations (in %) as budget terms are not given in Textor et al. (2006). For comparison removal rates (in 1 d^{-1}) from MAM3 and MAM7 are listed in parentheses.

	MAM3	MAM7	AeroCom
Sources	3121.9	2943.5	1840.0, 1640.0, 49
Sinks	3122.4	2945.6	
Dry deposition	1948.4 (0.24)	1732.7 (0.19)	(0.23, 0.16, 84)
from gravitational settling (%)	89.7	89.1	46.2, 40.9, 66
Wet deposition	1174.0 (0.14)	1212.9 (0.13)	(0.08, 0.09, 42)
Burden	22.4	24.7	19.2, 20.5, 40
In modes (%)	8.0 (accum.) 92.0 (coarse)	29.5 (fine) 70.5 (coarse)	
Lifetime	2.61	3.07	4.14, 4.04, 43

Units are sources and sinks, Tg yr^{-1}; burden, Tg; lifetime, days.

GMDD
4, 3485–3598, 2011

Table 12. Global budgets for sea salt. The means, medians and normalized standard deviations (in %) from available models participating in AeroCom (Textor et al., 2006) are listed. The values in parentheses are mean and median removal rates (in 1 d^{-1}) and normalized standard deviations (in %) as budget terms are not given in Textor et al. (2006). For comparison removal rates (in 1 d^{-1}) from MAM3 and MAM7 are listed in parentheses.

	MAM3	MAM7	AeroCom
Sources	4965.5	5004.1	16600.0, 6280.0, 199
Sinks	4962.9	5001.3	
Dry deposition	2410.3 (0.64)	3073.8 (1.11)	(4.28, 1.40, 219)
from gravitational settling (%)	56.6	60.8	58.9, 59.5, 65
Wet deposition	2552.6 (0.67)	1927.4 (0.70)	(0.79, 0.68, 77)
Burden	10.37	7.58	7.52, 6.37, 54
In modes (%)	~ 0.0 (Aitken)	~ 0.0 (Aitken)	
	7.5 (accum.)	1.1 (accum.)	
	92.5 (coarse)	8.0 (fine sea salt)	
		90.9 (coarse sea salt)	
Lifetime	0.76	0.55	0.48, 0.41, 58

Units are sources and sinks, Tg yr^{-1}; burden, Tg; lifetime, days.

GMDD
4, 3485–3598, 2011

Table 13. Mean of observations, and normalized mean bias (NMB) and correlation coefficients (R) between model simulations and observations for AOD over the seven regions in Fig. 23. The NMB is calculated from the difference between model and observation divided by observation.

	North America	Europe	East Asia	Northern Africa	Southern Africa	South America	South Asia	Global
Mean (obs)	0.13	0.18	0.34	0.51	0.18	0.21	0.39	0.21
NMB (MAM3)	−0.28	−0.38	−0.53	−0.37	−0.39	−0.24	−0.71	−0.33
NMB (MAM7)	−0.28	−0.38	−0.50	−0.12	−0.33	−0.29	−0.72	−0.24
R (MAM3)	0.87	0.29	0.36	0.55	0.66	0.44	0.78	0.69
R (MAM7)	0.87	0.28	0.31	0.51	0.49	0.50	0.80	0.71

GMDD
4, 3485–3598, 2011

Table 14. Mean of observations and model simulations, and correlation coefficients (R) between model simulations and observations for SSA over the seven regions in Fig. 23.

	North America	Europe	East Asia	Northern Africa	Southern Africa	South America	South Asia	Global
Mean (obs)	0.93	0.91	0.92	0.91	0.89	0.88	0.90	0.92
Mean (MAM3)	0.92	0.91	0.88	0.90	0.91	0.94	0.92	0.91
Mean (MAM7)	0.92	0.91	0.88	0.91	0.90	0.94	0.92	0.91
R (MAM3)	0.28	−0.17	0.58	0.55	0.61	0.35	0.48	0.24
R (MAM7)	0.31	−0.16	0.61	0.51	0.61	0.28	0.47	0.27

GMDD
4, 3485–3598, 2011

Table 15. Global annual mean statistics from CAM5 with MAM3 and MAM7: shortwave (SWCF) and longwave (LWCF) cloud forcing, liquid water path (LWP), ice water path (IWP), total (CLDTOT), low (CLDLOW) and high (CLDHGH) cloud cover, column droplet number concentration (CDNUMC), column ice number concentration (CINUMC), and column CCN concentration at supersaturation of 0.1%.

Simulations	MAM3	MAM7	Observations
SWCF ($W\,m^{-2}$)	−48.8	−48.9	−46 to −53[a]
LWCF ($W\,m^{-2}$)	23.7	23.8	27–31[a]
LWP ($g\,m^{-2}$)	41.0	40.7	50–87[b]
IWP ($g\,m^{-2}$)	17.7	17.7	
CLDTOT (%)	62.9	63.0	65–75[c]
CLDLOW (%)	41.9	41.7	
CLDHGH (%)	38.0	38.4	21–33[d]
CDNUMC ($10^{10}\,m^{-2}$)	1.27	1.19	
CINUMC ($10^{10}\,m^{-2}$)	0.0092	0.0094	
Column CCN at $S = 0.1\,\%$ ($10^{10}\,m^{-2}$)	24.4	21.5	

[a] SWCF, LWCF are from ERBE for the years 1985–1989 (Kiehl and Trenberth, 1997) and CERES for the years 2000–2005 (Loeb et al., 2009).

[b] Liquid water path is derived from SSM/I (for the years 1987–1994, Ferraro et al., 1996; for August 1993 and January 1994, Weng and Grody, 1994; and for August 1987 and February 1988, Greenwald et al., 1993) and ISCCP for the year 1987 (Han et al., 1994). SSM/I data are restricted to oceans.

[c] Total cloud fraction observations are obtained from ISCCP for the years 1983–2001 (Rossow and Schiffer, 1999), MODIS data for the years 2001–2004 (Platnick et al., 2003) and HIRS data for the years 1979–2001 (Wylie et al., 2005).

[d] High cloud fraction observations are obtained from ISCCP data for the years 1983–2001 and HIRS for the years 1979–2001.

GMDD
4, 3485–3598, 2011

Table 16. Global budgets for primary organic aerosol from MAM7, MAM-k and MAM-aging runs.

	MAM7	MAM7-k	MAM7-aging
POA (primary mode)			
Sources	50.2	50.2	50.2
Fossil and bio-fuel emission	16.8	16.8	16.8
Biomass burning emission	33.4	33.4	33.4
Sinks	50.2	50.2	50.2
Dry deposition	2.5	2.8	4.5
Wet deposition	2.6	0.004	0.009
Aged to accumulation mode	45.1	47.4	45.7
Burden	0.10	0.14	0.37
Lifetime	0.73	1.0	2.7
POA (accumulation mode)			
Sources			
Aged from primary mode	45.1	47.4	45.7
Sinks	44.9	47.3	45.6
Dry deposition	5.8	6.1	5.5
Wet deposition	39.1	41.2	40.1
Burden	0.58	0.61	0.60
Lifetime	4.7	4.7	4.8

Units are sources and sinks, Tg yr^{-1}; burden, Tg; lifetime, days.

GMDD
4, 3485–3598, 2011

Table 17. Global budgets for black carbon from MAM7, MAM7-k and MAM7-aging runs.

	MAM7	MAM7-k	MAM7-aging
BC (primary mode)			
Sources	7.76	7.76	7.76
Fossil and bio-fuel emission	5.00	5.00	5.00
Biomass burning emission	2.76	2.76	2.76
Sinks	7.76	7.76	7.76
Dry deposition	0.39	0.42	0.70
Wet deposition	0.33	0.00	0.00
Aged to accumulation mode	7.04	7.34	7.06
Burden	0.010	0.014	0.040
Lifetime	0.47	0.66	1.88
BC (accumulation mode)			
Sources			
Aged from primary mode	7.04	7.34	7.06
Sinks	7.03	7.32	7.05
Dry deposition	1.02	1.04	0.93
Wet deposition	6.01	6.28	6.12
Burden	0.083	0.086	0.085
Lifetime	4.3	4.3	4.4

Units are sources and sinks, Tg yr^{-1}; burden, Tg; lifetime, days.

GMDD
4, 3485–3598, 2011

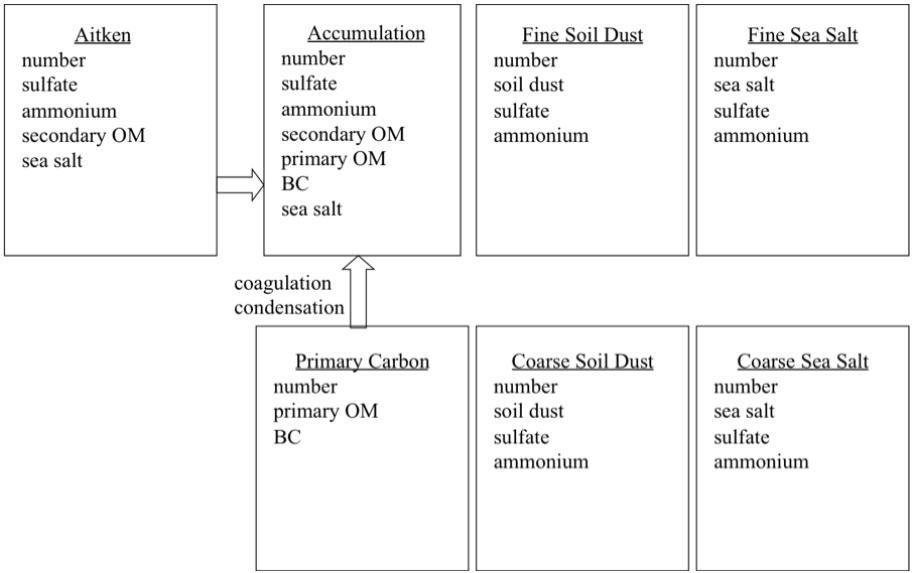

Fig. 1. Predicted species for interstitial and cloud-borne component of each aerosol mode in MAM7. Standard deviation for each mode is 1.6 (Aitken), 1.8 (accumulation), 1.6 (primary carbon), 1.8 (fine and coarse soil dust), and 2.0 (fine and coarse sea salt).

GMDD
4, 3485–3598, 2011

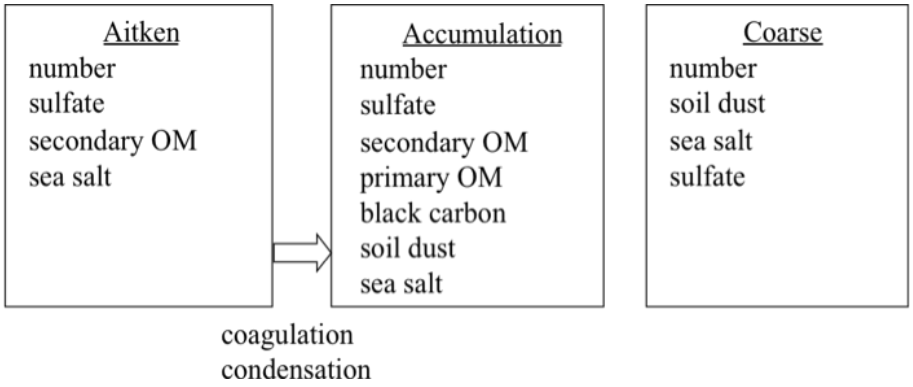

Fig. 2. Predicted species for interstitial and cloud-borne component of each aerosol mode in MAM3. Standard deviation for each mode is 1.6 (Aitken), 1.8 (accumulation) and 1.8 (coarse mode).

GMDD
4, 3485–3598, 2011

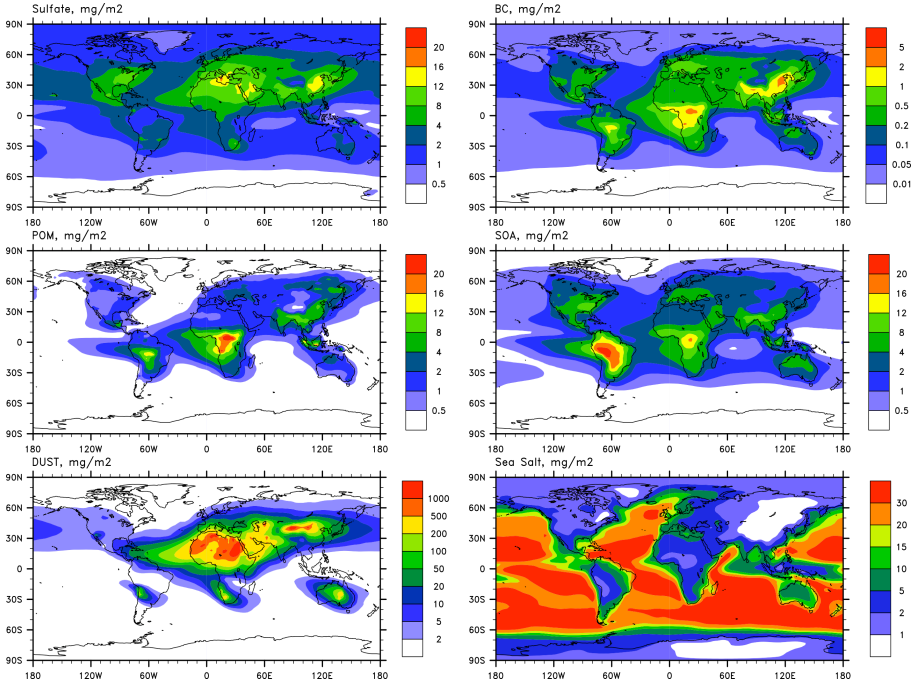

Fig. 3a. Annual mean vertically integrated concentrations (mg m^{-2}) of sulfate, BC, POM, SOA, dust, and sea salt from MAM3.

GMDD
4, 3485–3598, 2011

Toward a minimal representation of aerosol direct and indirect effects

X. Liu et al.

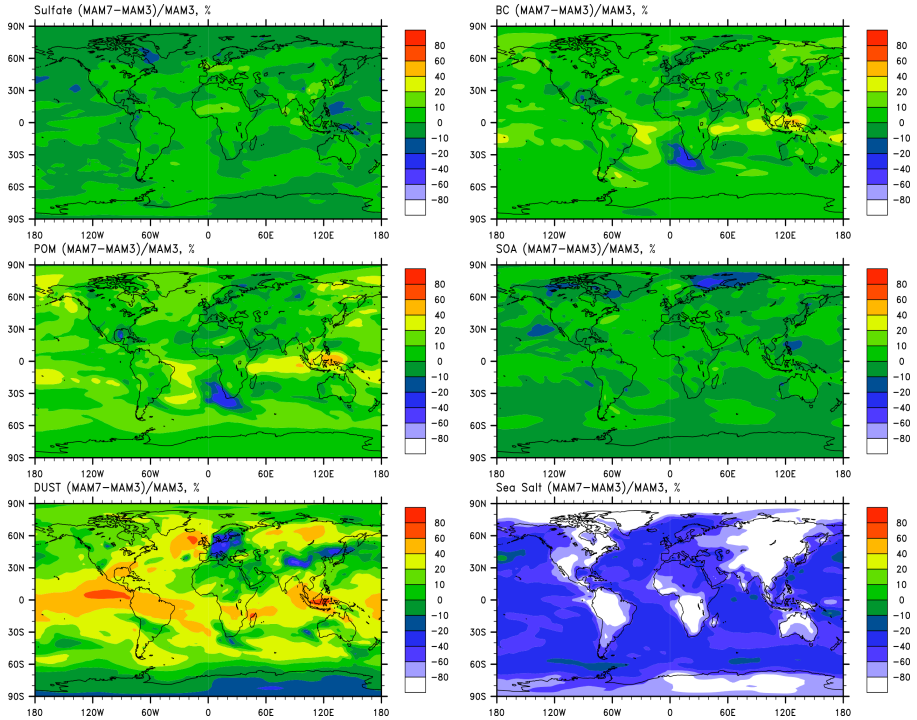

Fig. 3b. Relative differences (in %) of annual mean vertically integrated concentrations of sulfate, BC, POM, SOA, dust, and sea salt between MAM7 and MAM3.

GMDD
4, 3485–3598, 2011

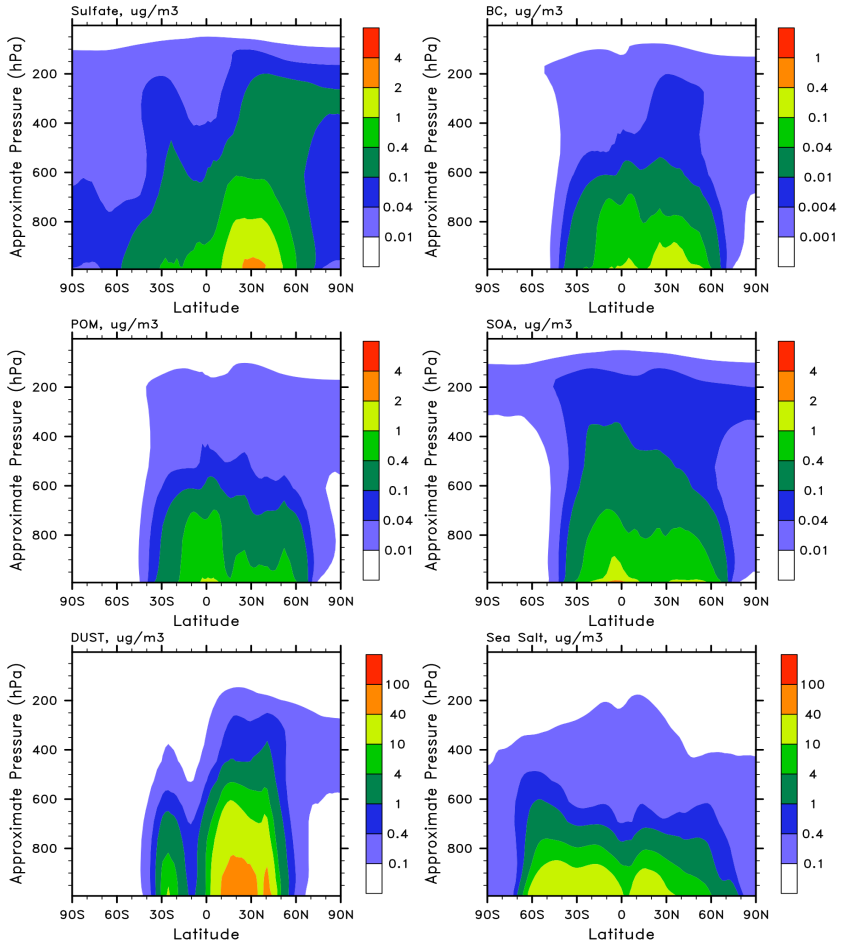

Fig. 4. Annual and zonal mean distributions of sulfate, BC, POM, SOA, dust and sea salt concentrations in MAM3.

GMDD
4, 3485–3598, 2011

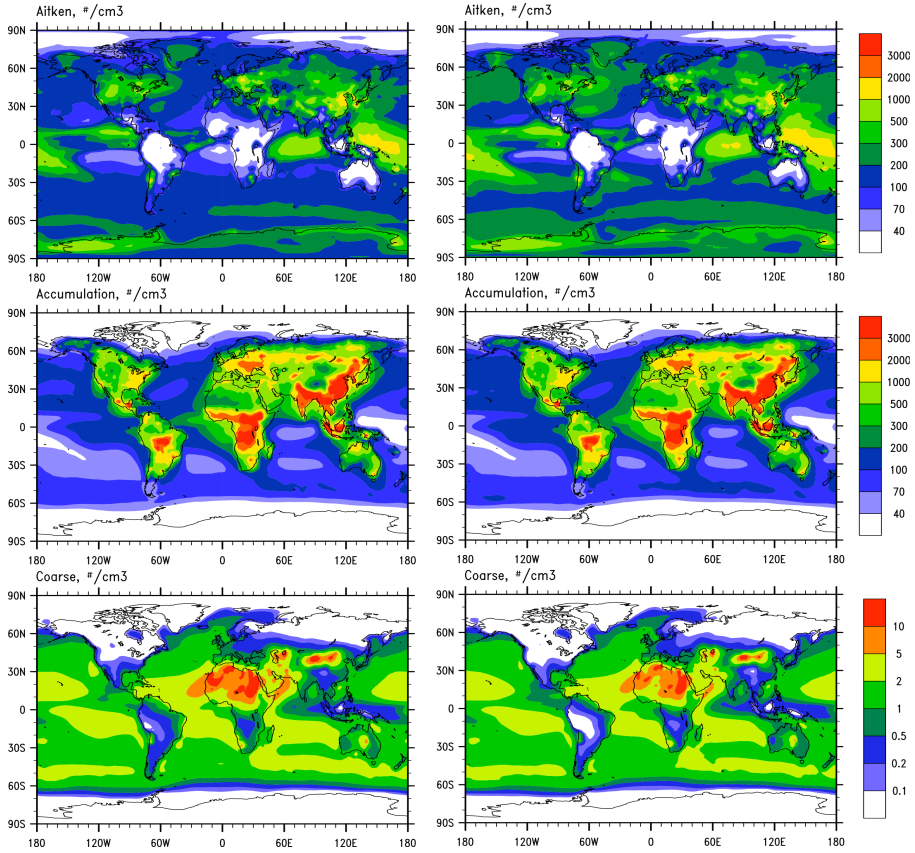

Fig. 5. Annual mean number concentration of aerosol in Aitken, accumulation and coarse mode in the surface layer from MAM3 (left) and MAM7 (right) at standard temperature and pressure (STP) (1013.25 hPa, 273.15 K).

GMDD
4, 3485–3598, 2011

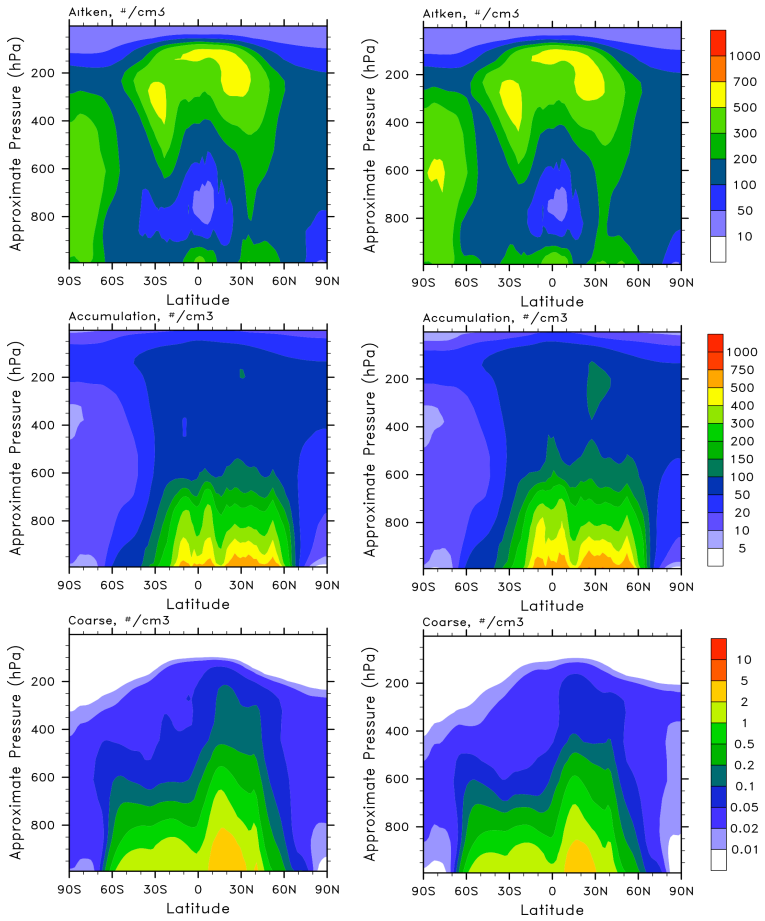

Fig. 6. Same as Fig. 5 except for annual and zonal mean aerosol number concentrations in Aitken, accumulation and coarse mode.

GMDD
4, 3485–3598, 2011

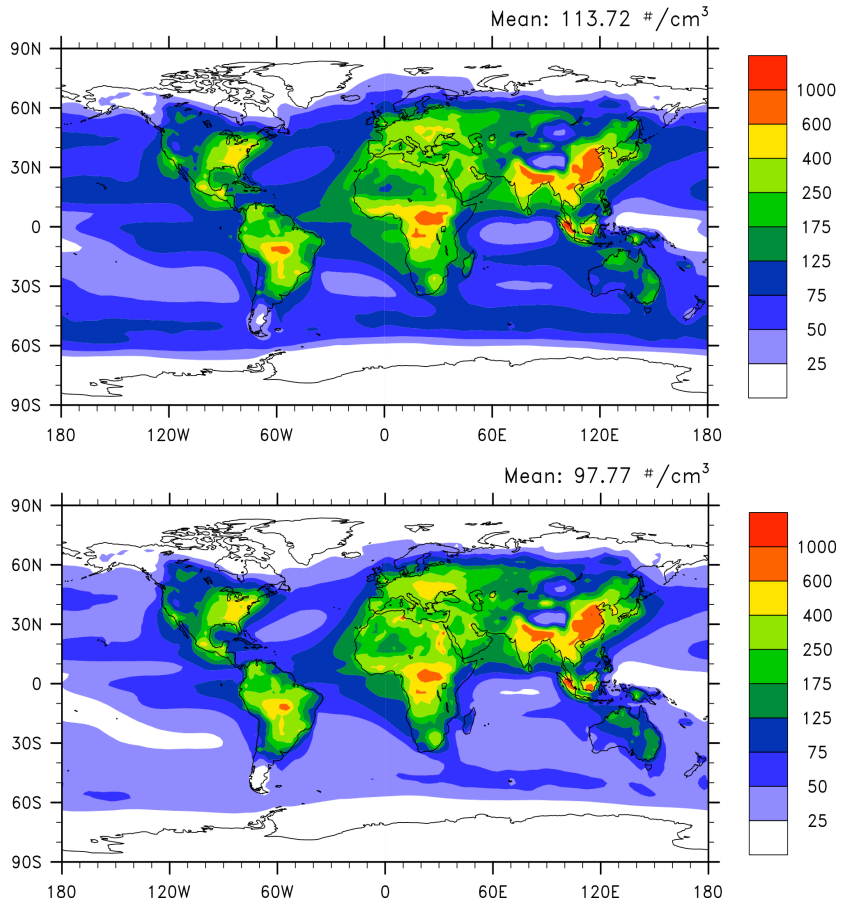

Fig. 7. Annual averaged global distribution of CCN number concentration at 0.1 % supersaturation (S) at surface in MAM3 (upper) and MAM7 (lower).

GMDD
4, 3485–3598, 2011

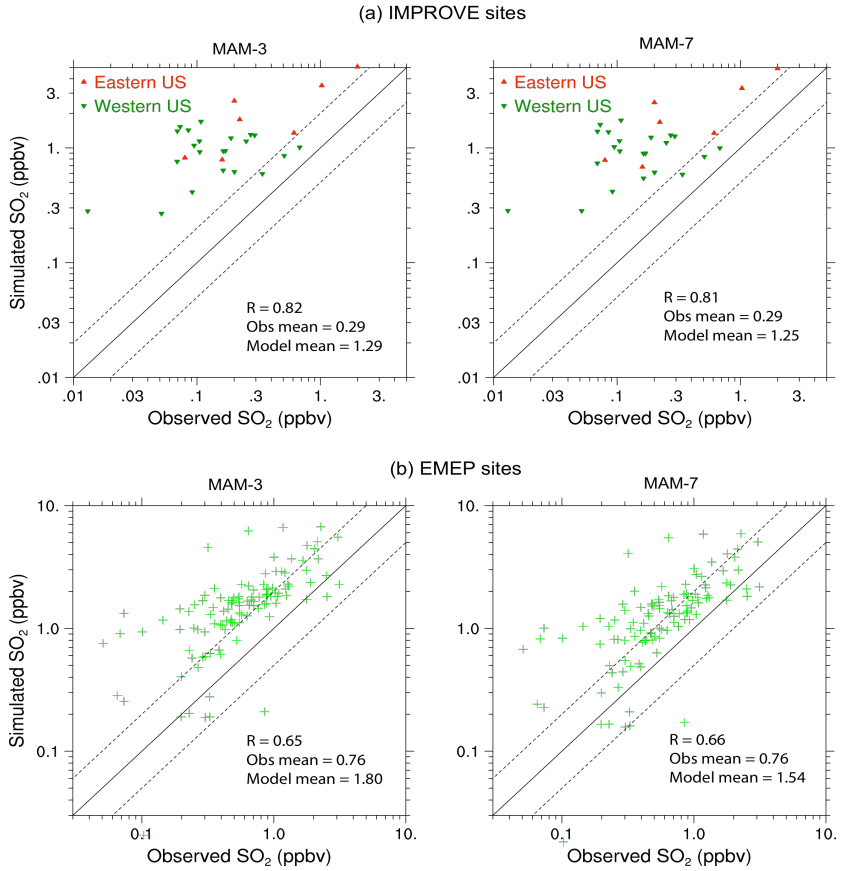

Fig. 8. Observed and simulated annual-average SO_2 mixing ratios at IMPROVE and EMEP network sites. Observations are for site-available years between 1990–2005 for IMPROVE sites and 1995–2005 for EMEP sites. Simulated values for MAM3 (left) and MAM7 (right) are from model lowest layer. Top: IMPROVE network, Eastern US sites are east of 97° W longitude. Bottom: EMEP network.

GMDD
4, 3485–3598, 2011

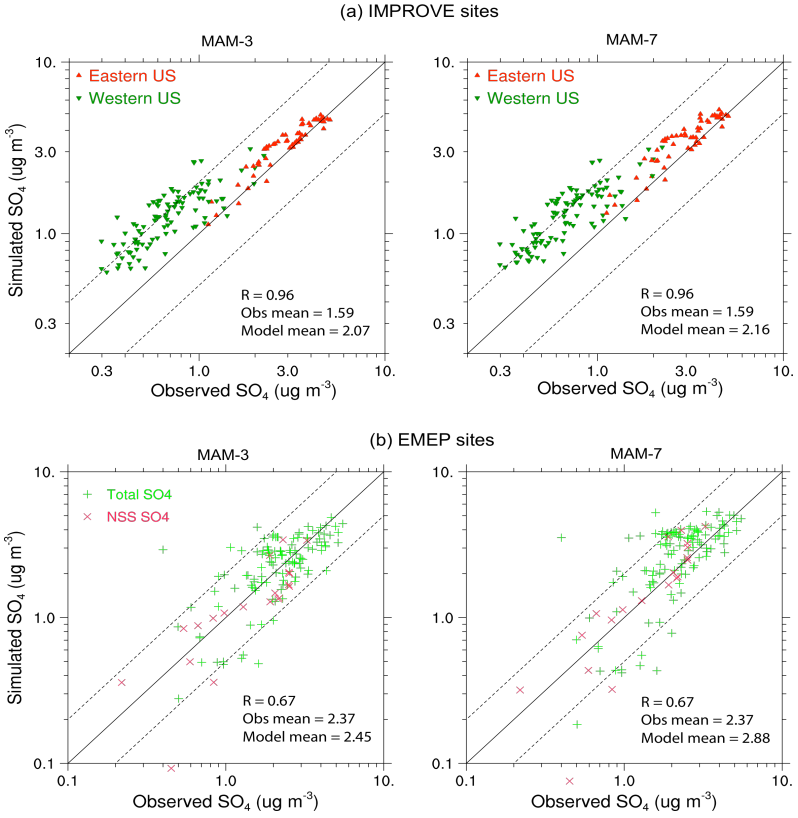

Fig. 9. Observed and simulated annual-average sulfate (SO_4) concentrations at IMPROVE and EMEP network sites. Observations are for site-available years between 1995–2005. Simulated values for MAM3 (left) and MAM7 (right) are from model lowest layer. Top: IMPROVE network, Eastern US sites are east of 97° W longitude. Bottom: EMEP network. EMEP plots show total and non-sea salt (nss) SO_4, and IMPROVE plots show total SO_4. The CAM5 SO_4 species are nss-SO_4, and simulated total SO_4 includes a sea-salt component equal to 7.7 % of the simulated sea salt concentration.

GMDD
4, 3485–3598, 2011

Toward a minimal representation of aerosol direct and indirect effects

X. Liu et al.

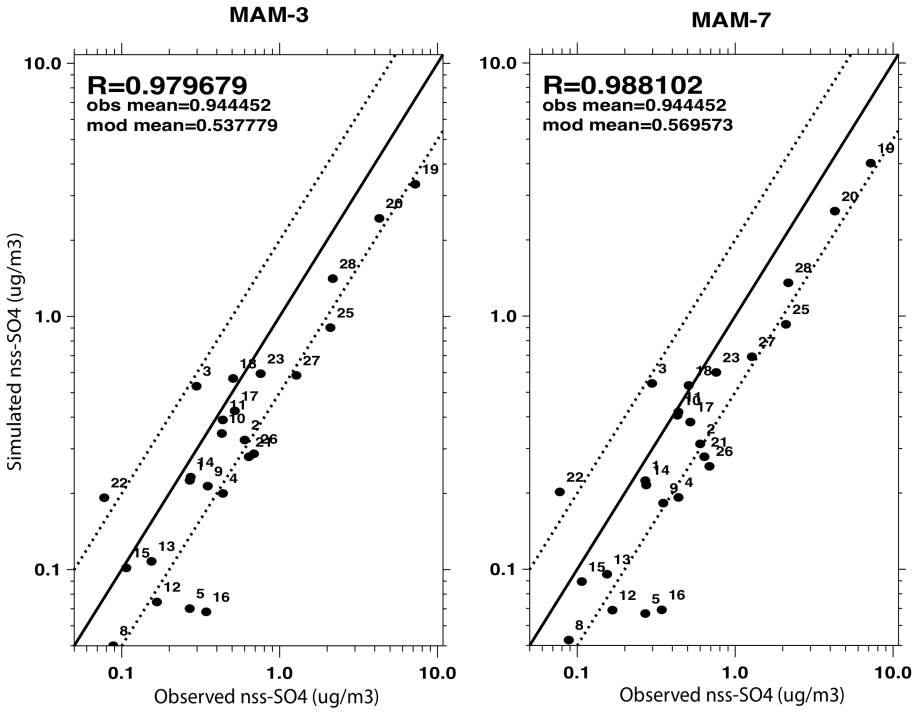

Fig. 10. Observed and simulated annual-average non-sea salt sulfate (nss-SO_4) concentrations ($\mu g\, m^{-3}$) at marine sites operated by the Rosenstiel School of Marine and Atmospheric Science (RSMAS) at the University of Miami. Observations are for site-available years between 1981–1998. Simulated values for MAM3 (left) and MAM7 (right) are from model lowest layer, and the Tenerife mountain site is not included. The global locations of sites denoted by different numbers in the figure can be found in Wang et al. (2011).

GMDD
4, 3485–3598, 2011

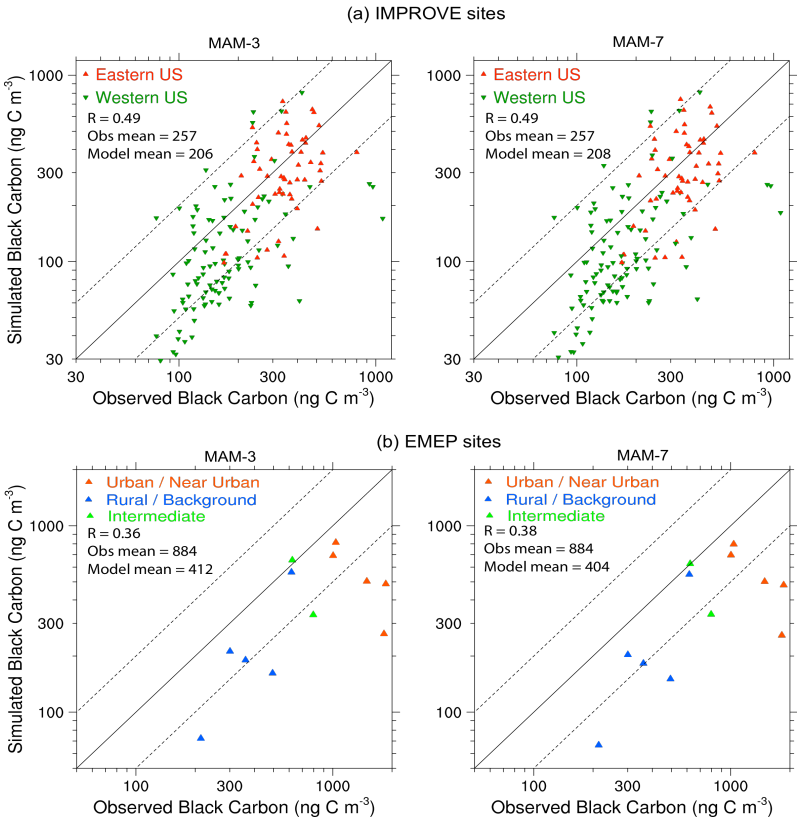

Fig. 11. Observed and simulated annual-average black carbon (BC) concentrations (ng C m^{-3}) at IMPROVE and EMEP BC/OC network sites. Observations are for site-available years between 1995–2005 for IMPROVE sites and July 2002–June 2003 for EMEP sites. Simulated values for MAM3 (left) and MAM7 (right) are from model lowest layer. Top: IMPROVE network, Eastern US sites are east of 97° W longitude. Bottom: EMEP network.

GMDD
4, 3485–3598, 2011

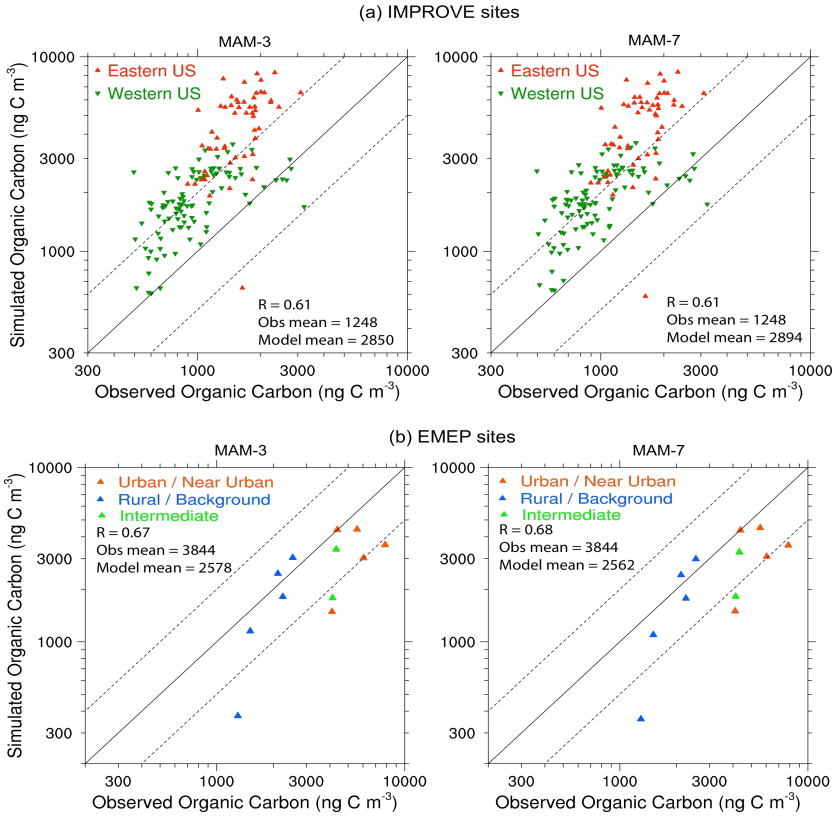

Fig. 12. Observed and simulated annual-average organic carbon (OC) concentrations (ng C m^{-3}) at IMPROVE and EMEP BC/OC network sites. Observations are for site-available years between 1995–2005 for IMPROVE sites and July 2002–June 2003 for EMEP sites. Simulated values for MAM3 (left) and MAM7 (right) are from model lowest layer and are equal to the modeled (POM + SOA)/1.4. Top: IMPROVE network, Eastern US sites are east of 97° W longitude. Bottom: EMEP network.

GMDD
4, 3485–3598, 2011

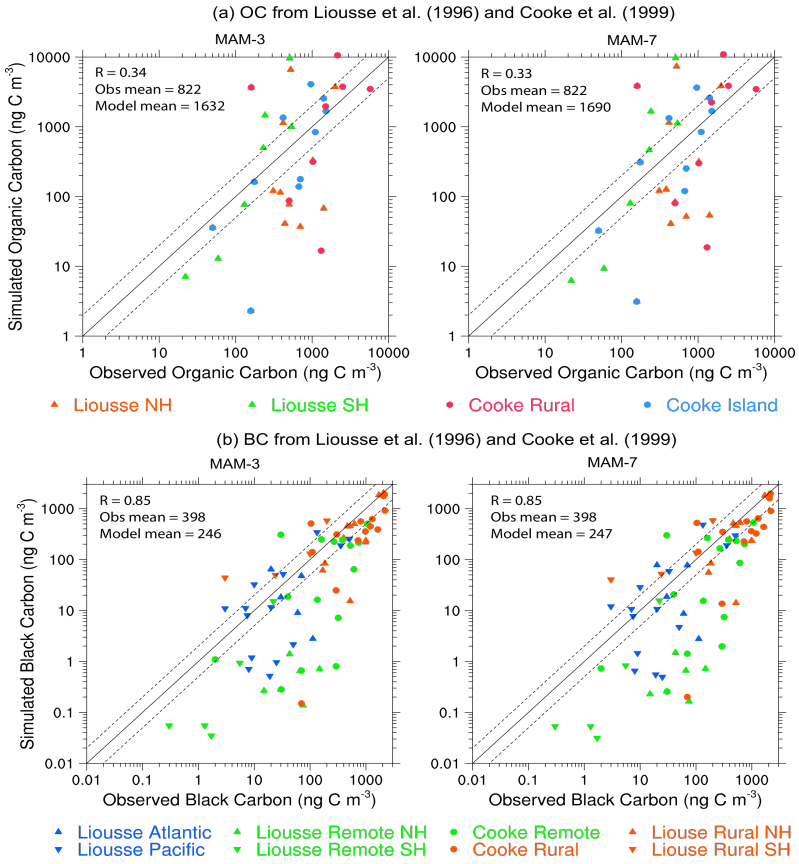

Fig. 13. Observed and simulated organic carbon (top) and black carbon (bottom) concentrations (ng C m^{-3}) at various locations and time periods. Observations are from the compilations of Liousse et al. (1996) and Cooke et al. (1999). Simulated values for MAM3 (left) and MAM7 (right) are from model lowest layer, and OC is the modeled (POM + SOA)/1.4.

GMDD
4, 3485–3598, 2011

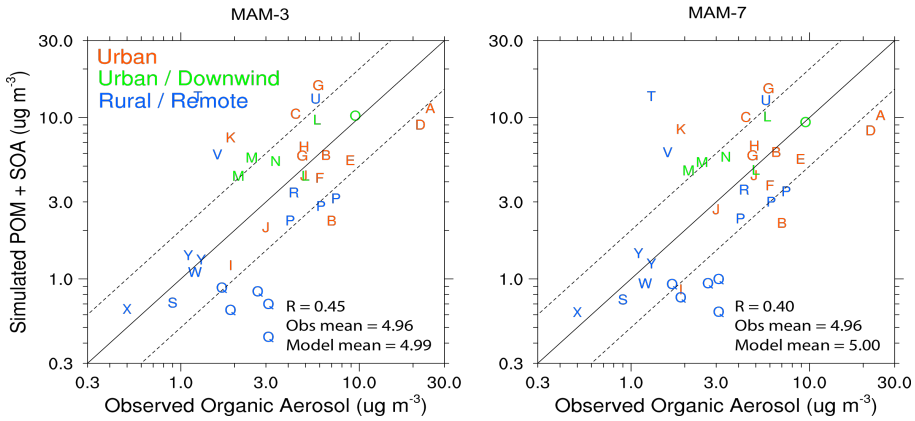

Fig. 14. Observed and simulated organic aerosol concentrations at various locations and times as reported compiled by Zhang et al. (2007). Simulated values for MAM3 (left) and MAM7 (right) are from model lowest layer except for Jungfraujoch site (symbol W).

GMDD
4, 3485–3598, 2011

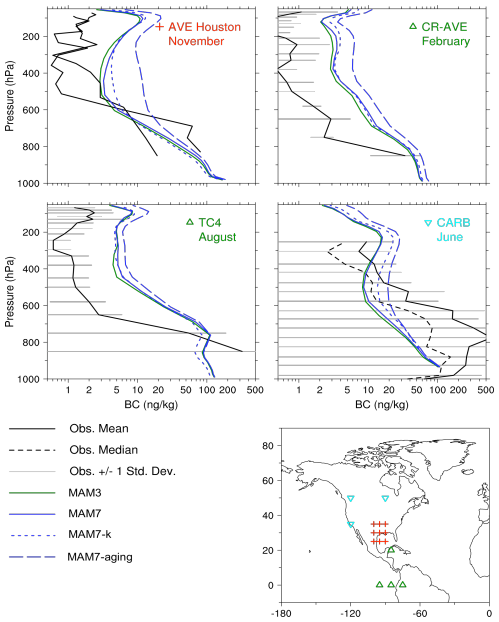

Fig. 15. Observed and simulated BC vertical profiles in the tropics and middle latitudes from 4 aircraft campaigns: AVE Houston (NASA Houston Aura Validation Experiment), CR-AVE (NASA Costa Rica Aura Validation Experiment), TC4 (Tropical Composition, Cloud and Climate Coupling), and CARB (NASA initiative in collaboration with California Air Resources Board). Observations are averages for the respective campaigns and were measured by three different investigator groups: NOAA (Schwarz et al., 2006) for AVE-Houston, CR-AVE, and TC4; University of Tokyo (Moteki and Kondo, 2007; Moteki et al., 2007) and University of Hawaii (Clarke et al., 2007; Howell et al., 2006; McNaughton et al., 2009; Shinozuka et al., 2007) for CARB. The Houston campaign has two profiles from two different days. See Koch et al. (2009) for additional details. Simulated profiles for MAM3 and MAM7 are averaged over the points on the map and the indicated month. Two sensitivity experiments are included: MAM7-k and MAM7-aging, as discussed in Sect. 5.

GMDD
4, 3485–3598, 2011

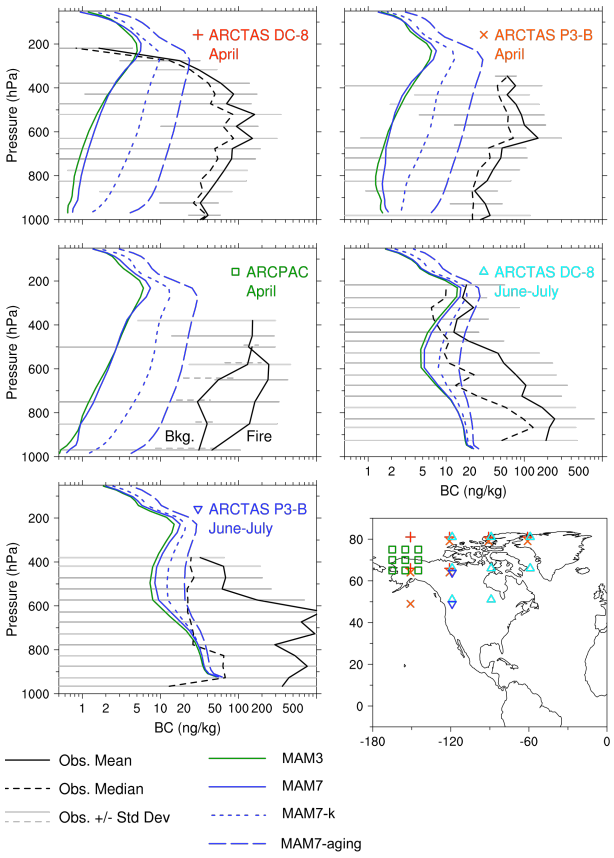

Fig. 16. Same as Fig. 15 but for BC vertical profiles at high latitudes from over two campaigns: ARCTAS (NASA Arctic Research of the Composition of the Troposphere from Aircraft and Satellite), and ARCPAC (NOAA Aerosol, Radiation, and Cloud Processes affecting Arctic Climate). Observations are from the NOAA group for ARCPAC, and from the University of Tokyo and University of Hawaii groups for ARCTAS.

GMDD
4, 3485–3598, 2011

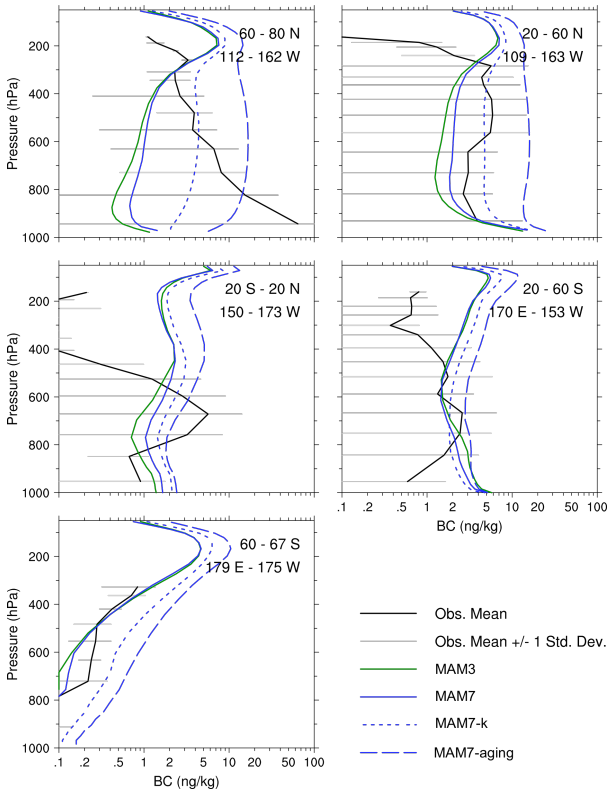

Fig. 17. Same as Fig. 16, but for BC vertical profiles above W. Canada, Alaska, the Arctic Ocean, and the remote Pacific Ocean during the HIAPER Pole-to-Pole Observations (HIPPO) campaign in January 2009 (Schwarz et al., 2010). The observational data was grouped into five latitude zones (67–60° S, 60–20° S, 20° S–20° N, 20–60° N, and 60–80° N). Simulated profiles for MAM3 and MAM7 are averaged over January and the flight track segments within each latitude zone. Two sensitivity experiments are included: MAM7-k and MAM7-aging, as discussed in Sect. 5.

GMDD
4, 3485–3598, 2011

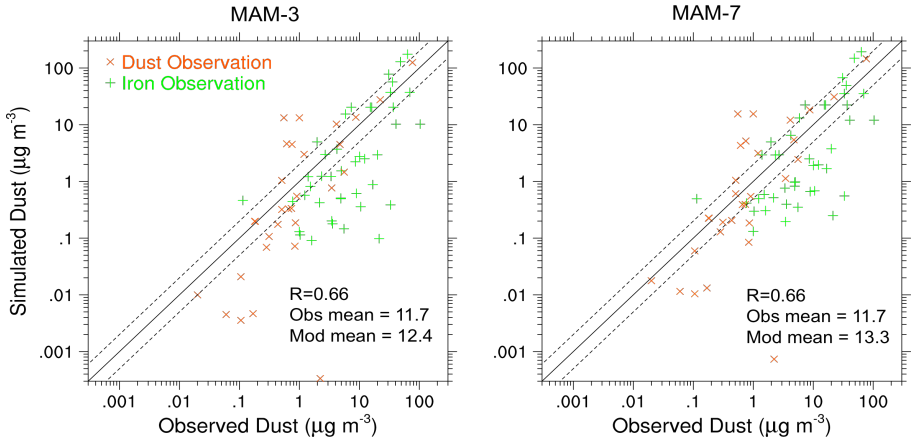

Fig. 18. Observed and simulated annual-average mineral dust concentrations ($\mu g\,m^{-3}$). Observations are from Table S2 of Mahowald et al. (2009). Only station measurements are shown (no cruise measurements), and dust concentrations were calculated from the iron concentrations assuming 3.5 % iron in dust, as in Mahowald et al. (2009). The symbols distinguish the original data types: actual dust measurement (×), or dust concentrations converted from iron measurement (+).

GMDD
4, 3485–3598, 2011

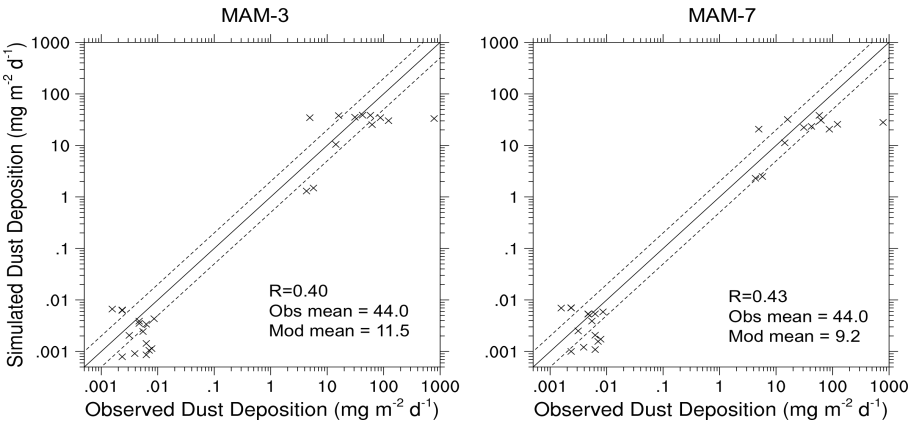

Fig. 19. Observed and simulated annual-average mineral dust total (dry plus wet) deposition fluxes (mg m^{-2} d^{-1}). Observations are from Table S1 of Mahowald et al. (2009). Dust deposition fluxes were calculated from the iron deposition fluxes assuming 3.5 % iron in dust.

GMDD
4, 3485–3598, 2011

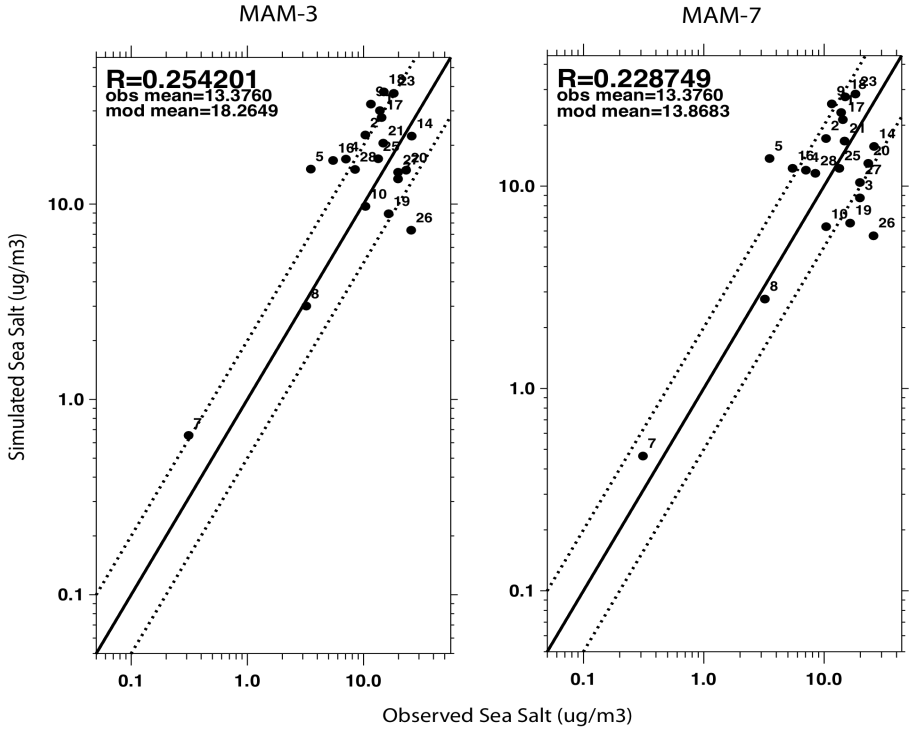

Fig. 20. Same as Fig. 10, but for sea salt concentrations ($\mu g\, m^{-3}$). The global locations of sites denoted by different numbers in the figure can be found in Wang et al. (2011).

GMDD
4, 3485–3598, 2011

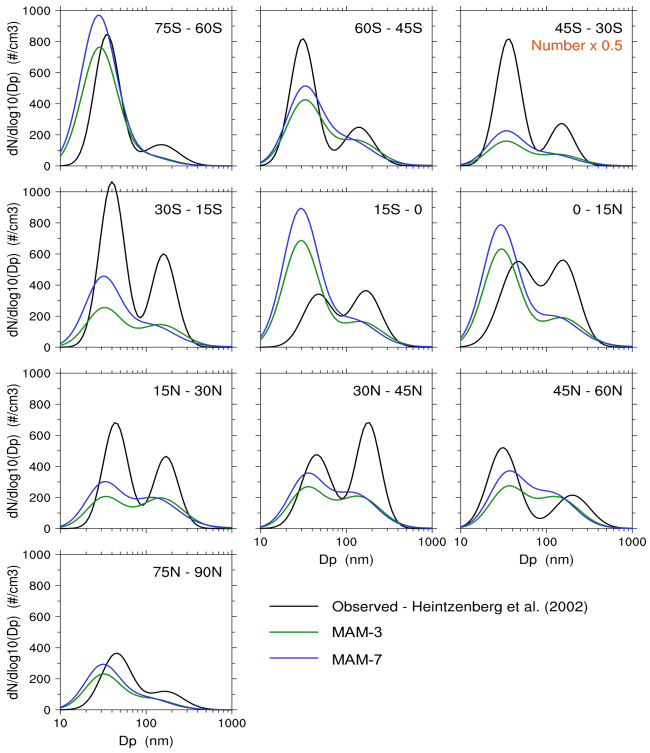

Fig. 21. Submicron aerosol number size distributions in the marine boundary layer. Observations (Obs.) from Heintzenberg et al. (2000) were compiled and aggregated onto a 15° × 15° grid then averaged zonally. The model data are spatially averaged over the 15° × 15° grid cells having observations. Model data for MAM3 and MAM7 are temporally averaged over December–February for 75–45° S, over November–March for 45–30° S, annually for 30° S–30° N, over May–September for 30–45° N, over June–August for 45–90° N. For the 45–30° S latitude band, aerosol number densities are scaled by 0.5 so the same vertical axis can be used for all latitudal bands.

GMDD
4, 3485–3598, 2011

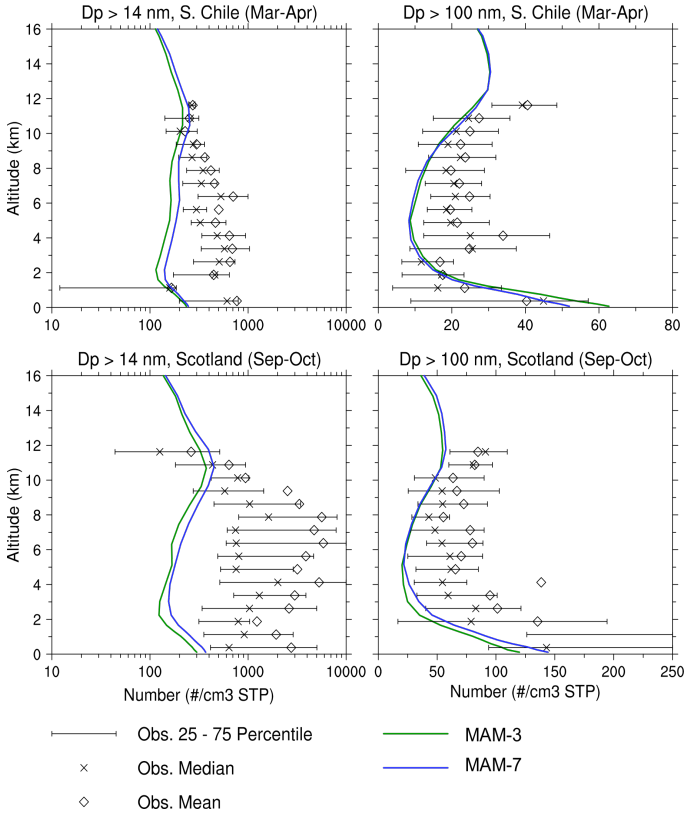

Fig. 22. Vertical profiles of aerosol number concentration of Aitken mode particles with diameter > 14 nm (left) and accumulation mode particles with diameter > 100 nm (right), near Punta Arenas, Chile during March/April (top) and near Prestwick, Scotland in September/October (bottom). Observations are from Minikin et al. (2003): median (star), 25 and 75 percentiles (left and right end of error bars). Model results for MAM3 and MAM7 are averaged over latitude-longitude ranges of 60–50° S, 70–85° W for Chile, and over 50–60° N, 10° W–5° E for Scotland.

GMDD
4, 3485–3598, 2011

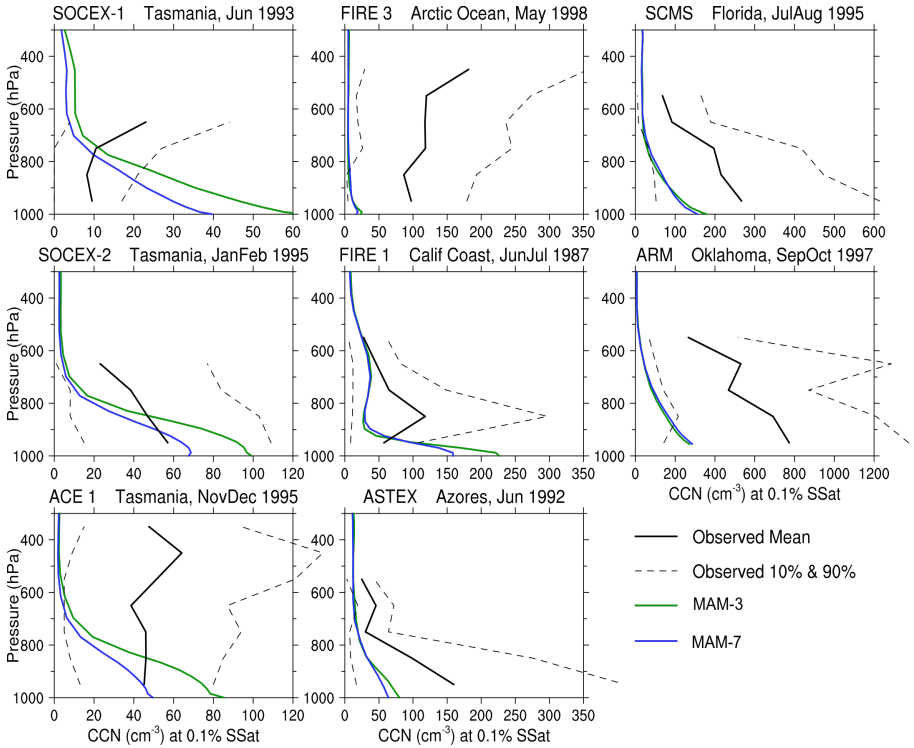

Fig. 23. Observed and simulated vertical profiles of CCN concentrations at 0.1 % supersaturation for eight field experiments. Field experiment acronym, location, and date are shown above each plot, and more details are given in Table 1 of Ghan et al. (2001). Observed values are means (solid black lines) and 10th and 90th percentiles (dashed black lines) for each experiment. Simulated values (colored lines) for MAM3 and MAM7 are averages over the months shown and experiment location.

GMDD
4, 3485–3598, 2011

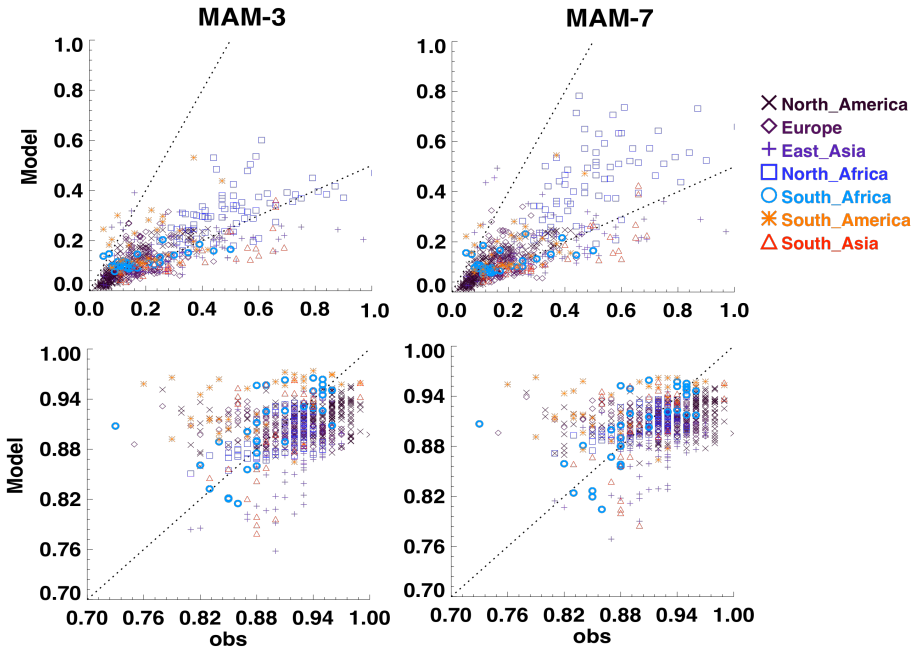

Fig. 24. Comparison of modeled monthly aerosol optical depth (AOD) (upper) and single scattering albedo (SSA) (lower) at 550 nm from MAM3 (left) and MAM7 (right) with observations from the AERONET (http://aeronet.gsfc.nasa.gov) at 75 sites in seven regions (North and South America, Europe, East and South Asia, and Northern and Southern Africa) over the globe. Dashed lines are 1 : 2 or 2 : 1 for AOD (upper) and 1 : 1 for SSA (lower).

GMDD
4, 3485–3598, 2011

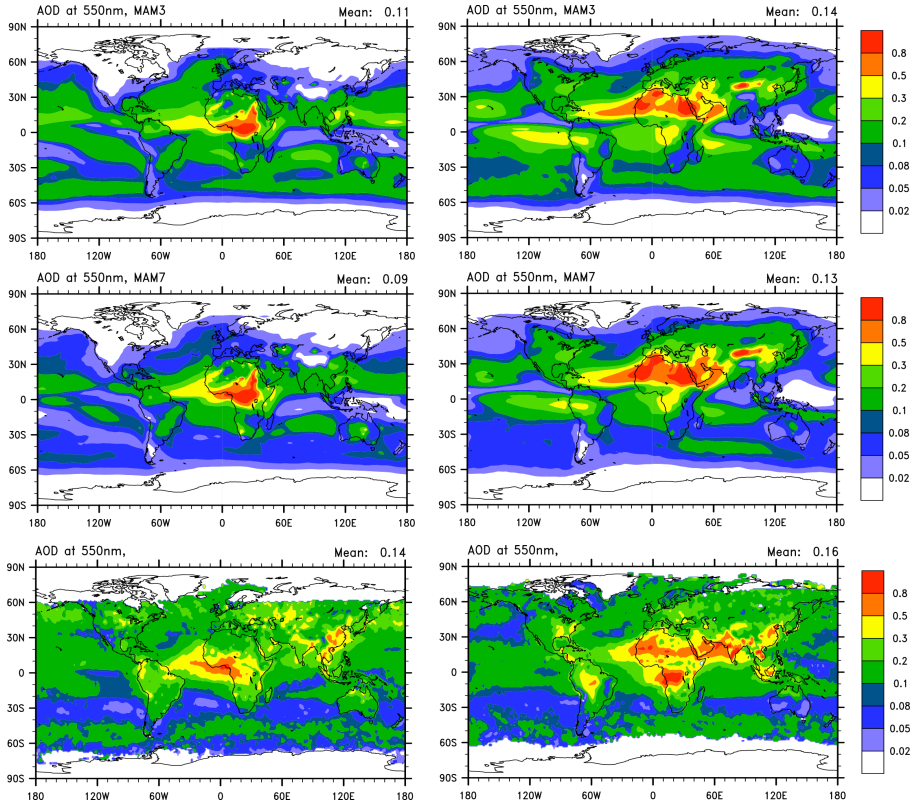

Fig. 25. Comparison of simulated AOD at 550 nm from MAM3 (upper) and MAM7 (middle) in January (left) and July (right) with that from a satellite AOD retrieval composite (lower) derived by Kinne et al. (2006).

GMDD
4, 3485–3598, 2011

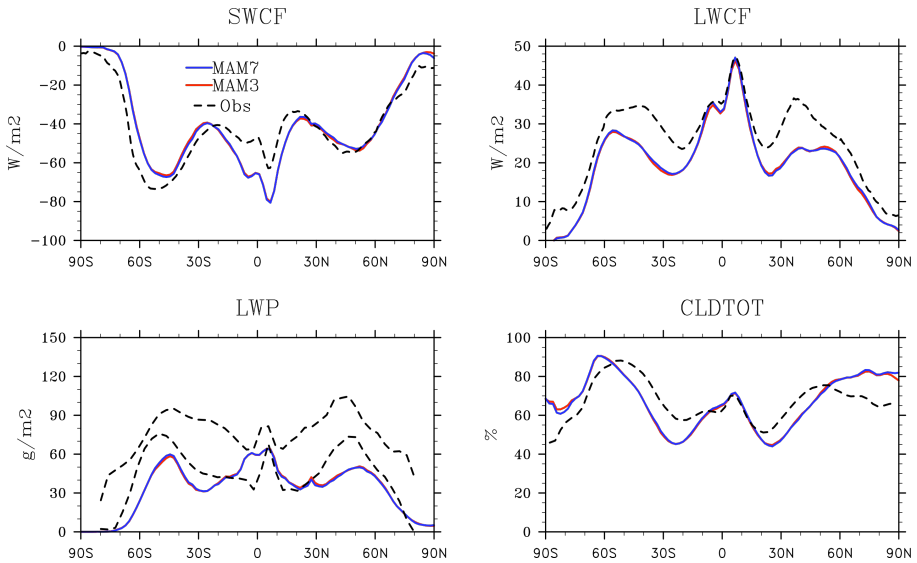

Fig. 26. Annual and zonal mean shortwave cloud forcing (SWCF), longwave cloud forcing (LWCF), liquid water path (LWP), and total cloud cover (CLDTOT) from MAM3 and MAM7 in comparison with observations. Observed SWCF and LWCF are from CERES; observed LWP is from SSM/I with two data sources: Weng and Grody (1994) (lower dashed line) and Greenwald et al. (1993) (upper dashed line); and observed CLDTOT is from ISCCP. LWP comparison is restricted to oceans.

GMDD
4, 3485–3598, 2011

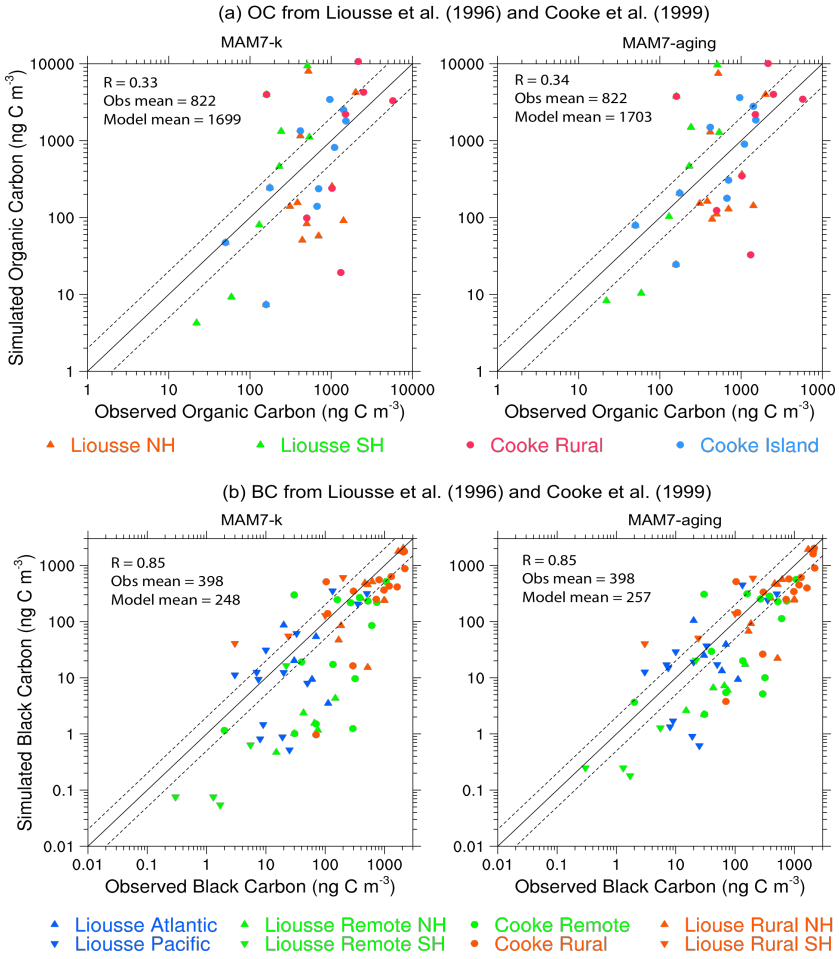

Fig. 27. Same as Fig. 13 but with model results from MAM7-k and MAM7-aging sensitivity simulations.

GMDD
4, 3485–3598, 2011

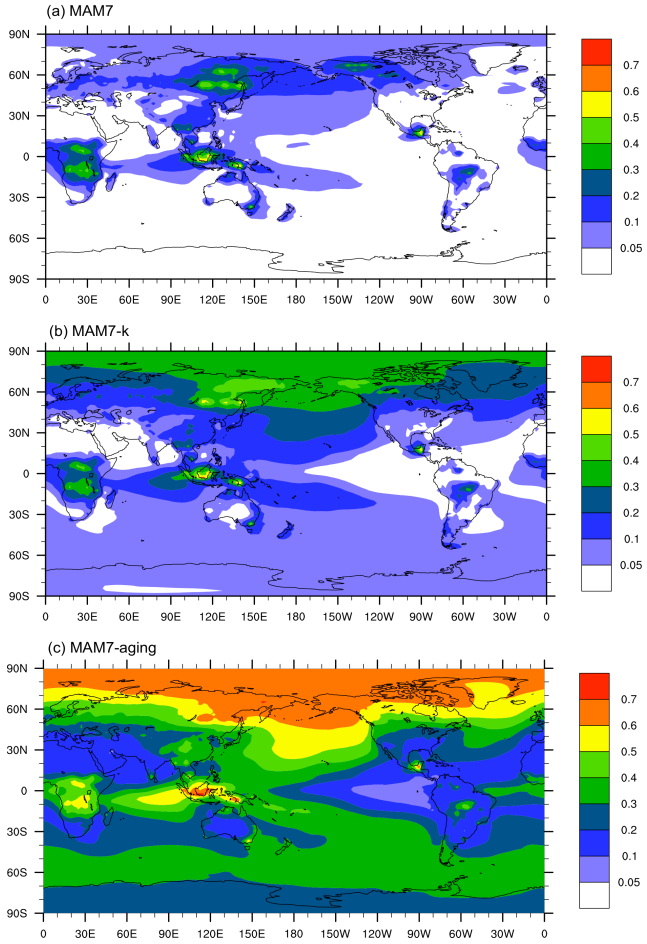

Fig. 28. Mass fraction of the total BC column burden that is in the primary carbon mode from the three experiments: MAM7, MAM7-k and MAM7-aging.

GMDD
4, 3485–3598, 2011